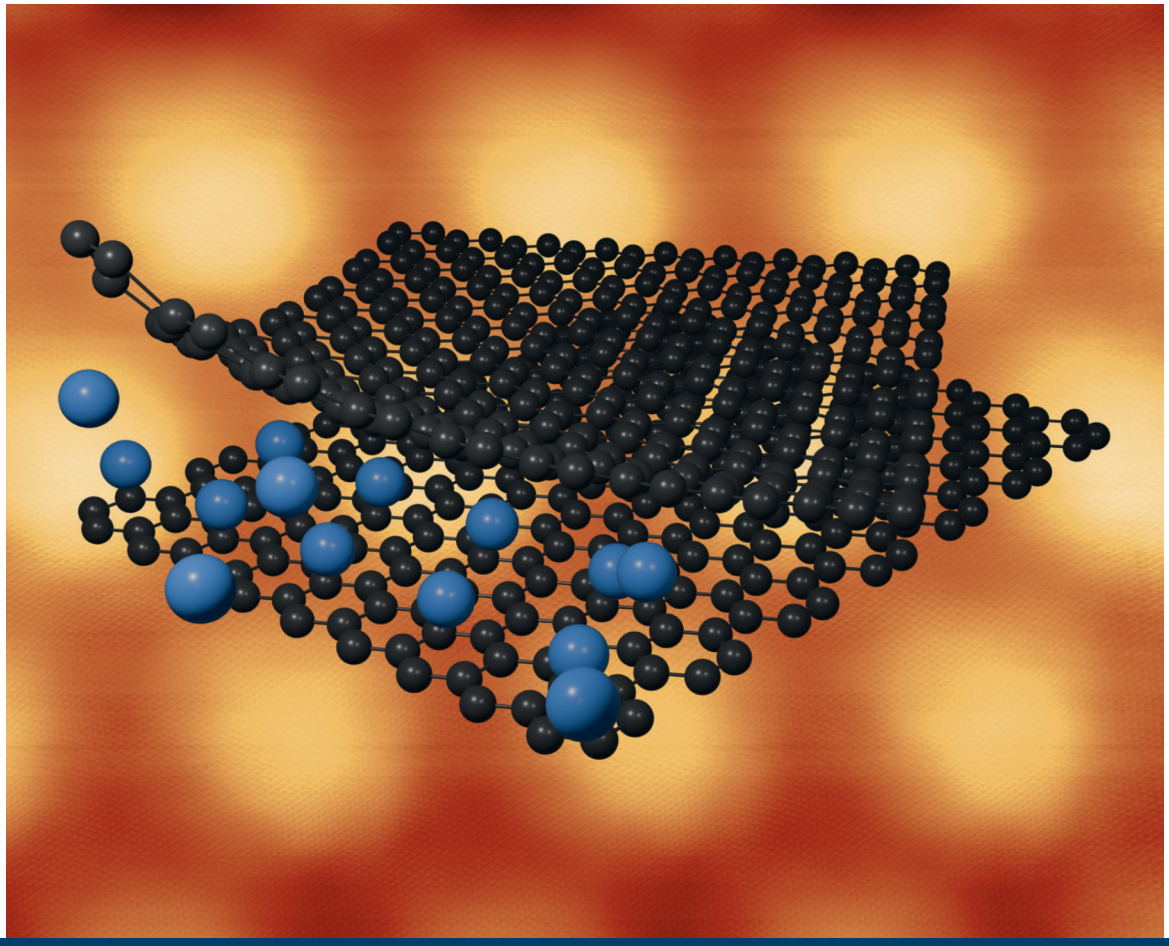

Towards high-quality decoupled Graphene heterostructures

Mark Hutter

Information
Band / Volume 127
ISBN 978-3-95806-913-8

Mitglied der Helmholtz-Gemeinschaft

JÜLICH
Forschungszentrum

Schriften des Forschungszentrums Jülich
Reihe Information / Information Band / Volume 127

Forschungszentrum Jülich GmbH
Peter Grünberg Institut (PGI)
Quantum Nanoscience (PGI-3)

Towards high-quality decoupled Graphene heterostructures

Mark Hutter

Schriften des Forschungszentrums Jülich
Reihe Information / Information Band / Volume 127

ISSN 1866-1777 ISBN 978-3-95806-913-8

Bibliografische Information der Deutschen Nationalbibliothek.
Die Deutsche Nationalbibliothek verzeichnet diese Publikation in der
Deutschen Nationalbibliografie; detaillierte Bibliografische Daten
sind im Internet über http://dnb.d-nb.de abrufbar.

Herausgeber und Vertrieb:	Forschungszentrum Jülich GmbH Zentralbibliothek, Verlag 52425 Jülich Tel.: +49 2461 61-5368 Fax: +49 2461 61-6103 zb-publikation@fz-juelich.de www.fz-juelich.de/zb
Umschlaggestaltung:	Grafische Medien, Forschungszentrum Jülich GmbH
Druck:	Grafische Medien, Forschungszentrum Jülich GmbH
Copyright:	Forschungszentrum Jülich 2026

Schriften des Forschungszentrums Jülich
Reihe Information / Information, Band / Volume 127

D 82 (Diss. RWTH Aachen University, 2026)

ISSN 1866-1777
ISBN 978-3-95806-912-1 (Print)
ISBN 978-3-95806-913-8 (E-Book)

Vollständig frei verfügbar über das Publikationsportal des Forschungszentrums Jülich (JuSER)
unter www.fz-juelich.de/zb/openaccess.

Contents

Abstract

This thesis deals with the 2D material graphene, which has been the subject of intense research in recent years due to its unique properties. The main focus is on different ways to tune the properties of graphene. Several approaches to modify the properties of graphene are investigated, focusing on intercalation and twisted bilayer structures.

The intercalation with Bi and Se is studied using the Normal Incidence X-ray Standing Wave (NIXSW) technique, which reveals the vertical structure of these systems, from which some electronic properties can be deduced. For the intercalation with Bi, the two phases (α and β) are discussed. For all samples, the results show a successful decoupling of the graphene from the substrate (SiC(0001)), with van-der-Waals bond distances of Bi and Se to graphene and covalent bond distances to the substrate.

Epitaxially grown samples are also discussed for twisted bilayer graphene. Two 30° twisted bilayer graphene samples are grown using the surfactant-mediated growth technique presented by Bocquet [1] and are investigated with respect to the different annealing temperatures during the growth. A temperature difference of only 50 K results in a very different structure and thickness of the graphene layers.

Besides the epitaxial growth, twisted bilayer graphene is also prepared by exfoliation and stacking for scanning tunneling microscopy (STM) and transmission electron microscopy (TEM) investigations. A sample with a twist angle of 1.2° reveals in STM the shift of van Hove singularities and the possibility of doping the sample through the STM tip. For TEM, different transfer methods are investigated, including the use of different polymer stamps and different TEM grids (Cu grid, sapphire glass, and SiN wafer). Despite progress in the sample preparation, further studies are needed to find a suitable

transfer method and to realize the TEM investigations of twisted bilayer graphene.

Zusammenfassung

Diese Arbeit befasst sich mit dem 2D-Material Graphen, das in den letzten Jahren aufgrund seiner einzigartigen Eigenschaften intensiv erforscht wurde. Der Schwerpunkt liegt auf einigen verschiedenen Möglichkeiten, die Eigenschaften von Graphen zu optimieren. Es werden mehrere Ansätze zur Modifizierung der Eigenschaften von Graphen untersucht, wobei der Schwerpunkt auf Interkalation und Twisted-Bilayer-Graphen liegt.

Die Interkalation mit Bi und Se wird mithilfe der NIXSW-Technik (Normal Incidence X-ray Standing Wave) untersucht, womit die vertikale Struktur dieser Systeme bestimmt werden kann. Aus dieser vertikalen Struktur lassen sich Rückschlüsse auf einige elektronische Eigenschaften ableiten. Zwei Proben, die mit Bi interkaliert wurden, werden aufgrund ihrer unterschiedlichen Phasen (α und β) diskutiert. Die Ergebnisse zeigen für alle Proben eine erfolgreiche Entkopplung des Graphens vom Substrat (SiC(0001)), wobei van-der-Waals-Bindungsabstände von Bi und Se zu Graphen und kovalente Bindungsabstände zum Substrat bestimmt wurden.

Epitaktisch gewachsene Proben werden auch für Twisted-Bilayer-Graphen diskutiert. Zwei 30° Twisted-Bilayer-Graphen Proben wurden unter Verwendung der von Bocquet [1] vorgestellten ”surfactant”-vermittelten Wachstumstechnik gezüchtet und im Hinblick auf die unterschiedlichen Glühtemperaturen während des Wachstums untersucht. Ein Temperaturunterschied von nur 50 K führt zu sehr unterschiedlichen Strukturen und Dicken der Graphenschichten.

Neben dem epitaktischen Wachstum wird Twisted-Bilayer-Graphen auch durch Exfolieren und Stapeln hergestellt, um Untersuchungen mittels Rastertunnelmikroskopie (STM) und Transmissionselektronenmikroskopie (TEM) durchzuführen. Eine Probe mit

einem Twist-Winkel von 1,2° zeigte im STM die Verschiebung der van-Hove-Singularitäten. Außerdem war es möglich, die Probe durch die STM-Spitze zu dotieren. Für TEM wurden verschiedene Transfermethoden getestet, darunter die Verwendung verschiedener Polymerstempel und verschiedener TEM-Gitter (Cu-Gitter, Saphirglas und SiN-Wafer). Trotz der Fortschritte bei der Probenvorbereitung sind weitere Studien erforderlich, um eine geeignete Transfermethode zu finden und Twisted-Bilayer-Graphen im TEM zu untersuchen.

List of Acronyms

1D	One-dimensional
2D	Two-dimensional
AFM	Atomic force microscopy
ARPES	Angle-resolved photoemission spectroscopy
DBBA	10, 10'-dibromo-9,9'bianthracene
DLS	Diamond Light Source
EDM	Energy distribution map
FFT	Fast Fourier transform
FWHM	Full width at half maximum
hBN	Hexagonal boron nitride
IPA	Isopropyl alcohol
LEED	Low-energy electron diffraction
LEEM	Low-energy electron microscopy
NI	Normal incidence
NIXSW	Normal-incidence X ray standing wave
PASG	Polymer-assisted sample growth
PC	Polycarbonate
PDMS	Polydimethylsiloxane
PES	Photoelectron spectroscopy
PMMA	Poly(methyl methacrylate)

PVC	Polyvinylchloride
QFMLG	Quasifreestanding monolayer graphene
RT	Room temperature
STEM	Scanning transmission electron microscope
STM	Scanning tunneling microscopy
STS	Scanning tunneling spectroscopy
TBLG	twisted bilayer graphene
TEM	Transmission electron microscope
TMDC	Transition metal dichalcogenides
UHV	Ultrahigh vacuum
UPS	Ultraviolet photoemission spectroscopy
UV	Ultraviolet
vdW	van der Waals
XP	X ray photoelectron
XPS	X ray photoelectron spectroscopy
XSW	X ray standing wave
ZLG	Zero-layer graphene

1 Introduction

The relentless pursuit of faster, more efficient, and smaller electronic devices has consistently pushed the boundaries of materials science and engineering. For multiple decades, silicon-based semiconductors have constituted the foundation of the digital age, facilitating the exponential growth that was predicted by Moore's Law [2]. However, as the physical limits of silicon-based architectures are increasingly approached, including issues with heat dissipation and current leakage at smaller scales, the necessity to explore alternative materials and novel structural designs has become more urgent than ever [3]. It is imperative to comprehend the landscape of advanced material structures to facilitate the redefinition of the capabilities of future computer chips.

Among the various materials that have been the subject of significant research in recent years, graphene has been identified as a particularly promising candidate. Graphene, a single layer of carbon atoms arranged in a hexagonal lattice, possesses an extraordinary variety of properties, including exceptional electrical conductivity with high electron mobility, superior thermal dissipation, and remarkable mechanical strength [4, 5]. These characteristics render it an optimal subject for the investigation of next-generation electronic components. Initial challenges, particularly the absence of a natural band gap that would allow facile on/off switching, have historically prevented its widespread adoption in digital logic [6, 7]. However, recent breakthroughs in the field of engineering have reignited significant interest in this material. Specifically, the development of functional graphene semiconductors has led to a resurgence of interest in the potential applications of graphene in various technological domains. A body of research has emerged demonstrating methodologies for inducing a band gap in graphene. The methods employed include controlled growth on silicon carbide (epitaxial graphene), strain engineering, and chemical functionalization, which enable its operation as a semiconductor [7–9]. Furthermore, the electron mobility of graphene has been shown to be three orders of

magnitude larger than that of silicon, the prevailing material in microelectronics today [5, 10–12]. The distinctive electronic and thermal properties of graphene, in conjunction with its enhanced synthesis and integration, position it as a pivotal material on the verge of a transformative impact on the design of computer chips. This advancement has the potential to yield devices with unparalleled speed, energy efficiency, and miniaturization [3, 13]. The exploration of graphene's role is not merely an incremental improvement; rather, it represents a potential paradigm shift in the fundamental building blocks of computing.

In order to engineer graphene effectively for the demanding requirements of the micro- and nanoelectronics industries, it is indispensable to have a comprehensive understanding of its fundamental physical, electronic, and chemical properties. Graphene, a single atomic layer of the carbon allotrope graphite, consists exclusively of carbon atoms arranged in a hexagonal structure, forming what is known as a honeycomb lattice. It is noteworthy that each carbon atom within this lattice is sp^2-hybridized, which results in the formation of strong σ bonds in the plane with three neighboring carbon atoms, thereby establishing the material's robust two-dimensional framework. It is imperative to note that the remaining unhybridized π orbitals extend perpendicularly out of the plane, overlapping to form delocalized π and π^* bands. These bands approach the Fermi energy, at which point they exhibit a linear dispersion relation, a characteristic of massless Dirac fermions. At the $\vec{K}$ point, the characteristic Dirac point occurs at the point of intersection between the conduction and valence bands, while the energy dispersion forms the distinctive Dirac cones [5, 14].

In addition to its intriguing band structure and resulting properties, the scalable production of graphene is of paramount interest for producing material suitable for various advanced applications, such as high-frequency transistors, supercapacitors, solar cells and photocatalysts [6, 15]. The earliest method, mechanical exfoliation, yields high-quality, defect-free graphene flakes, typically up to 100 nm in edge length [4]. While not accessible to mass production, the merits of mechanical exfoliation and dry transfer lie in its capacity to carefully arrange diverse two-dimensional materials at predetermined twist angles. This facilitates the fabrication of van-der-Waals heterostructures with programmable electronic properties, a requirement for fundamental research into emergent

quantum phenomena, including, but not limited to, superconductivity and correlated insulating states, particularly in the context of ”twistronics” applications [14, 16–23].

Another significant approach to synthesizing graphene is epitaxial growth. One such method involves the annealing of various carbon species, including amorphous carbon and ethylene, on metal surfaces [24–28]. A more popular and technologically relevant method is the thermal decomposition of silicon carbide (SiC). In this process, a graphene-like layer is formed on the SiC surface through the desorption of Si atoms. Further annealing can produce multiple layers of graphene on the SiC(0001) substrate. This method holds particular promise for the large-scale, high-quality production of graphene layers directly on semiconducting or semi-insulating substrates [29–34]. This approach enables seamless integration with existing silicon-based microelectronics [35, 36].

Other notable synthesis methods include chemical vapor deposition (CVD) and bottom-up synthesis of graphene nanoribbons (GNRs). CVD is regarded as a highly scalable method for producing large-area graphene films on metal catalysts (e.g., copper or nickel) through the decomposition of carbon-containing gases [15, 37–42]. Bottom-up synthesis enables the precise, atomic-scale growth of GNRs with controlled widths and edge structures [43–45].

When contrasting the various preparation methods, a significant benefit of the epitaxial growth techniques lies in their ability to achieve a high level of cleanliness due to the use of ultra-high vacuum (UHV) conditions. However, a primary drawback associated with these methods is the constrained control over the twist angles or the stacking of different two-dimensional materials. Although twist angles and stacking of different materials can be easily achieved using exfolation techniques, there are two major drawbacks to exfoliation and stacking. On the one hand, the sizes of the resulting flakes and regions of interest are limited to the µm range, and on the other hand, the cleanliness of these stacks is not competitive with in-vacuum synthesis or growth due to residues left over from polymer transfers. Notably, cleanliness has greatly improved by new transfer methods [46, 47]. In this work, only mechanical exfoliation and stacking, as well as epitaxial growth on SiC have been applied to the research of graphene.

In addition to the synthesis of graphene samples, the manipulation of graphene properties is also essential. The investigation has so far focused on three distinct research areas. First, epitaxially grown graphene on SiC can be intercalated with various elements to decouple the graphene from the underlying substrate. Successful intercalations have been performed with antimony [48, 49], bismuth [50], copper [51], germanium [52], gold [53, 54], hydrogen [31, 55], indium [56], lead [57–59], oxygen [60, 61], and tin [62]. These intercalants often change the doping level, but also influence other properties. For example, the charge-carrier type can be tuned by the amount of germanium or gold [52, 53]. Induction of superconductivity in graphene by intercalation with lithium has also been observed in the past [63].

Second, interesting physics can also be observed when two monolayers of graphene are twisted against each other. Very small twist angles, especially the so-called magic angle ($\approx 1.05°$), have been studied extensively both experimentally and theoretically. [18, 19, 21, 22, 64–71] Here, the appearance of van-Hove singularities was observed. In twisted bilayer graphene (TBLG), a van-Hove singularity emerges when the misaligned Dirac cones from each graphene layer ”cross” or hybridize, thereby creating saddle points in the electronic band structure where the density of states experiences a pronounced increase. The energy of these singularities can be adjusted by modifying the twist angle between the layers [69, 72–74]. In addition, superconductivity was observed for magic-angle TBLG [16, 21]. However, not only small angles are of interest, but also large twist angles in the range of 20° to 30° have attracted attention. In particular, theoretical studies have predicted interesting phenomena in large twist angle samples. On the one hand, corner states with fractional electron charges are predicted by Park et al. [75], while Pal et al. [76] propose the existence of an alternating structure of gapped and non-gapped regions within the moiré pattern. For a twist angle of 30°, an experimental route to produce TBLG in an epitaxial manner has recently been demonstrated. Here, the 30° angle can be achieved by thermal decomposition of SiC in a partial pressure of borazine, which rotates the top layer with respect to the subsequently grown graphene layers below [1].

The following thesis will present five different methods for investigating the altered

properties of graphene. Initially, epitaxial graphene on SiC(0001) is intercalated with bismuth. As demonstrated in previous research conducted by Sohn et al. [50], the existence of two different phases, designated as α and β, has been established. It has thus been determined that these two phases are distinguishable based on their respective properties. In particular, the presence of a metallic band structure has been identified in the α-phase, while the β-phase demonstrates an insulating band structure. The structures of both phases, particularly in the vertical direction, remain uncertain. The aim of this work is to determine the structure and characterize the bonding from Bi to both graphene and SiC. This objective is accomplished by conducting a series of X-ray standing wave (XSW) experiments on the two phases of Bi-intercalated graphene on SiC(0001).

Secondly, building upon our established methodology, previously applied to the bismuth-graphene system, the next project now shifts focus to the intercalation of graphene with selenium (Se). The primary objective is to precisely determine the vertical structure of the selenium within the graphene lattice, thereby yielding critical information regarding the bonding configuration of the intercalant. In accordance with previous studies, the XSW technique will be used once more for the highly precise determination of this vertical atomic arrangement. The objective of this research is to provide insights into the bonding character of Se-intercalated graphene.

In the third project, the epitaxial growth of graphene remained the primary focus. However, in contrast to intercalation, samples with TBLG were grown and investigated. The mechanism and synthesis procedure have previously been demonstrated in the literature [1, 77]. The precise role of the annealing temperature during graphene growth remains to be elucidated. It is yet to be determined whether the temperature can be adjusted to ensure the presence of a single twisted graphene layer on top of a single buffer layer, without the formation of additional partial layers. Consequently, the prepared samples were examined through the use of low energy electron diffraction (LEED), angle-resolved photoemission spectroscopy (ARPES) and low energy electron microscopy (LEEM).

In the fourth project, TBLG was prepared using the exfoliation and stacking method, an alternative to the epitaxial growth method. The objective of this study was to examine a graphene sample with a twist angle of 30°. As previously stated, the theoretical

framework predicts an alternating pattern of gapped and non-gapped regions [76]. The objective of this study was to utilize scanning tunneling microscopy (STM) and scanning tunneling spectroscopy (STS) to investigate these differing regions.

The last project is complementary to the previous one. Instead of preparing TBLG samples for the investigation in STM, different ways of transferring TBLG onto a substrate suitable for transmission electron microscopy (TEM) were explored. The goal was to be able to measure the predicted corner states with fractional electron charges [75]. Unfortunately, the work within this thesis was limited to the preparation.

2 Methods

2.1 Normal-Incidence x-Ray Standing Wave

In 1964, Boris W. Batterman was the first to demonstrate the application of an X-ray standing wave (XSW) field in the study of the properties of single-crystal surfaces. He built on previous research to develop a method that utilized XSW, which was first used in 1969. The purpose of this method was to ascertain the precise locations of foreign species. Initially, this novel technique was utilized sparingly by scientists specializing in the study of surfaces. However, its utilization increased significantly following the development of synchrotron radiation sources. These sources provided the brightness and capacity for modification in the method required for more sophisticated XSW experiments [78, 79].

At present, XSW is a useful technique for making exact measurements of structures. These include, but are not limited to, determining the height and location of adsorbates on a surface and providing precise vertical coordinates of adsorbates relative to the substrate lattice planes [80]. One such type of XSW, known as normal incidence X-ray standing wave (NIXSW), is frequently employed. The X-ray beam is oriented perpendicularly to the crystal surface and exhibits a variable photon energy [78, 81, 82]. However, the experimental setup for XSW can be adapted to accommodate a variety of shapes, depending on the particular application and the characteristics of the sample under investigation. These alternatives include Total External Reflection XSW (TER-XSW), in which the standing wave is formed at a low angle for the study of structures with low density above reflecting interfaces [83]. Grazing Incidence X-ray Standing Wave (GIXSW) is another such technique that utilizes the concept of grazing incidence. In this scenario, the standing wave is formed by the interference of beams that are incident, specularly reflected, and specularly diffracted. This property renders it

advantageous for applications such as depth profiling and characterizing nanoparticles on surfaces [83].

The chemical shift observed in X-ray photoelectron spectroscopy (XPS), a technique frequently employed in conjunction with XSW, facilitates the differentiation between atoms of disparate elements. Furthermore, it has the capacity to discern variations in the positional arrangement of atoms within a singular element. Fluorescence spectroscopy can be utilized as an alternative to photoemission to differentiate between disparate elements. In this study, NIXSW was employed in conjunction with photoelectron spectroscopy to investigate the adsorption heights of intercalants in graphene.

A more thorough examination of the NIXSW process reveals the necessity of an X-ray standing wave as a prerequisite. Consequently, the monochromatic X-ray beam impacts the surface at normal incidence, and for specific energies, an X-ray standing wave field is generated due to the interference of the incident and reflected beams. This is the case if the energy of the X-ray beam satisfies the Bragg condition. The corresponding energies are also referred to as Bragg energies (E_B)

$$n\lambda = 2d\,\sin(\theta) \tag{2.1}$$

$$\lambda = \frac{hc}{E_\mathrm{B}} \tag{2.2}$$

$$E_\mathrm{B} = \frac{nhc}{2d\,\sin(\theta)}. \tag{2.3}$$

Here, n is an integer value, d is the distance between two lattice planes, h is the PLANCK constant, c is the speed of light, θ is the angle of the incident beam and λ is its wavelength. Thus, precise control and tunability of the X-ray beam energy is essential to fulfill the Bragg condition for diverse materials. Therefore, synchrotron radiation sources are the optimal choice for experiments involving NIXSW [82].

The generated X-ray standing wave field has an intensity of [84]

$$I = \left| E_0 e^{-2\pi i \vec{k_0} \vec{r}} + E_H e^{-2\pi i \vec{k_H} \vec{r}} \right|^2 = |E_0|^2 \left| 1 + \frac{E_H}{E_0} e^{-2\pi i \vec{H} \vec{r}} \right|^2, \tag{2.4}$$

where E_0 and E_H are the complex amplitudes of the incident and reflected beams, respectively. $\vec{k_0}$ and $\vec{k_H}$ are the corresponding wave vectors, while $\vec{H}$ is the reciprocal lattice vector of the used Bragg reflection $(hkil)$. $\vec{r}$ is the real space vector, and $|E_0|^2$ is the intensity of the incident beam. The reflectivity R is defined as the ratio of the reflected and incoming beams

$$R = \frac{|E_H|^2}{|E_0|^2}. \tag{2.5}$$

Since the frequencies of the incoming and the reflected beam are same, the reflectivity R can be used to express the ratio of the intensities of the reflected and incoming beams

$$\frac{E_H}{E_0} = \sqrt{R} e^{i\phi}, \tag{2.6}$$

where ϕ is the phase between the incoming and reflected beams. The combination of the equations 2.4 and 2.6 results in [84]

$$I = \left| 1 + \sqrt{R} e^{i(\phi - 2\pi \vec{H} \vec{r})} \right|^2 = 1 + R + 2\sqrt{R} \cos\left(\phi - 2\pi \vec{H} \vec{r} \right). \tag{2.7}$$

The scalar product between the vector $\vec{H}$ and the position vector $\vec{r}$ defines the spatial variation of the XSW field. The XSW field intensity remains constant in the direction perpendicular to $\vec{H}$, while parallel to $\vec{H}$, the XSW field shows a periodic modulation with a spacing of d_{hkil}, which is the distance between successive Bragg planes with the Miller indices (hkil). This leads to the equation $\vec{H}\vec{r} = z$, where z is the coordinate perpendicular to the Bragg plane. The attribution of these coordinates to actual atomic positions is possible through the use of a detection method known as photoelectron spectroscopy (PES). Typically, core-level electrons are known to undergo excitation

and subsequent release from the atom when exposed to an external photon source, such as UV light or X-rays. In this instance, the excitation is facilitated by the X-ray standing wave field. The energy of the released photoelectron is dependent on the core-level as well as the surrounding of the specific atom [85, 86].

When taking this photoemission process into account, z reflects the atomic position. However, this atomic position varies due to thermal vibrations and surface disorder. Therefore, a distribution, $f(z)$, of positions is used, where the integration of $f(z)$ over dz equals 1. For simplification and easier fitting, two parameters are introduced: the coherent position, $P_c^{\mathbf{H}}$, and the coherent fraction, $F_c^{\mathbf{H}}$ [78]. This results in

$$I = 1 + R + 2F_c^{\mathbf{H}}\sqrt{R}\cos\left(\phi - 2\pi P_c^{\mathbf{H}}\right). \tag{2.8}$$

The coherent position gives the vertical position via

$$z = d_{hkl}\left(n + P_c^{\mathbf{H}}\right), \tag{2.9}$$

where n is an integer. Given that the coherent position provides the position within the wave field, it can only be defined between 0 and 1, where 0 and 1 are directly on the Bragg plane. The same is true for the coherent fraction, which gives a value for the vertical order of the species. $F_c^{\mathbf{H}} = 0$ refers to a complete vertical disorder, while $F_c^{\mathbf{H}} = 1$ reflects a perfectly ordered species in the vertical direction. These two parameters can then be plotted in a polar coordinate system, where $P_c^{\mathbf{H}}$ is the angular position and $F_c^{\mathbf{H}}$ is the radial position. This plot is called an Argand diagram [82].

The coherent positions and coherent fractions resulting from equation 2.8 are only valid as long as the dipole approximation is legitimate. This dipole approximation is based on the assumption that the X-ray wave field is uniform across the atom. Consequently, the photoelectron yield is proportional to the square of the electric field at the atom's center, and thus proportional to I [87]. This approximation is valid under the condition that the wavelength of the standing wave field is considerably larger than the atom size.

However, for higher X-ray energies, corresponding to shorter wavelengths, this simplification becomes invalid, requiring the consideration of so-called non-dipolar effects [80]. Van Straaten et al. [88] introduced the correction factors S_R and S_I, as well as the phase ψ. This changes eq. 2.8 to [84, 88]

$$I = 1 + S_R R + 2\left|S_I\right| F_c^{\mathbf{H}} \sqrt{R} \cos\left(\phi - 2\pi P_c^{\mathbf{H}} + \psi\right). \tag{2.10}$$

One possibility to perform an XSW experiment is to ramp the photon energy through the Bragg energy. Alternatively, the angle of incidence relative to the crystal lattice plane can be varied. Here, the ramping through the photon energy is discussed. At each step, an X ray photoelectron (XP) spectrum and the reflectivity are measured. The different peaks in the XP spectrum are fitted with CasaXPS [89]. The peak intensity at each energy step is then plotted against the photon energy, resulting in a so-called yield curve. This yield curve can be fitted using eq. 2.10 using the dedicated Torricelli software [84, 90]. The resulting coherent position and coherent fraction are then plotted in the Argand diagram.

2.1.1 Experimental Setup

The NIXSW experiments shown in this work have been performed at the I09 beamline at the Diamond Light Source (DLS) in Didcot, UK. The complete setup is shown in side and top view in Fig. 2.1. Additionally, a photograph of the UHV system is depicted in Fig. 2.2. The end station itself consists of 5 different chambers, with two preparation chambers, two load locks and the main chamber. Both preparation chambers have sputtering and annealing capabilities, as well as potential evaporators for sample preparation. The second preparation chamber also provides a Low Energy Electron Diffraction (LEED) device for a quick verification of the preparation parameters. The two load locks are used to transfer samples into the UHV system. The most important part of the system is the main chamber. It is connected to the preparation chambers as well as to the branch from the synchrotron itself. Before the photons arrive in the main chamber, the beam energy can be selected using different monochromators. Both hard X-ray and

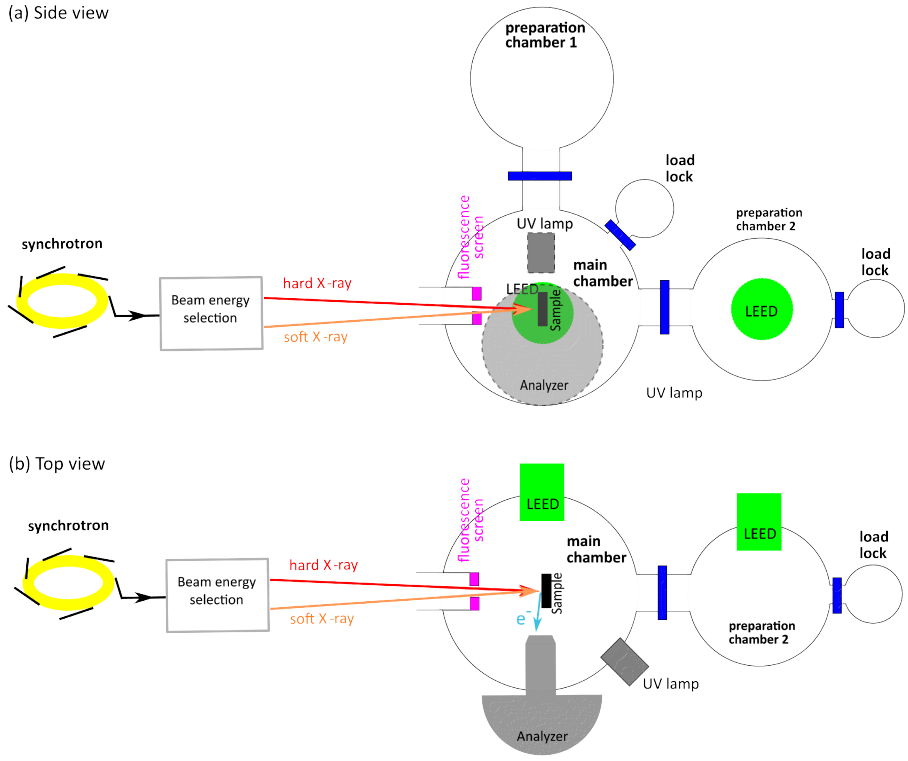

Fig. 2.1: Schematic drawings of the I09 beamline at the Diamond Light Source synchrotron. (a) Side view and (b) top view of the end station. In the top view, the load lock of the main chamber and the preparation chamber 1 are not shown for clarity, as they would be depicted on top [91].

soft X-ray photons are possible and both are focused onto the same position within the main chamber, where the sample is positioned on a five-way manipulator (not shown in Fig. 2.1). The resulting photoelectrons are detected by a hemispherical electron analyzer (VG Scienta EW4000 HAXPES), while the reflected photons are detected on a fluorescence screen. In addition to the synchrotron photon source, an ultraviolet (UV) lamp is installed for standard Ultraviolet Photoelectron Spectroscopy (UPS) measurements.

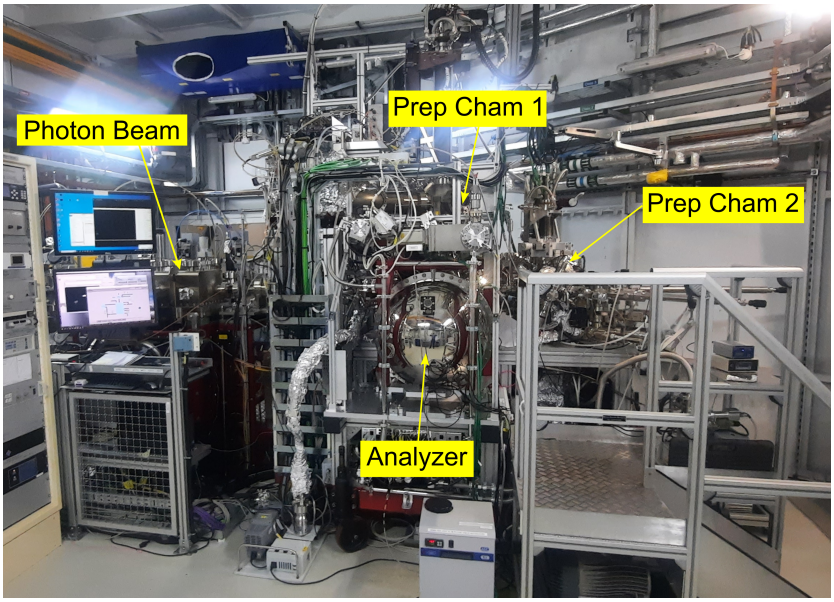

Fig. 2.2: Photo of the I09 beamline at the Diamond Light Source synchrotron. The view is from the opposite sitde as the side view shown in Fig. 2.1 (a).

The primary focus of the I09 beamline is the high-resolution study of the atomic and electronic structures of surfaces and interfaces. Notably, the NIXSW technique has been prioritized in the optimization process. Moreover, this beamline is currently the sole facility capable of performing XSW experiments under UHV conditions, a prerequisite for surface investigation to prevent contamination. Furthermore, the utilization of UHV is crucial in the examination of materials that are sensitive to either air or water. Consequently, this beamline is particularly well-suited for the investigation of the intercalated graphene samples discussed in Chapters 3 and 4, as some of these samples have demonstrated sensitivity to air.

2.2 Scanning Tunneling Microscopy

Scanning tunneling microscopy (STM) was invented by Gerd Binning and Heinrich Rohrer, who won the Nobel Prize in Physics in 1986 [92, 93]. STM makes use of the quantum tunneling effect, which describes the ability of a particle to tunnel through a potential barrier instead of overcoming it [94, 95]. This effect can be used to achieve a high lateral resolution (down to the atomic scale). To do this, a sharp metal tip (ideally down to single atoms) is brought close to the surface of interest, while a bias is applied. A schematic drawing of the STM setup is shown in Fig. 2.3. The tip is moved closer to the surface until a certain set tunneling current is observed. By scanning over the surface, the topography can be resolved, since the tunneling to the tip (or vice versa) always occurs from the atom on the surface that is closest to the last atom of the tip apex. However, one must be careful when referring to the topography as a simple height profile in STM. The tip is not sensitive to atomic position, but to electron density, so the resulting STM image is a mixture of the height profile and the electronic structure of the surface under investigation. Depending on the sign of the of bias on the sample, one sees either the filled electronic states (negative bias) or the empty electronic states (positive bias) [96].

This high lateral resolution requires not only an atomically sharp tip, but also the ability to move this sharp tip around in very small steps. Therefore, the piezoelectric effect is used and the tip is mounted on a set of piezos. These piezos allow to move the tip into each spatial direction (x, y, z) and are hence used to scan over the sample. In addition to the fine step piezos, coarse step piezos are also important for a coarse movement of the tip with respect to the sample. There is a coarse piezo in the z-direction to approach and retract the tip, for example to safely change the sample or refill a cryostat. In addition, some STMs have coarse step piezos in the scanning directions (x, y) to move around the sample, e.g., if not the whole surface is covered with the desired species or if parts of the surface are dirty or damaged. All these piezos are controlled by applying a voltage to them, which is then translated into a lateral shift of the tip position [96].

There are two different scan modes in the STM. The first is constant current, which attempts to keep the setpoint tunneling current constant at all times. This is achieved by

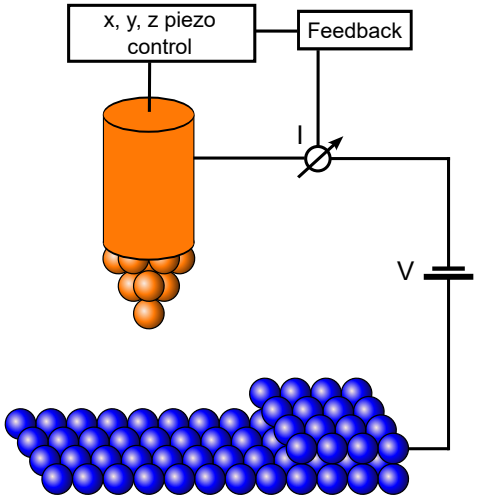

Fig. 2.3: A schematic drawing of the general setup of a scanning tunneling microscope [97].

moving the z-piezo slightly up and down. This feedback constantly adjusts the height of the tip to maintain the set tunneling current. The height of the piezo reflects the topography. This mode is relatively slow because the feedback needs some time to adjust the height of the tip. The faster method is constant height, where the tip position is kept constant and the tunneling current is recorded as the topography. The disadvantage of constant height is that a flat surface is required, otherwise the tip may crash into the sample [96].

2.2.1 Experimental Setup

The STM used is the Polar STM designed and manufactured by Scienta Omicron (formerly Sigma). A schematic drawing of the whole setup is shown in Fig. 2.4. This setup contains three connected UHV chambers, the LoadLock, the preparation chamber and the STM chamber. The LoadLock is equipped with a sample and tip garage for storing and transferring samples and tips in and out of the instrument. In addition, a quick access

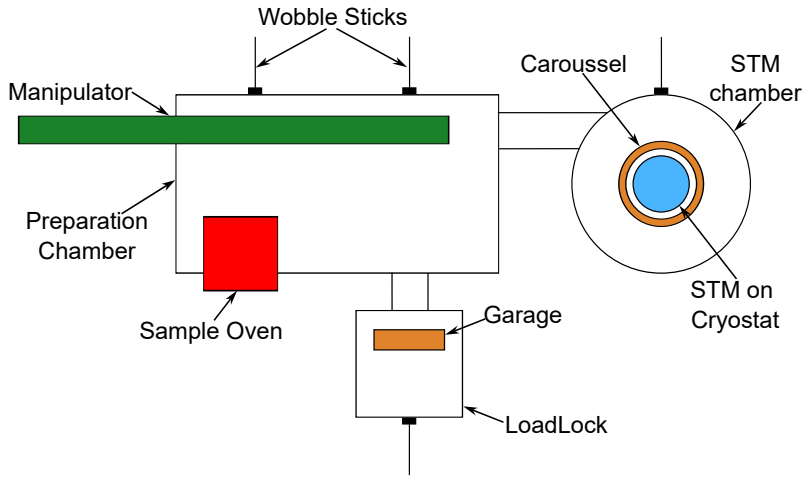

Fig. 2.4: A schematic drawing of the Polar STM.

door and a wobblestick are mounted to assist with transfers. The preparation chamber is connected to the Loadlock by a tube. The main object in the preparation chamber is the x,y,z manipulator, which has a multiple sample and tip slots, including heating stages, one for tips and one for samples. In addition, the preparation chamber provides various options for sample and tip preparation. There is also a sputter gun for cleaning single crystals and a sample oven for annealing to higher temperatures than are possible on the manipulator. There are also two wobble sticks for transferring and repositioning samples and tips. To move these into the STM chamber, the manipulator can be moved all the way into the STM chamber.

The STM is mounted on a 4K cryostat cooled by liquid helium and nitrogen. Sample and tip can be exchanged in the STM head using the mounted wobble sticks. Cryoshields surround the cryostat to reduce the heat load from the rest of the chamber and ensure stable, low temperature operation of the STM. A sample carousel is mounted around the cryoshields, providing space for 18 samples and four tips. Since STM measurements are sensitive to vibrations, the vacuum in the preparation and STM chambers is maintained by ion pumps, while the turbomolecular pumps are only used for a single pump-down

and then shut-down. In addition, the entire setup is mounted on pneumatic vibration isolators (vertical resonant frequency: $<$1.1 Hz, horizontal resonant frequency: $<$1.5 Hz), which provide a good damping of external vibrations caused, for example, by persons walking next to the setup or people talking in the laboratory.

3 Bismuth-intercalated quasifreestanding Graphene on SiC(0001)

The results presented in this chapter are partly published in the following journal article: S. Wolff, M. Hutter, P. Schädlich, H. Yin, M. Stettner, S. Wenzel, F. S. Tautz, F. C. Bocquet, T. Seyller, and C. Kumpf, ”Bi-intercalated epitaxial graphene on SiC(0001)”, New J. Phys. 26, 103009 (2024) [98].

The acquisition and analysis of the NIXSW data has been the author's contribution in this project. The paper was written by the author, S. Wolff, P. Schädlich and C. Kumpf. The sample preparation and the acquisition and analysis of the XPS, ARPES and LEED data was done by S. Wolff. The acquisition and analysis of the LEEM data was done by P. Schädlich with assistance from H. Yin.

3.1 Introduction and Motivation

As previously stated in the general introduction, a primary objective of intercalating epitaxially grown graphene on SiC(0001) is to break the strong coupling between the zeroth-layer graphene and the substrate [99], thereby potentially enabling its application in computer chips. Furthermore, the intercalation of diverse elements into graphene results in a spectrum of physical and chemical properties of the graphene layer, which may hold significance for future applications [31, 48–63, 100, 101]. In most cases, the intercalation of graphene leads to the electronic decoupling of the graphene layer from the substrate [101], which reveals the 2D characteristics of graphene, i.e. the Dirac cone

at the $\bar{K}$-point. Furthermore, the doping level of the graphene can be changed [101], the intercalant can introduce certain effects, such as superconductivity for Li intercalation [63], via the proximity effect.

To date, most intercalation processes have been performed with single atomic elements as intercalants. Promising candidates for intercalation are elemental Bi and Bi-based 2D materials, such as Bi_2Se_3 and Bi_2Te_3. Both Bi_2Se_3 and Bi_2Te_3 are topological insulators and heterostructures of them with graphene have been investigated in theory [102]. Here, a strong proximity spin-orbit coupling in graphene is predicted [102]. These heterostructure of Bi_2Se_3 and graphene even show a coexistence of superconductivity and topological order in thin films [103]. For elemental Bi also an effect of the strong spin-orbit coupling is observed when combined with $NbSe_2$ to a heterostructure [104].

The majority of studies on heterostructures with Bi, Bi_2Se_3 and Bi_2Te_3 and graphene are either theoretical works or still rely on thicker films or exfoliation and stacking. As previously stated in the introduction, these exfoliation techniques have significant drawbacks. Consequently, a systematic approach is imperative for the synthesis of a UHV-grown heterostructure of graphene with Bi, Bi_2Se_3 and Bi_2Te_3. A fruitful starting point for the investigation with epitaxially grown graphene is the intercalation with elemental Bi.

Therefore, this chapter will focus on the intercalation of epitaxial graphene on SiC(0001) with Bi. In their work, Y. Sohn et al. [50] presented the possibility of intercalating graphene on SiC(0001) with Bi. They found two different phases of the intercalated layer, which differ in the amount of intercalated Bi. The higher-coverage phase (called α phase) shows no specific LEED pattern other than that of the SiC substrate. Therefore, it is either a closely packed layer of Bi atoms with a (1x1) periodicity with respect to the SiC(0001) substrate, or a disordered layer. In Angle-Resolved Photoelectron Spectroscopy (ARPES), metallic bands are observed, in contrast to the lower coverage phase (β phase), which instead shows insulating and flat bands. This phase is $(\sqrt{3}\text{x}\sqrt{3})\text{R}30^\circ$ periodic to the substrate. [50]

In this chapter, the preparation of two samples, a α-phase and a β-phase sample, is

discussed. The two samples were characterized with XPS and ARPES [98, 105]. To gain further insight into the structure of both phases, NIXSW measurements were performed on them to obtain interlayer distances, which can be used to investigate the bonding character between the different layers.

3.2 Sample Preparation

The starting point of the preparation is a zeroth layer graphene (ZLG), also called buffer layer, on Si(0001) sample, which was prepared by polymer-assisted sublimation growth (PASG) as described by Kruskopf et al. [106]. Thereby the SiC(0001) wafer is spin-coated with a photoresist. During the spin coating process, a small amount of liquid material is placed on the center of a flat substrate. The substrate is then rotated at high speed, spreading the liquid by centrifugal force into a uniform film. The spin-coated photoresist is removed during annealing. This preparation method increases the homogeneity of the resulting ZLG sample. Next, the samples are transported through air from the induction furnace where the ZLG was prepared to the UHV system. Here, a thick layer of Bi is deposited on the ZLG using a conventional Knudsen-type evaporator until both the substrate and the overlying ZLG are no longer visible in the XP spectra. This corresponds to a thickness of at least 30 nm. The ZLG then is intercalated by the Bi on top by annealing at 350°C for 30 min, resulting in a Bi layer of the α-phase type below the former ZLG. To obtain the β phase, further annealing at 900°C for 30 min is required [50, 98].

3.3 XPS and ARPES

The ZLG sample, the α phase and the β phase of the Bi-intercalated graphene layer on SiC(0001) were characterized by XPS and ARPES to confirm the successful intercalation and to determine the degree of intercalation and the doping of the graphene layer. Starting with the ZLG sample, which is the basis for comparison, the C 1s XP spectrum is shown in Fig. 3.1 (a) in the upper spectrum.

There are two peaks, one large and one small one. The larger peak is labeled SiC and

derives from the bulk carbon. Fitting the peak with a Voigt peak shape, we find a peak energy of 283.66 eV. The second peak with a higher binding energy derives from the carbon atoms in the ZLG. One third of the atoms in the ZLG are still covalently bound to the top Si atoms of the substrate, while the other two thirds of the ZLG are only intralayer bound. Therefore, this peak must be fitted with two Voigt components reflecting these different binding situations. The peak labeled S1 refers to carbon atoms bound to the substrate and its fitted peak position is 284.76 eV, while the peak originating from the purely intralayer bound carbon atoms is located at 285.17 eV (labeled S2). In addition to the C 1s XP spectrum, XP spectra were also recorded for the Si 2p core level. For a Si 2p state, a Voigt doublet with an area ratio of 1:2 between the Si $2p_{1/2}$ and the Si $2p_{3/2}$ levels is expected, due to the spin-orbit splitting of 0.6 eV. This condition and the same full width at half maximum (FWHM) were used as constraints in the fit of the Si 2p XP spectra. Two species (two doublets) are required to fit the data. The result-

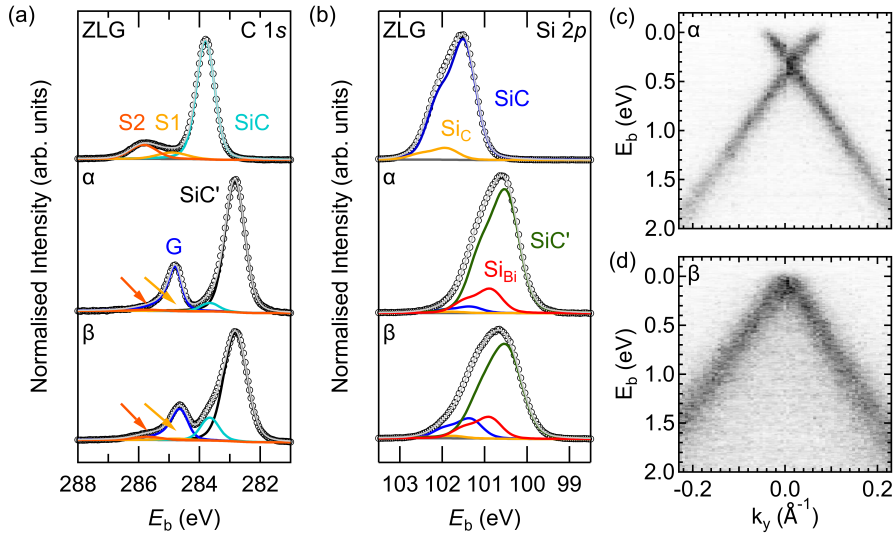

Fig. 3.1: (a, b) C 1s and Si 2p XP spectra of the ZLG, α, and β phases of Bi-intercalated graphene on SiC(0001). For the α and β phases, the components S1 and S2 are marked by yellow and red arrows, respectively. (c) ARPES data at the $\bar{K}$ point of the graphene for the α phase. (d) Same as (c) for the β phase. [98]

ing fit is shown in Fig. 3.1 (b) in the top panel. The most dominant species is labeled SiC (blue) and corresponds to the Si atoms in the bulk. The Si $2p_{3/2}$ peak is located at 101.48 eV. An additional small doublet is needed to account for the small chemical shift of the top Si layer, which is covalently bonded to the ZLG. The Si $2p_{3/2}$ peak of the surface Si atoms is shifted toward higher binding energies to 101.90 eV.

After the intercalation with Bi, the so-called α phase is formed. This leads to strong changes in the XP spectra, both C 1s and Si 2p, see Fig. 3.1 (a,b). There are five different peaks for the C 1s. The three peaks used to fit the data of the ZLG sample are also used here for the non-intercalated parts of the α-phase sample. In addition, there are two dominant new peaks, one for the decoupled graphene and another for the substrate atoms below the intercalated Bi atoms. The fitting parameters for all used components

Table 3.1: Fit parameters for C 1s and Si 2p core-level from both the α- and the β-phase samples.

	species	XP level	binding energy (eV)	peak shape	Asym.	Cut-off	error (χ^2)
α	S1	C 1s	284.76	Voigt	0	0	0.42
	S2	C 1s	285.85	Voigt	0	0	
	C_{SiC}	C 1s	283.66	Voigt	0	0	
	$C_{SiC'}$	C 1s	282.83	Voigt	0	0	
	C_G	C 1s	284.69	Mahan	0.042	1.4	
	SiC	Si 2p	101.34	Voigt doublet	0	0	0.17
	SiC'	Si 2p	100.48	Voigt doublet	0	0	
	Si_C	Si 2p	101.76	Voigt doublet	0	0	
	Si_{Bi}	Si 2p	100.86	Voigt doublet	0	0	
β	S1	C 1s	284.76	Voigt	0	0	0.39
	S2	C 1s	285.85	Voigt	0	0	
	C_{SiC}	C 1s	283.66	Voigt	0	0	
	$C_{SiC'}$	C 1s	282.82	Voigt	0	0	
	C_G	C 1s	284.53	Mahan	0.042	1.4	
	SiC	Si 2p	101.34	Voigt doublet	0	0	0.31
	SiC'	Si 2p	100.45	Voigt doublet	0	0	
	Si_{Bi}	Si 2p	100.88	Voigt doublet	0	0	

for both phases are shown in Table 3.1. The peak for graphene (G, blue) has an asymmetric shape and is located at 284.69 eV. If this chemical shift is compared to the literature value for highly oriented pyrolytic graphite (HOPG) (284.45 eV) [107], the found peak energy is close to the expected shift. The small difference of 0.24 eV between the peak energy of the fit and the literature value indicates n-type doping of the graphene. The peak for the intercalated substrate carbon atoms has a position in energy of 282.83 eV and is therefore shifted by -0.83 eV with respect to the non-intercalated substrate carbon atoms. These significant shifts for both the graphene and the substrate atoms with respect to the non-intercalated species indicate the successful intercalation of the ZLG with Bi. The degree of intercalation D based on the C 1s XP spectrum in the center panel of Fig. 3.1 (a) can be determined by the area ratio of the graphene peak (G) to the sum of G and the two ZLG peaks (S1, S2)

$$D = \frac{I(G)}{I(\mathrm{G}) + I(\mathrm{S1}) + I(\mathrm{S2})} , \tag{3.1}$$

which is D = 0.95 for the α phase. All determined D values for both phases are also shown in Table 3.2. A D value of 0.95 means that 95% of the former ZLG is intercalated with Bi and thus a good intercalation routine has been found. Besides using the ZLG and graphene intensities to calculate the degree of intercalation, also the bulk C intensities (SiC and SiC') can be used. Two distinct SiC species have been identified: the bulk carbon atoms of the intercalated regions (SiC') and those from the non-intercalated regions (SiC), remains of the ZLG. The degree of intercalation is determined by the area ratio between SiC' and the sum of SiC' and SiC

$$D = \frac{I(\mathrm{SiC'})}{I(\mathrm{SiC}) + I(\mathrm{SiC'})} . \tag{3.2}$$

with the peak intensities as shown in the middle spectrum of panel (a) of Fig. 3.1. Here, D = 0.94, showing a very good agreement with the previously determined D = 0.95 of the graphene and ZLG layer signals.

A third approach for determining the degree of intercalation involves the analysis of the

Table 3.2: Degree of intercalation resulting from the three different methods for both the α- and the β-phase samples. For the β-phase sample, only the value based on the C 1s spectrum was determined [105].

core-level	calculation basis	formula	$D(\alpha)$	$D(\beta)$
C 1s	graphene and ZLG	$\frac{I(G)}{I(\mathrm{G})+I(\mathrm{S1})+I(\mathrm{S2})}$	0.95	0.84
C 1s	(non-)intercalated bulk	$\frac{I(\mathrm{SiC'})}{I(\mathrm{SiC})+I(\mathrm{SiC'})}$	0.94	
Si 2p	(non-)intercalated bulk	$\frac{I(\mathrm{SiC'})+I(\mathrm{Si_{Bi}})}{I(\mathrm{SiC})+I(\mathrm{SiC'})+I(\mathrm{Si_{Bi}})}$	0.95	

Si 2p XP spectrum of the α phase. As with the C 1s, the ZLG peaks (SiC (blue) and $\mathrm{Si_C}$ (yellow)) have been included in the fit for the Si 2p, as shown in Fig. 3.1 (b). Additionally, there are two more features for the bulk Si atoms below the intercalated areas (SiC' (green)) as well as the top layer of Si atoms, which are bound to the intercalated Bi atoms ($\mathrm{Si_{Bi}}$ (red)). The bulk component after intercalation is labeled as SiC' and is located at 100.48 eV and shows a shift of 1.00 eV to lower binding energies compared to the bulk component of the ZLG sample (SiC). A comparable shift is evident in the Si atoms directly bound to the Bi ($\mathrm{Si_{Bi}}$), situated at 100.86 eV (shifted by 0.96 eV). The intensities of the SiC, SiC', and $\mathrm{Si_{Bi}}$ species in the Si 2p sepctra are related to the degree of intercalation by

$$D = \frac{I(\mathrm{SiC'}) + I(\mathrm{Si_{Bi}})}{I(\mathrm{SiC}) + I(\mathrm{SiC'}) + I(\mathrm{Si_{Bi}})} \,. \tag{3.3}$$

The degree of intercalation resulting from this method of determination is equal to that of the carbon-based analysis, $D = 0.95$. All values for the degree of intercalation calculated for both the α phase and the β phase are shown in Table 3.2.

To further prove the successful intercalation of the ZLG with Bi, ARPES investigations were performed on the α-phase sample. The $\bar{K}$ point is of particular interest because this is where the Dirac cone of graphene is expected. The ZLG shows no indication of a

Dirac cone, but after intercalation the ZLG is successfully decoupled from the SiC substrate and forms graphene. Hence, a Dirac cone with its characteristic linear dispersion is observed. This is shown in Fig. 3.1 (c). As it can be seen, the Dirac cone is not directly located at the Fermi level, but is shifted towards a lower binding energy by 360 meV. This indicates that the graphene is n-doped, in agreement with the previously observed shift of the XPS peaks of the intercalated species.

The α-phase sample can be transformed to a β-phase sample by annealing the sample up to 900°C. Subsequently, XPS and ARPES investigations were performed to verify the state of the sample and the degree of intercalation. The C 1s XP spectra are shown in the bottom panels of Fig. 3.1 (a) and (b). The peaks S1, S2, C_{SiC}, SiC, SiC' and Si_{Bi} are nearly identical to those of the α phase, compare Table 3.1. A significant difference is observed for the C_G peak. Its peak position is shifted by 160 meV towards lower binding energies, which indicates a less strong n-doping of graphene compared to the α phase. The degree of intercalation is determined similarly to the α phase. The result ($D = 0.84$) shows a small deintercalation upon annealing the sample to obtain the β phase.

In the ARPES measurement, the Dirac cone is again observed, including its typical linear dispersion at the $\bar{K}$ point, as shown in Fig. 3.1 (d). The Dirac cone for the β-phase is located at -10 meV, which shows a very small p-type doping. This shift of the Dirac point towards a higher binding energy is also consistent with the shift of the binding energy of the graphene in the XPS experiments.

The C 1s and Si 2p XP spectra provide meaningful information about the sucess of the intercalation, but no information about the intercalant layer is gained. Therefore, Bi 4f XP spectra were also recorded for the ZLG (before annealing, with Bi on top), for the α phase, and for the β phase. These XP spectra are shown in Fig. 3.2 (a).

In the upper part of panel (a) of Fig. 3.2, the Bi 4f XP spectrum of the ZLG layer with Bi on top shows the Bi $4f_{5/2}$ and Bi $4f_{7/2}$ Mahan doublet [108] with an area ratio of 3:4, which is included in the fitting routine. The binding energy of the Bi $4f_{7/2}$ is 156.84 ± 0.05 eV, which is similar for all three different samples. Besides the position, the peak shape and the total intensity give additional information. Regarding the peak

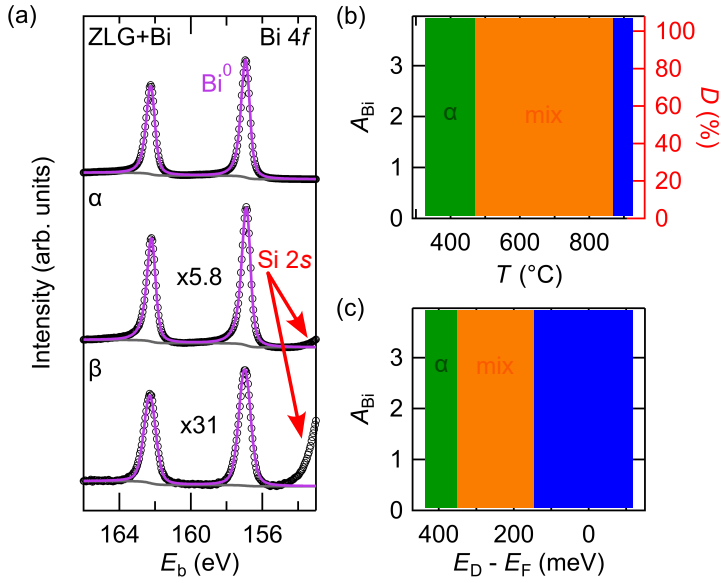

Fig. 3.2: (a) Bi 4f XP spectra of ZLG after Bi deposition but before intercalation (top) and of Bi-intercalated QFMLG after preparation of the α (middle) and β phase (bottom) at 350°C and 900°C, respectively. Red arrows mark the shoulder of the Si 2s peak located just outside the scan range. The spectra are shifted vertically for clarity and normalized to the Bi $4f_{7/2}$ peak. (b) The amount of Bi A_{Bi} in the sample (according to equation 3.4, black circles) and the degree of intercalation D (equation 3.1, red crosses), plotted against the annealing temperature of the sample. (c) Amount of Bi A_{Bi} on the sample as a function of the energy of the Dirac point E_D, which is a measure of the graphene doping level [98].

shapes, the ZLG with Bi on top as well as the α phase both show asymmetric peaks. Hence, they are fitted using a Mahan doublet [108] with an asymmetry parameter of 0.102, compare Table 3.3. This peak shape is representative of the metallic character of the Bi atoms [50]. When the sample is transferred to the β phase, the peak shape changes to a symmetric shape, indicating that the metallic character of the Bi intercalant layer is reduced and the layer becomes insulating, as it has been previously shown by Sohn et al. with ARPES investigations [50]. Therefore, a symmetric Voigt doublet is used instead

Table 3.3: Fit parameters for Bi 4f core-level from both the α- and the β-phase samples.

species	XP level	binding energy (eV)	peak shape	Asym.	Cut-off	error (χ^2)
α	Bi $4f_{7/2}$	156.84	Mahan doublet	0.102	0.45	4.98
β	Bi $4f_{7/2}$	156.98	Voigt doublet	0	0	0.59

of the asymmetric Mahan doublet, as additionally shown in Table 3.3.

Before comparing the amounts of Bi within the three samples, the Bi XPS intensities must be normalized. This is was only done for the α- and the β-phase samples. For the ZLG sample with Bi on top, this normalization is impossible due to the thick layer of Bi on top. This layer prevents the signal from the underlying ZLG or substrate almost completely. Note, that the Bi 4f spectra in Fig. 3.2 are not calibrated, but only the values for A_{Bi} in the panels (b) and (c). For calibration of the A_{Bi} values, the intensity of the Bi $4f_{7/2}$ is divided by the intensity of the bulk C 1s signal. This yields the amount of Bi:

$$A_{\mathrm{Bi}} = \frac{I_{\mathrm{Bi\ 4f_{7/2}}}(\mathrm{Bi}^0)}{I_{\mathrm{C\ 1s}}(\mathrm{SiC'})} \,. \tag{3.4}$$

This value A_{Bi} is used to monitor the changes in the amount of Bi for different annealing temperatures (350°C to 900°C). The change of A_{Bi} with changing annealing temperature is shown in Fig. 3.2 (b) by the black circles. For annealing temperatures from 350°C to 450°C, a rapid loss of Bi is observed. This loss is attributed to the desorption of residual Bi on top of the graphene layer. It is noteworthy that the intercalated and residual Bi cannot be distinguished in the Bi 4f XP spectra due to the lack of an observable chemical shift. When the intercalated sample is annealed to higher temperatures, the amount of Bi is further reduced, but the slope with annealing temperature is greatly reduced. This behavior is consistent with the change in the structure of the Bi layer, observed by Sohn et al. in LEED studies. They found a change from (1 x 1) to ($\sqrt{3}$ x $\sqrt{3}$) with respect to the SiC(0001) substrate [50]. The ($\sqrt{3}$ x $\sqrt{3}$) reconstruction in the β phase can be achieved by either one third or two thirds of the Bi atoms of the α phase. The exact percentage of Bi atoms in the β phase compared to the α phase cannot be distinguished from the XPS

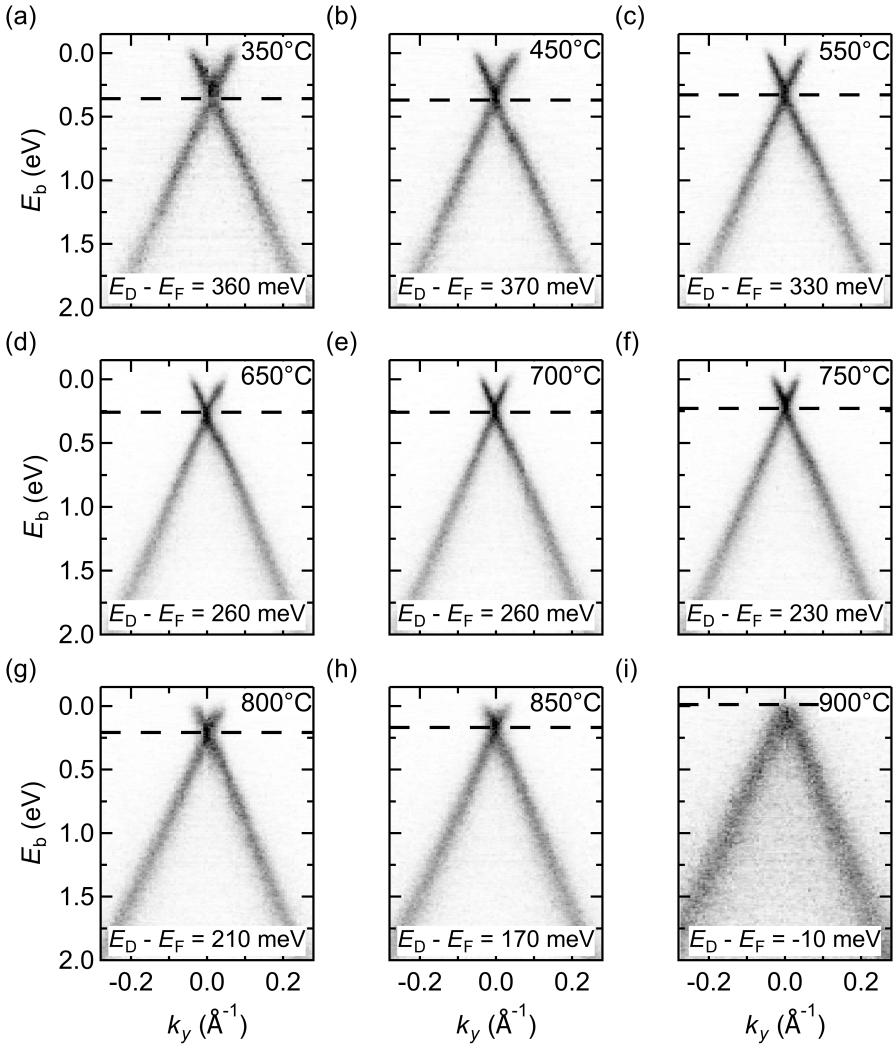

Fig. 3.3: ARPES data at the $\bar{K}$ point of graphene for samples annealed at (a) 350°C, (b) 450°C, (c) 550°C, (d) 650°C, (e) 700°C, (f) 750°C, (g) 800°C, (h) 850°C, and (i) 900°C. The position of each Dirac point is marked by a dashed horizontal line. [98]

results because the exact annealing temperature at which no residual Bi is left on top is not known. However, we observe that the degree of intercalation D does not change proportionally to the loss of Bi atoms. This is shown by the red crosses in Fig. 3.2 (b). Here, even for temperatures up to 900°C, D is still larger than 80% and thus indicates a good intercalation. The fact that the degree of intercalation remains nearly constant while the amount of Bi gradually decreases suggests that the bonding configuration of the Bi is undergoing a transition, becoming more likely to bind with multiple Si atoms. This phenomenon supports the observed shift in the Bi's character from a metallic to an insulating state, as evidenced by XPS analysis.

The change in the intercalant layer also affects the electronic properties of the graphene layer. As depicted in Fig. 3.2 (c), the position in energy of the Dirac point changes with the annealing temperature and thus with the amount of Bi. The EDMs for various annealing temperatures are shown in Fig. 3.3. At an annealing temperature of 350°C (the α-phase sample) the Dirac point is located at 360 meV. At higher temperatures the Dirac cone constantly shifts towards higher binding energies, i.e. at an annealing temperature of 700°C the Dirac cone is at 260 meV. It is noteworthy, that at no annealing temperature the existence of two distinct Dirac cones is observed, although a mixture of the two phases can be seen in LEEM [98]. The shift in the Dirac cone shows a continuous change in the doping from n-type to slightly p-type.

As previously mentioned, is the annealing temperature directly related to the amount of Bi. The change of the energy of the Dirac point with increasing annealing temperatures is shown in Fig. 3.2 (c). In the regime of the green circles, the amount of residual Bi on top changes. The behavior observed here, that the Dirac cone of graphene shifts towards higher energies the more Bi is on top, has already been observed by Gierz et al. [109]. On the other hand, if we focus on the amount of Bi in the intercalation layer, the black circles (see Fig. 3.2 (c)) show a constant shift of the energy of the Dirac cone with the amount of Bi in the intercalation layer. The less Bi is intercalated under the graphene, the higher the energy shift of the Dirac cone. The higher energy of the Dirac cone for the β phase can be explained by the fact, that each Bi atom has to saturate more Si atoms than in the α phase. This reduces the number of free electrons available for doping the graphene layer. However, the continuous change in the energy of the Dirac cone is sur-

prising, since it is known from LEEM studies [98] that in the mixed regime, both the α and β phases coexist. Therefore, for a mixed layer, two different Dirac cones with changing intensity would be expected for the mixture of both phases. This continuously shifting Dirac cone was also seen by Sohn et al. [50] for this system, and was additionally observed for In-intercalated graphene on SiC(0001) [56]. The different observations in LEEM and ARPES could be explained if there is charge spillover from the α-phase regions to the β phase and vice versa. If this charge spillover has a decay length comparable to the domain size of the different phases, only one averaged Dirac point would be observed in ARPES. This averaged Dirac point would then depend on the ratio of the α and β phases and shift in energy accordingly.

3.4 XSW

Having demonstrated successful intercalation and the transition from metallic to insulating properties in the two phases, it is crucial to investigate the vertical structure. This investigation is necessary to better understand how the intercalant bismuth (Bi) layer is bound to the underlying SiC(0001) substrate and the decoupled graphene layer on top. Specifically, it is necessary to determine the vertical bond length and identify the most probable type of bonding (covalent, van der Waals, etc.). Consequently, the NIXSW technique was utilized to ascertain the vertical distances between the layers implicated in the sub-angstrom regime of the two phases.

In a first synchrotron beamtime, both an α-phase and a β-phase sample were transported in air to the Diamond synchrotron facility, as it was believed that all these samples were insensitive to air exposure. To verify this, XP spectra of the two phases were recorded after transport in air. The resulting XP spectra are shown in Fig. 3.4 as dark green dots (α phase) and the blue solid line (β phase). Note that these spectra were recorded under hard X-ray conditions. Therefore, the peak resolution (and consequently, the peak shapes) is less precise than that of the previously discussed soft X-ray spectra. The samples behave differently when exposed to air. While the β phase shows one doublet for the Bi 4f region, the α phase consists of two doublets, one of which is shifted to higher binding energies compared to the β phase. This second doublet indicates the presence

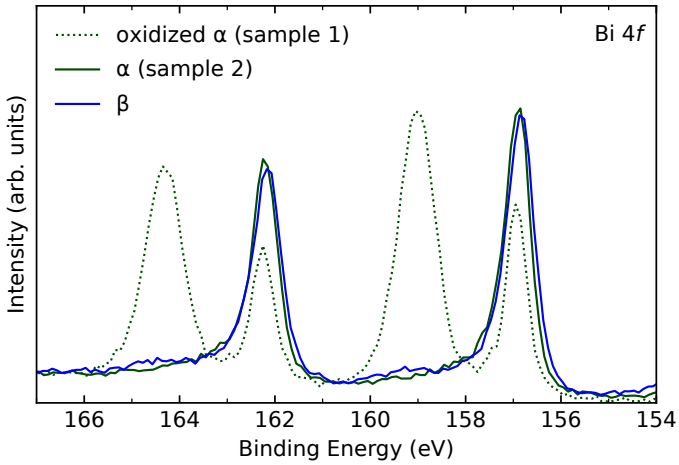

Fig. 3.4: Bi 4f XP spectra of the three samples that were transported to the I09 beamline at Diamond. The first α-phase sample (green dotted line, $h\nu = 2458.0$ eV) and the β-phase sample (blue, $h\nu = 2459.7$ eV) were transported in air. The α-phase sample shows signs of oxidation. Therefore, a second α-phase sample (green solid line, $h\nu = 2458.2$ eV) was transported in vacuum. The following discussion of the data refers to the non-oxidized α-phase sample. The spectra have been normalized for better comparability. The binding energy of the largest peak was set to the binding energy resulting from the XP results in the pre-characterization.

of an oxidized Bi species in the α phase after transport through air. Whether the intercalation layer or residual Bi on top was oxidized during transport cannot be determined from these XP data. To avoid the possibility of erroneous data due to an oxidized intercalant Bi layer, a second α phase sample was later transported to the Diamond beamline in UHV for NIXSW measurements. The XP spectrum of the second α-phase sample is additionally plotted in Fig. 3.4 (dark green line). The vacuum transported sample shows no indication of oxidized Bi. As previously mentioned, the β-phase sample was only transported in air and no Bi was oxidized. Hence, the reason could be that the β phase has a lower amount of Bi on the sample and was prepared by annealing at a higher temperature. Therefore, the remaining Bi on top of the graphene could desorb before

transport in air. Consequently, for the further analysis of the vertical structure, the data recorded for the vacuum-transported α-phase and for the air-transported β-phase sample are discussed below.

For NIXSW experiments, XP spectra and reflectivity curves are measured for the photon energy range around the Bragg energy. Starting with the α phase, an example plot of the XP spectra in the C 1s region is shown in Fig. 3.5 (a). Two peaks are found, one for the graphene in blue (284.15 eV) and one for the substrate carbon atoms in black (282.17 eV). Note that these spectra were measured at a photon energy approximately 10 eV below the Bragg energy (2448.3 eV). In this photon energy range, the energy resolution is worse than for soft X-rays. Therefore, the peaks belonging to still unintercalated regions could not be resolved here. The difference in intensity between data recorded with soft and hard X-rays can be explained by two opposing effects. In hard X-rays, the photon energy is much higher than in soft X-rays. This results in a higher kinetic energy of the photon, allowing it to penetrate deeper into the sample and increasing bulk sensitivity. In contrast, the different geometrical setup causes another effect. Only photoelectrons emitted under grazing angles are detected, resulting in higher surface sensitivity in measurements using hard X-rays. Evidently, the geometric effect is stronger than the effect of kinetic energy. Thus, the signal of graphene is enhanced, while the intensity of the bulk signal is drastically reduced. In addition to the carbon species, the other core levels of interest were investigated. The Bi 4f level is in the same binding energy range as the Si 2s, and so both were investigated in one scan. Here, the α phase shows the known doublet of the Bi 4f with its area ratio of 3:4 of the Bi $4f_{5/2}$ at 161.61 eV and the Bi $4f_{7/2}$ at 156.30 eV. The Si 2s, similar to the C 1s XP spectrum, is lower in intensity and has a binding energy of 151.24 eV.

These XP spectra are recorded for each photon energy step through the Bragg energy. Then, for each spectrum, the signal from each atomic species is fitted separately and its integrated intensity is plotted against the corresponding photon energy. These so-called yield curves for one sample position are shown for all investigated species in Fig. 3.5 (c) shows the yield curves for one sample position for all investigated species.The yield curves are displaced by 2, 4 and 5 in Fig. 3.5 (c), respectively. Additionally, also the reflectivity of the sample is recorded. As described in the Chapter 2, these yield curves

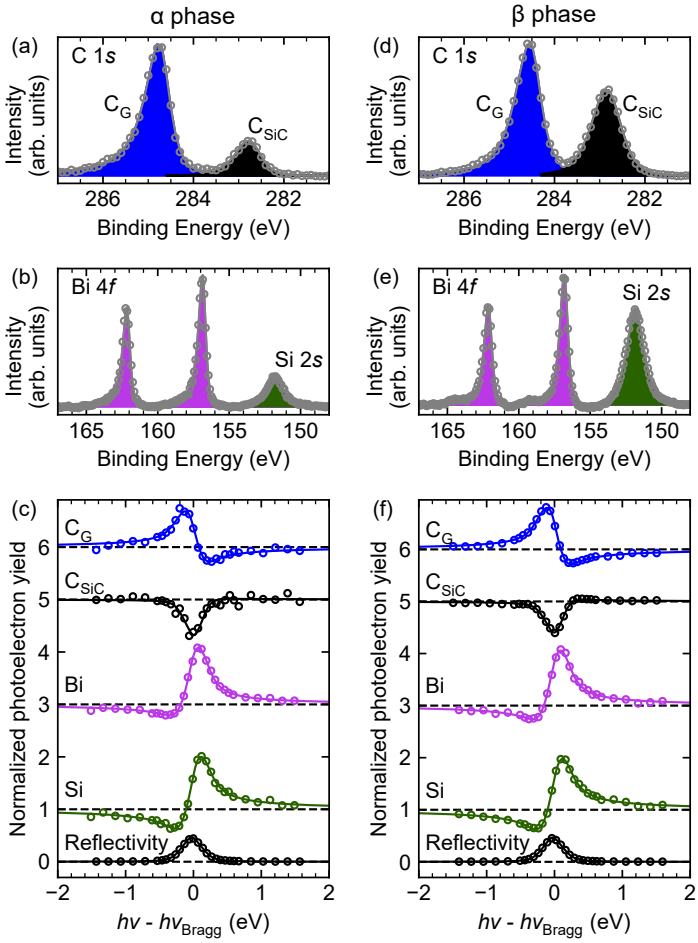

Fig. 3.5: (a, b) Exemplary hard XP spectra of the α-phase of the Bi-intercalated graphene on 4H-SiC(0001) in the off-Bragg condition (hν = 2448.3 eV, 10 eV below the Bragg energy). A Shirley background was subtracted for both spectra. (c) Resulting typical yield curves of the SiC(0004) reflection for the relevant species. These yield curves are displaced by 2 (Bi), 4 ($C_{SiC'}$) and 5 (C_G). (d, e, f) Same as (a, b, c) for the β phase, but on 6H-SiC(0001) (and hence the SiC(0006) reflection). Here, the photon energy for the XP spectra was 2461.1 eV, which is slightly above the Bragg energy.

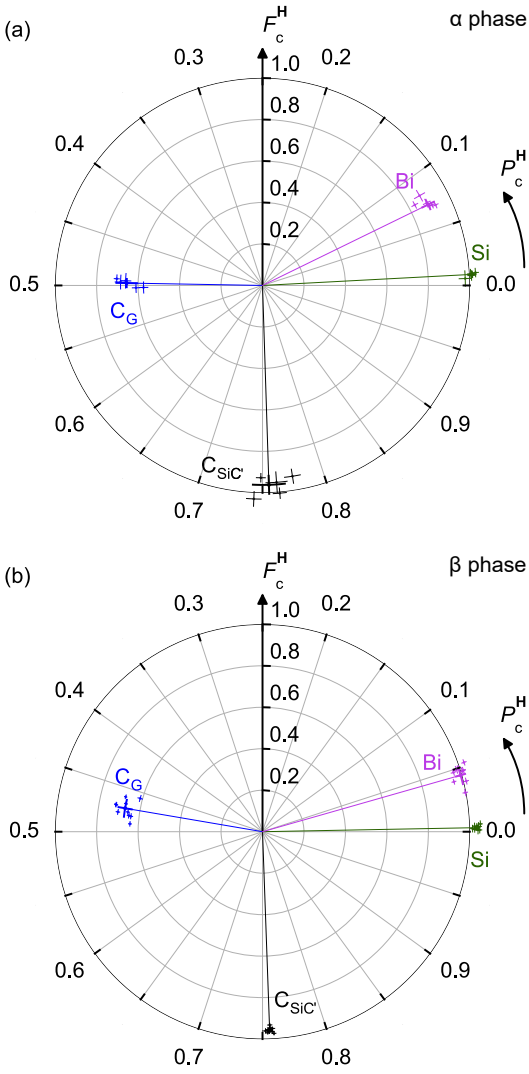

Fig. 3.6: Argand diagram showing the fit results of both the α phase (a) and the β phase (b). The data points reflect measurements at different positions on the sample. The lines towards a larger data point represent the average of the species over all measurements.

can be fitted using equation 2.10, yielding the two parameters coherent fraction ($F_c^{\mathbf{H}}$) and coherent position ($P_c^{\mathbf{H}}$). This procedure was performed for several positions on the sample surface. The resulting coherent positions and fractions are plotted as individual vectors in the so-called Argand diagram, a polar diagram, with the coherent position as the polar angle and the coherent fraction as its length. The Argand diagram for the α phase is shown in Fig. 3.6 (a). For all species, the results of the individual measurements are plotted as small dots with a cross as error bars for the coherent position and fraction. For each species, the data points are hardly scattered, indicating a high homogeneity of the investigated α-phase sample.

The same analysis procedure was applied to the β phase. In Fig. 3.5 (d) the C 1s XP spectrum is shown. The main difference between the β phase and the α phase is the change in the intensity ratio between the graphene and the bulk carbon signal, see Fig. 3.1. This effect is due to the reduced amount of Bi in the intercalant layer and therefore less photon shielding by the Bi atoms. A similar effect is observed for the ratio between the Bi 4f and Si 2s intensities in Fig. 3.5 (e). However, in this case as well, the Bi 4f intensity is generally reduced due to the lower amount of Bi. The peak positions are similar to the α-phase sample. The resulting yield curves do not show much of a change either and thus the Argand vectors are also similar to those of the α-phase sample.

The vertical structure can be determined from the coherent positions, a general model for the layer arrangement and the Bragg distance, $z = d_{hkil}\ \left(n\ +\ P_c^{\mathbf{H}}\right)$ (equation 2.9). For the general model, the layers are arranged from bottom to top. For these two samples, the layers are bulk carbon, bulk silicon, bismuth, and graphene on top. Inserting the experimental data for both phases gives the vertical yields. Thus, the interlayer distances can be determined. The averaged coherent positions, coherent fractions, the used values for n (an integer number) and the resulting vertical heights are listed in Table 3.4. Most interesting are the interlayer distances between graphene and Bi as well as the distance between Bi and Si. For graphene to Bi the distances are 3.59 Å and 3.60 Å for the α and β phases, respectively. These two distances are identical within experimental accuracy. The graphene-Bi distance is almost identical to the sum of the van-der-Waals-radii of carbon and Bi (1.53 Å (C) + 2.07 Å (Bi) = 3.60 Å) [110, 111], while the theoretically

Table 3.4: Averaged values for the coherent position $P_c^{\mathbf{H}}$ and the coherent fraction $F_c^{\mathbf{H}}$, as obtained from several individual NIXSW measurements on the two different phases of Bi-intercalated graphene on SiC(0001). The height z is calculated using the equation $z = d_{\mathbf{H}}^{\mathrm{SiC}}(n + P_c^{\mathbf{H}}(\mathrm{SiC}) - P_c^{\mathbf{H}}(\mathrm{Si}))$, where n is the number of Bragg planes between the considered atomic species and the surface, and $d_{\mathbf{H}}^{\mathrm{SiC}} = 2.52$ Å is the lattice spacing of the Bragg reflection used (for both, 4H- and 6H-SiC substrate). Δ is the distance from two neighboring layers, calculated by the difference of their heights. Parameters used in the fitting procedure: Deviation from perfect normal incidence $\xi = 3.5°$, averaged electron emission angle relative to the incident synchrotron beam $\phi = 80.9°$, non-dipolar correction factors (applicable to s-state emission only) $\gamma'_{\mathrm{C\,1s}} = 1.022$, $\Delta_{\mathrm{C\,1s}} = -0.218$, $\gamma'_{\mathrm{Si\,2s}} = 0.707$, and $\Delta_{\mathrm{Si\,2s}} = 2.645$. For details of the analysis procedure, see Refs. [84, 88]

phase	XP level	$P_c^{\mathbf{H}}$	$F_c^{\mathbf{H}}$	n	z (Å)	Δ (Å)
α	C_G $1s$	0.497 ± 0.005	0.66 ± 0.05	3	6.27 ± 0.01	3.59 ± 0.02
	Bi $4f_{7/2}$	0.072 ± 0.004	0.89 ± 0.04	2	2.68 ± 0.01	2.68 ± 0.01
	Si $2s$	0.008 ± 0.002	1.012 ± 0.002	1	0.0	0.64 ± 0.03
	$C_{SiC'}$ $1s$	0.76 ± 0.01	0.96 ± 0.05	0	-0.64 ± 0.03	
β	C_G $1s$	0.473 ± 0.009	0.67 ± 0.04	3	6.22 ± 0.02	3.60 ± 0.03
	Bi $4f_{7/2}$	0.044 ± 0.007	0.99 ± 0.02	2	2.62 ± 0.02	2.62 ± 0.02
	Si $2s$	0.003 ± 0.002	1.03 ± 0.01	1	0.0	0.62 ± 0.01
	$C_{SiC'}$ $1s$	0.76 ± 0.02	0.96 ± 0.01	0	-0.62 ± 0.01	

calculated sum of the covalent radii (0.75 Å (C) + 1.51 Å (Bi) = 2.26 Å) [112] is much smaller. Thus, a pure van-der-Waals bonding between graphene and Bi is found, confirming the decoupling of the graphene layer from the substrate by the Bi intercalant. The opposite behavior is observed for the distance between Bi and Si, where the measured distances of 2.68 Å for the α phase and the 2.62 Å for the β phase are both close to the sum of the covalent bond radii (1.16 Å (Si) + 1.51 Å (Bi) = 2.67 Å). [112] The sum of the van-der-Waals radii is 4.00 Å(1.93 Å (Si) + 2.07 Å (Bi)). [110, 111] Therefore, it is very likely that the Bi is covalently bonded to the uppermost Si atoms, saturating their dangling bonds. The difference between the two phases is relatively small, but an experimental artifact seems unlikely, because both the graphene and the Bi atom positions are shifted by essentially the same value (0.06 Å for Bi and 0.05 Å for graphene). This small difference could be due to the change of the adsorption site of Bi on top of

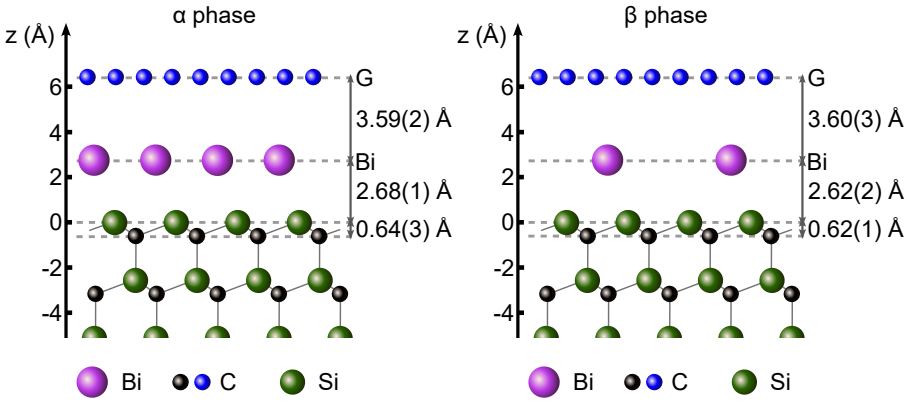

Fig. 3.7: Ball-and-stick models of the vertical structure of the α phase (left) and the β phase (right).

the Si atoms. The exact lateral positioning of the Bi atoms with respect to the substrate cannot be extracted from these data sets, but the vertical structure of both phases is resolved and is shown as a ball-stick model in Fig. 3.7. The lateral positioning of the Bi is based on the model proposed by Sohn et al. [50], but still needs to be confirmed by other methods.

3.5 Summary and Outlook

Two samples of Bi-intercalated quasi-freestanding graphene on SiC(0001) were successfully prepared and characterized with XPS and ARPES. In XPS the successful and complete intercalation was confirmed and in ARPES the decoupling of the former ZLG to quasi free-standing graphene was proven by the appearance of a Dirac cone at the $\bar{K}$ point. NIXSW was used to resolve the vertical structures for both the α and the β phase of Bi-intercalated graphene. Both have a high vertical order and are homogeneous over the entire sample surface. The bond between graphene and Bi is of van-der-Waals character for both phases, while the Bi-Si bond is covalent. While the differences between the α phase and the β phase seem small for the Bi-Si distance, this difference is significant and not within the experimental error. The exact reason for this small dif-

ference can only be speculated. Further investigations using density functional theory may resolve this issue, but it may also be solved experimentally by using XSW imaging [113]. This technique exploits the fact that the coherent position and coherent fraction can be considered as the phase and amplitude of the Fourier components of the electron density of the system under study. If a sufficient number of Fourier components are measured, i.e. XSW data are recorded for a sufficient number of (inclined) Bragg reflections, a Fourier back-transformation is possible, which yields the electron density (in real space) of the atomic species under consideration. With this it is possible to obtain a three-dimensional model of the structure. Thus, it may be possible to solve for the exact lateral positions of the Bi atoms in both phases and gain further insight into the differences between the two phases.

4 Selenium-intercalated epitaxially grown Graphene on SiC(0001)

The acquisition and analysis of the NIXSW data for the first sample has been the author's contribution in this project. The acquisition and analysis of the NIXSW data for the second sample was done by S. Wolff. The sample preparation and characterization with LEED, XPS and ARPES was done by S. Wolff and is published in her dissertation [105].

4.1 Introduction and Motivation

Similar to the discussed possibilities of heterostructures with Bi-based 2D materials, the field of transition metal dichalcogenides (TMDCs) is also increasing in the last decades. TMDCs are two-dimensional (2D) materials with diverse properties, including semiconducting and superconducting properties, depending on their composition and layers. Monolayer TMDCs have direct band gaps, making them ideal for optoelectronic devices such as LEDs and solar cells [114–118]. Combining TMDCs with graphene in van der Waals heterostructures creates new functionalities. Graphene acts as a conductive channel or transparent electrode, and TMDCs provide the necessary bandgap and strong light-matter interaction. This hybrid approach enables tuning of electronic and optical properties, allowing for the creation of high-speed, light-manipulating devices [119, 120]. A combination of graphene and TMDCs could also be useful in spintronic devices [121].

Heterostructures of TMDCs and graphene are so far realized by exfoliation techniques [122–124], which have the disadvantages mentioned above. Therefore, the realization of grown heterostructures by intercalating a ZLG sample with a TMDC material is

very promising. Similar to the successful intercalation of gallium nitride [125], growing TMDCs under epitaxial graphene on silicon carbide (SiC) could create large, uniform, layered systems with precise thickness control. This could significantly impact graphene's electronic properties and open doors to advanced electronics and optoelectronics [118, 121, 126–129]. One interesting option is to intercalate graphene with iron selenide (FeSe), as a single trilayer of FeSe is already known to exhibit superconductivity [130].

Preliminary work on intercalating epitaxially grown graphene with molybdenum disulfide (MoS_2) was conducted in T. Seyller's group. However, this only resulted in partial intercalation of the graphene. There were indications that the sulfur atoms were causing the partial decoupling of the graphene layer [105]. Therefore, it is crucial to first achieve intercalation with selenium in order to later add the metal component. The question then arose as to whether the Se layer forms an ordered structure between the graphene and the SiC substrate. Additionally, identifying the vertical bond lengths can reveal the nature of the Se-graphene and SiC-Se bonds.

4.2 Sample Preparation

As a starting point, a ZLG sample was prepared similar to the procedure described in the Bi-intercalated graphene chapter (PASG assisted). The ZLG is transferred to a two-zone furnace for the intercalation with Se. Tin diselenide ($SnSe_2$) is used as a precursor for the free Se atoms. This precursor is placed in the first zone of the furnace and heated to 400°C. This causes $SnSe_2$ to decompose into gaseous Se and SnSe while the latter remains in the first furnace, the gaseous Se diffuses into the second furnace, where the ZLG sample is heated to 750°C. At this elevated temperature, Se intercalates into the ZLG sample and quasi free-standing Se-intercalated graphene on SiC(0001) is formed. The two-zone furnace is necessary to achieve the required degree of cleanliness and for other experimental advantages, which are discussed in the work of S. Wolff [105].

4.3 Discussion

Both samples of Se-intercalated graphene on SiC(0001) were transferred in UHV to the Diamond facilities and were investigated by means of XSW at the I09 beamline. The measurement routine as well as the analysis procedure is similar to the one described in Chapter 3 for the Bi-intercalated graphene sample.

For the first sample, an exemplary C 1s hard X-ray XP spectrum is shown in Fig. 4.1 (a), where two peaks are observed. These peaks correspond to the decoupled graphene layer (C_G) and the carbon atoms within the SiC substrate ($C_{SiC'}$). The graphene peak is colored in blue and has a binding energy of 283.64 eV, while the substrate C 1s peak, colored in black, is at 282.42 eV. In Fig. 4.1 (c) an example XP spectrum of the Si 2s region is shown. Only one peak is observed, corresponding to the substrate Si atoms. This peak is located at a binding energy of 151.64 eV. The expected core-level shift between the Si atoms in the bulk and the Si atoms directly bound to the Se intercalation layer cannot be resolved due to the 200-300 meV wide bandwidth [131] of the hard X-ray beam at the used 2.4 keV photon energy. The third XP spectrum shown in Fig. 4.1 (b) shows the Se 3s core level. Only one peak is included in the model used for fitting. All fit parameters are shown in Table 4.1. There could be indications of a high energy shoulder but the recorded data has a too low signal-to-noise ratio to be able to clearly distinguish two species here. The peak used is at 229.18 eV.

The data and analysis of the second sample, the unpublished work of S. Wolff, is included here for completeness. As for the first sample, exemplary XP spectra are shown in Fig. 4.1 (d-f). Here, the fitting routine of the hard XP spectra is similar to the soft XP spectra for sample characterization, as discussed in S. Wolff's dissertation [105]. Therefore, additional components (peaks) are used for the fitting of the three regions. This was possible due to the increased signal-to-noise ratio, but the additional components are not shown in the NIXSW analysis, because either the total intensity is too small or no difference in their vertical positions to another species of the same element is observed. For the exemplary C 1s XP spectrum (Fig. 4.1 (d)), in addition to the previously used graphene (G) and substrate peak (SiC'), components for non-intercalated ZLG regions (S1, S2 and SiC) for the two ZLG species and the substrate signal of non-intercalated

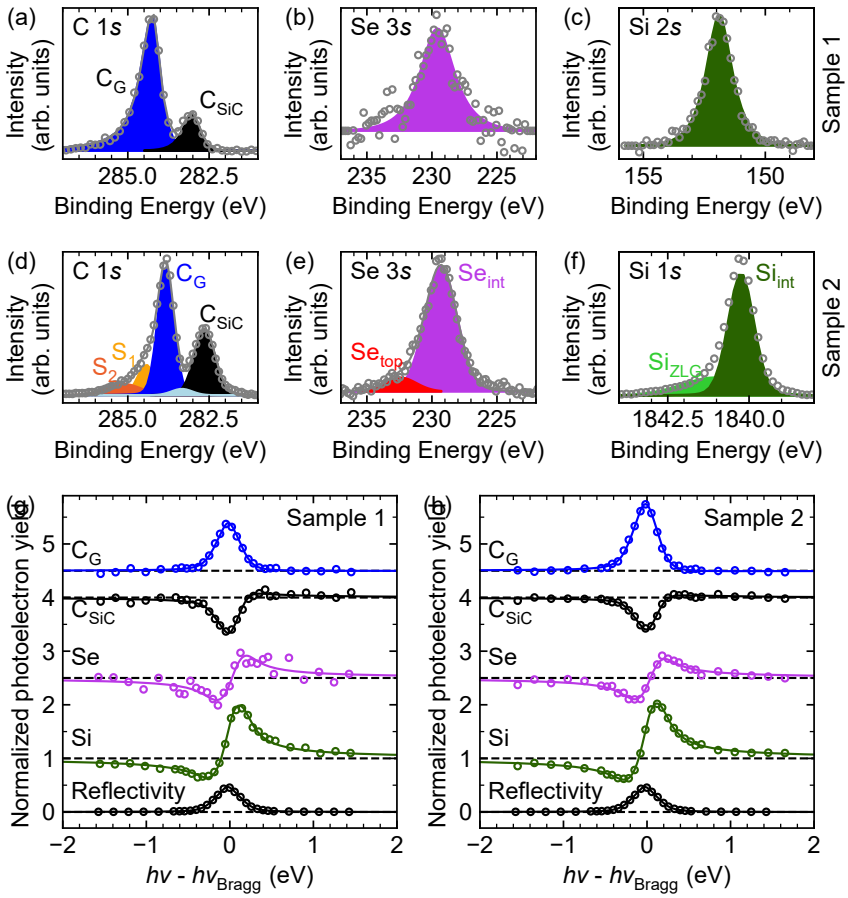

Fig. 4.1: (a, b, c) Exemplary hard XP spectra of the first Se-intercalated graphene on 4H-SiC(0001) sample in an off-Bragg condition (hν = 2468.3 eV, 10 eV above the Bragg energy (2458.3 eV)). A Shirley background was subtracted for both spectra. (g) Typical yield curves of the SiC(0004) reflection for the relevant species. These yield curves are displaced by 1.5 (Se), 3 ($C_{SiC'}$) and 3.5 (C_G). (d, e, f) Same as (a, b, c) for the second sample, (h) same as (g) for the second sample.

Table 4.1: Fit parameters for C 1s, Si 2s, Si 1s and Se 3s core-level from both samples.

	species	XP level	binding energy (eV)	peak shape	FWHM	Asym.	error (χ^2)
1	C_{SiC}	C 1s	282.42	asym. Voigt	0.555	1.2 / 1.0	5.37
	C_G	C 1s	283.64	asym. Voigt	0.559	2.0 / 3.0	
	SiC	Si 2s	151.62	Voigt	1.245	0	3.48
	SiC	Se 3s	229.03	Voigt	3.045	0	1.58
2	S1	C 1s	284.14	Pseudo-Voigt	0.626	0	12.31
	S2	C 1s	285.84	Pseudo-Voigt	1.283	0	
	C_{SiC}	C 1s	283.04	Pseudo-Voigt	0.754	0	
	$C_{SiC'}$	C 1s	282.34	Pseudo-Voigt	0.754	0	
	C_G	C 1s	284.54	Pseudo-Voigt	0.578	0	
	Si_{int}	Si 1s	1839.98	Pseudo-Voigt	0.942	0	13.54
	Si_{ZLG}	Si 1s	1840.78	Pseudo-Voigt	2.410	0	
	Se_{int}	Se 3s	229.03	Pseudo-Voigt	2.898	0	6.53
	Se_{top}	Se 3s	232.13	Pseudo-Voigt	2.898	0	

areas were added.

Similarly, the fitting routine for the Si XPS core level spectrum has been adapted. It should be noted that the Si 1s core level was investigated in contrast to the first sample, where the Si 2s core level was used. For the Si 1s (Fig. 4.1 (f)) two components were used to fit the XP spectra. The dark green peak represents the intercalated area of the substrate, labeled by Si_{int}, and the light green peak represents the non-intercalated regions, labeled Si_{ZLG}. The Se 3s XP spectrum is shown in .Fig. 4.1 (e). Here the situation is slightly different, as there is no Se in the non-intercalated areas. Therefore, the intercalant Se is fitted by one peak, shown in violet and labeled Se_{int}. A small shoulder can be detected on the high binding energy side. It was previously assumed to be present in the first sample, but it could not be resolved due to the low signal-to-noise ratio. This shoulder is attributed to residual Se on top of the graphene layer, but the intensity of the shoulder is very low, making a subsequent NIXSW analysis not very reliable.

The yield curves, which are shown in Fig. 4.1 (g) and (h), respectively, for both samples, are the corresponding peak integrals plotted against their kinetic energy difference from the Bragg energy. After extracting these yield curves, the two fitting parameters, coherent position ($P_c^{\mathbf{H}}$) and coherent fraction ($F_c^{\mathbf{H}}$), can be determined as discussed in Chapter 2 and Chapter 3. Additionally, the reflectivity of the sample is shown. This analysis was performed for all the different sample positions, where NIXSW was measured.

The resulting coherent positions and fractions of all investigated sample positions studied are shown in the Argand diagram in Fig. 4.2 (a). The subsequent discussion of coherent positions and fractions utilizes the averaged values for each species because single measurement spots are limited in size and therefore can only reflect the specific vertical position and vertical order at a certain position on the sample. If the averaged values of several measurement spots do not show a large statistical error, it can be assumed that the majority of the sample is showing this behavior.

For this first sample of Se-intercalated quasi free-standing graphene on SiC(0001), it can be observed that the individual measurements for the carbon and silicon species show very similar positions in the Argand diagram, indicating that the atoms are homogeneously distributed vertically over the sample. For the Se species, the scatter of the data points is slightly larger, but still does not reflect a large discrepancy between different regions of the sample.

The two substrate signals Si and C_{SiC} as well as the Se signal show a large coherent fraction. While this is expected for a bulk species, for the Se layer it shows that the Se atoms are very homogeneously distributed vertically across the sample. However, the graphene signal shows an unusually low coherent fraction of less than 0.4, indicating that the graphene layer is not homogeneously distributed vertically across the sample. Possible explanations will be discussed later.

The Argand diagram for the second sample is shown in Fig. 4.2 (b). Here, a high coherent fraction is observed for all components, with a very homogeneous vertical distribution. The coherent fraction of graphene is also around 0.7, which is a typical value for an epitaxially grown graphene layer on SiC(0001), in agreement with literature [49, 57,

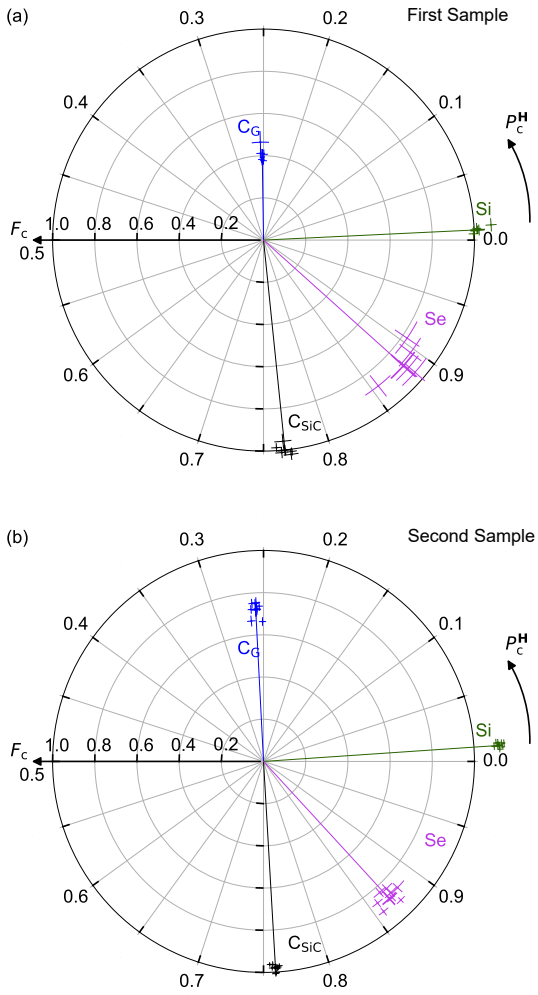

Fig. 4.2: Argand diagrams of (a) the first Se-intercalated quasi free-standing graphene on SiC(0001) and (b) the second sample.

Table 4.2: Averaged values for the coherent position $P_c^{\mathbf{H}}$ and the coherent $F_c^{\mathbf{H}}$, as obtained from several individual NIXSW measurements on the two samples of Se-intercalated graphene on SiC(0001). The height z is calculated using the equation $z = d_{\mathbf{H}}^{\mathrm{SiC}}(n + P_c^{\mathbf{H}}(\mathrm{SiC}) - P_c^{\mathbf{H}}(\mathrm{Si}))$, where n refers to the number of Bragg planes between the considered atomic species and the surface, and $d_{\mathbf{H}}^{\mathrm{SiC}} = 2.52$ Å is the lattice spacing of the used Bragg reflection. Δ is the distance from two neighboring layers, calculated by the difference of their heights. Parameters used in the fitting procedure: Deviation from perfect normal incidence $\xi = 3.5°$, averaged electron emission angle relative to the incident synchrotron beam $\phi = 80.9°$, non-dipolar correction factors (only applicable for s-state emission) $\gamma'_{\mathrm{C\ 1s}} = 1.022$, $\Delta_{\mathrm{C\ 1s}} = -0.218$, $\gamma'_{\mathrm{Si\ 1s}} = 0.344$, $\Delta_{\mathrm{Si\ 1s}} = 2.244$, $\gamma'_{\mathrm{Si\ 2s}} = 0.707$, $\Delta_{\mathrm{Si\ 2s}} = 2.645$, $\gamma'_{\mathrm{Se\ 3s}} = -0.007$, and $\Delta_{\mathrm{Se\ 3s}} = -1.133$. For details of the analysis procedure, see Refs. [84, 88].

	XP level	$P_c^{\mathbf{H}}$	$F_c^{\mathbf{H}}$	n	z (Å)	Δ (Å)
1	C_G $1s$	0.252 ± 0.004	0.39 ± 0.04	3	5.66 ± 0.01	3.45 ± 0.04
	Se $3s$	0.88 ± 0.01	0.89 ± 0.08	2	2.21 ± 0.04	2.21 ± 0.04
	Si $2s$	0.008 ± 0.002	1.02 ± 0.03	1	0.0	0.61 ± 0.02
	$C_{SiC'}$ $1s$	0.766 ± 0.005	1.001 ± 0.005	0	-0.61 ± 0.01	
2	C_G $1s$	0.258 ± 0.004	0.72 ± 0.03	3	5.66 ± 0.01	3.50 ± 0.02
	Se $3s$	0.868 ± 0.007	0.88 ± 0.04	2	2.16 ± 0.02	2.16 ± 0.02
	Si $1s$	0.011 ± 0.002	1.120 ± 0.002	1	0.000	0.63 ± 0.01
	$C_{SiC'}$ $1s$	0.759 ± 0.002	0.98 ± 0.02	0	-0.634 ± 0.005	

98, 132].

Returning to the low coherent fraction of the graphene signal for the first sample, one possible explanation is that the sample is not fully intercalated. This would affect the coherent position and fraction of the graphene in the Argand diagram, since it would be the sum of the partial vectors (vector multiplied by the percentage of the respective area) for the fully intercalated sample and the ZLG (non-intercalated). However, assuming that the second sample is fully intercalated, the position in the Argand diagram of the graphene of the first sample cannot be explained by a mixture of intercalated and non-intercalated regions. If a signal or measurement point in the Argand diagram consists of two components that could not be separated in the XPS spectrum beforehand, then the measurement point is a mixture of the two "ideal" components (perfectly sep-

arated in XPS). This mixture can be traced in the Argand diagram by adding the vector proportions of both components, where the sum of the proportions equals one. This is easily seen in the Argand diagram: the measurement point should lie on the straight line between the points of the two components due to vector addition and the sum of the proportions equaling 1. Since this is not the case for the graphene signal of the first sample, a mixture of intercalated and non-intercalated regions can be ruled out. Another possible explanation for the poor quality of the graphene layer could be the fact that the sample was exposed to air for some time before being transported to Diamond. This could have caused some degradation or oxidation of the sample, especially the Se layer. The presence of atoms between the Se and the graphene would cause the graphene layer to buckle, resulting in a lower coherent fraction.

For easier comparison, a detailed overview of the coherent positions, coherent fractions and resulting vertical positions of all relevant species of both samples is shown in Table 4.2. It can be observed that the coherent positions of the species are very similar for both investigated samples and are always within the error of the method. The most significant difference is evident in the coherent fractions of graphene.

From the coherent positions, the vertical positions can be determined. The resulting distances between the individual layers are shown in a ball-and-stick model in Fig. 4.3 The Se intercalation layer has interfaces with two other layers. First, the distance between Se and the top substrate layer is 2.21(4) Å and 2.16(2) Å for the two samples, respectively. These distances indicate a covalent bond character, because the sum of the covalent radii is 2.32 Å (1.16 Å (Si) + 1.16 Å (Se)) [112] and the van-der-Waals distance would be 3.83 Å (1.93 Å (Si) + 1.90 Å (Se)) [110]. Therefore, the resulting distance is 95% (93%) of the sum of covalent radii. This value below the covalent distance can be explained by the horizontal position of the Se with respect to Si. If Se is sitting not directly on top of the Si atom, the vertical distance can be smaller than the covalent distance. The opposite bonding situation is observed for the distance between graphene and Se. Here, the theoretical covalent bond length is 1.91 Å (0.75 Å (C) + 1.16 Å (Se)) [112] and the van-der-Waals bond length is 3.43 Å (1.53 Å (C) + 1.90 Å (Se)) [110]. The experimental values for both samples of 3.45(4) Å and 3.50(2) Å are 101% and 102% of the van-der-Waals bond length, respectively. This clear van-der-Waals distance is an indication of

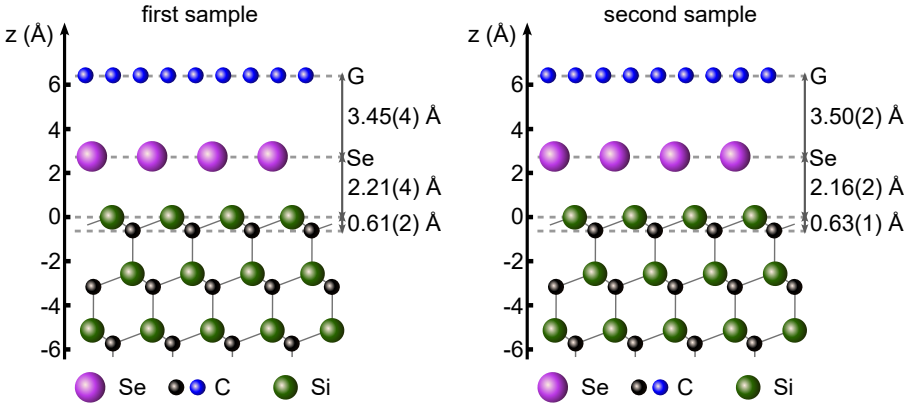

Fig. 4.3: Ball-and-stick model of the vertical structure of the second Se-intercalated graphene sample.

the successful decoupling of the graphene layer from the SiC substrate.

4.4 Summary and Outlook

In summary, two samples of Se-intercalated quasi free-standing graphene on SiC(0001) were prepared and investigated with NIXSW. The first sample showed a low coherent fraction of the graphene layer, due to the inhomogeneous vertical distribution over the sample. Since the low sample quality was most likely due to the prolonged contact of the first sample with air (oxygen), this problem could be solved by preparing the second sample. This shows high coherent fractions for all species. The resulting vertical structure could be determined and shows a van-der-Waals bond between the graphene and the Se intercalation layer. The distance between Se and the substrate indicates a covalent bond. The combination of the likely covalent bond between Se and Si and the van-der-Waals distance between graphene and Se, indicating the decoupling of graphene from the substrate, gives a strong indication that the Se intercalation layer saturates all dangling bonds from the substrate Si.

One open question remaining for the Se-intercalated graphene on SiC(0001) is the in-plane distribution of the Se atoms. It remains unclear whether the Se atoms form a (1x1) reconstruction or are not ordered at all [105]. Hence, XSW imaging investigations are planned to check for the positions of the Se atoms.

5 Epitaxially grown twisted bilayer Graphene on SiC(0001)

The results presented in this chapter are partly published in the following journal article: H. Yin, M. Hutter, C. Wagner, F. S. Tautz, F. C. Bocquet, and C. Kumpf, ”Epitaxial growth of mono- and (twisted) multilayer graphene on SiC(0001)”, Phys. Rev. Materials 9, 044003 (2025). [133]

The sample preparation and the acquisition and analysis of the LEED and ARPES data has been the author's contribution in this project. The paper was written by the author, H. Yin and C. Kumpf. The acquisition and analysis of the LEEM data was done by H. Yin.

5.1 Introduction and Motivation

Most research on twisted bilayer graphene has focused on twist angles close to the magic angle of 1.05° due to its interesting features, such as superconductivity [16, 134]. In contrast, theoretical physicists have theorized a number of intriguing properties of graphene that result from the presence of a substantial twist angle of 20° to 30°. For a long time, it was believed that, for bilayer graphene with a large twist angle, the two graphene layers behave more like two independent graphene layers. However, Pal et al. [76] discovered in their theoretical work that, contrary to this belief, a strong interlayer coupling is expected. This leads to three different phenomena. First, the strong interlayer coupling, together with the specific geometry of the moiré pattern, leads to geometric frustration. This geometric frustration forces electrons to localize within a large-scale network of topologically protected states. Topological protection refers to the stability and robustness of electronic states against minor disturbances within the

system. Second, the geometric frustration and resulting electron localization lead to flat bands forming in the electronic structure, demonstrating the electrons' greater independence from their momentum. This indicates the low kinetic energy of the electrons in these flat bands. Third, the presence of these flat bands indicates that electron-electron interactions dominate over the electrons' kinetic energy. These strong interactions lead to correlated physics, which can result in a variety of phenomena, including superconductivity, Mott insulating, magnetism, or heavy fermion behavior, for example. Based on these results, they proposed separating the system into alternating gapped and non-gapped areas [16, 71, 76, 134–137].

Park et al. also explore interesting phenomena in large-angle TBLG in their theoretical work [75]. The authors predict that TBLG is a higher-order topological insulator, which leads to the formation of corner states – zero-dimensional (0D) localized modes at the corners. The authors demonstrate that intervalley scattering opens a bulk gap in TBLG at large commensurate angles, resulting in the occurrence of these topological corner states at half filling. A key finding is that the emergence of these corner states is robust and independent of specific large angles, provided that the underlying symmetries remain intact. TBLG is presented as a strong candidate for the experimental detection of higher-order topological insulator phases, particularly because the corner states appear at half-filling. Furthermore, the corner states are shown to be robust against disorder [75].

In order to experimentally observe the previously discussed theoretical findings, it is crucial to reproducibly grow twisted bilayer graphene epitaxially on SiC(0001) with an exact 30° twist angle [1, 77, 138–140]. This twist angle precision can hardly be achieved by mechanical exfoliation and stacking, which also has other potential risks, as it will be discussed in the next chapter. Therefore, the question arises: How can epitaxial TBLG be grown optimally, and what effect does the exact annealing temperature have on the resulting sample quality? This chapter discusses the effect of a small change in annealing temperature on the structure of epitaxially grown twisted bilayer graphene. The changes in the two prepared samples are investigated using LEED, ARPES and LEEM.

5.2 Sample Preparation

For this investigation, two different samples were prepared using N-doped 6H-SiC(0001) wafers from SITUS Technicals GmbH. The preparation was performed in four steps. First, the wafer piece is thoroughly degassed at 880°C until the pressure in the UHV chamber drops below 10^{-9} mbar. In this case, 30 minutes were sufficient. Next, the sample is annealed at 1050°C for 30 minutes to remove oxides and other contaminations from the substrate. These annealing conditions are well-known and may vary slightly depending on the experimental setup [141]. Additionally, an external supply of silicon (Si) atoms is needed to avoid the sublimation of silicon from the surface; this supply can be achieved by heating a silicon wafer close by [1, 32, 142, 143]. The successful cleaning of the surface can be verified using LEED measurements. Fig. 5.1 (a) shows the LEED image of this preparation step. A Si-rich $(\sqrt{3} \times \sqrt{3})$R30° reconstruction can be observed on SiC(0001), exemplarily. The spots are very sharp, indicating a clean and well-ordered surface. Two spots of the substrate and two of the reconstruction are marked by colored circles, respectively. The color assignment to the different structures is shown in Table 5.1.

In the third step, the sample is annealed again at 880°C for 30 minutes, but with the external supply of Si atoms, to create an even more Si-rich (3×3) reconstruction on SiC(0001). These parameters were empirically found and have also been reported previously [1, 141]. Deviating from these conditions can result in poorer quality of the (3×3) reconstruction. A high-quality (3×3) reconstruction is essential for the subsequent graphene preparation, as its quality influences that of the epitaxially grown

Table 5.1: Assignment of diffraction spots for LEED pattern in Fig. 5.1

Step	Color	Involved Structures	Reconstruction
First Step	Red	SiC	(1×1)
	Yellow	Si on SiC	(3×3)
Second Step	Red	SiC	(1×1)
	Orange	Si on SiC	$(\sqrt{3} \times \sqrt{3})$R30°

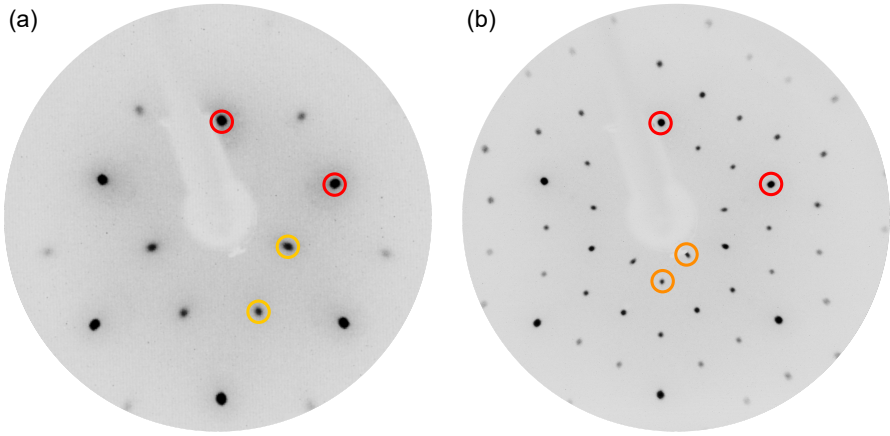

Fig. 5.1: LEED patterns of the (a) $\left(\sqrt{3} \times \sqrt{3}\right) R30°$ reconstruction and (b) (3×3) reconstruction on SiC(0001). Two substrate spots are marked with red circles and two spots for the reconstructions are marked with yellow (a) and orange (b) circles, respectively. LEED images were recorded at an electron energy of 100 eV.

graphene. The size of the terraces and the number of defects in latter grown graphene can be affected by small terraces in the (3×3) reconstruction or by surface oxides remaining on the substrate [32, 142, 143]. Hence, it is important to check the LEED pattern again (Fig. 5.1 (b)). In this case, the pattern shows very sharp spots, indicating a well-ordered, clean surface. The substrate and reconstruction spots are marked again with colored circles and their assignment can be found in Table 5.1. If the LEED pattern of the (3×3) reconstruction does not show the desired quality, then the second and third steps must be repeated until the surface quality seen in the LEED pattern is good. In this case, only one cycle was needed to prepare both samples.

The difference in the preparation of the two samples is the last step, where the graphene layers are grown. There are two routines of growing unconventionally oriented graphene on SiC(0001) which have been shown by Bocquet et al. [1] and others [77, 144]. For both procedures borazine is needed, because upon annealing it is forming hBN on the SiC surface. This hBN is aligned with the substrate's crystalline orientation (rotated

by 0°), while conventionally grown graphene on SiC(0001) shows a 30° rotation with respect to the substrate. This different alignment of hBN can be used to also influence the rotation of the top-most graphene layer grown on SiC(0001). The first routine, which is known as the "template method", consists of two preparation steps. The SiC(0001) is first annealed at around 1050°C in a borazine atmosphere to grow an epitaxial hBN layer on SiC. The following annealing at a much higher temperature of 1600°C triggers the replacement of the hBN layer by a graphene layer, while conserving the crystalline orientation of hBN [77, 144]. The quality of the graphene layer is limited by the quality of the previous hBN layer. Bocquet et al. [1] demonstrated that this process can be improved by performing this in one step. Instead of growing the hBN layer as a template, the sample is directly annealed at around 1300°C in a partial pressure of borazine of 1.5×10^{-6} mbar for 30 min. During the annelaing, the borazine molecules act more like surfactants as there is no hBN layer formed due to the higher temperature, but they force the formed graphene layer to be aligned with respect to the substrate (rotated by 0°) [1]. In this work, two different samples were prepared using the surfactant method described by Bocquet et al. [1]. The only difference in the preparation of the two presented samples is the temperature during the annealing in borazine. The first sample was annealed 1330°C, while the second one was annealed at 1380°C. In the following the sample annealed at 1330°C will be referred to as the low-T sample, and the sample at 1380°C as the high-T sample.

The LEED investigations were performed with an OCI LEED (BDL800IR). For ARPES, a Scienta VUV-5k He-lamp (He-I) was used to excite the photoelectrons, which were then detected by a Scienta R4000 hemispherical analyzer.

5.3 LEED

To determine the presence and quality of graphene, as well as its orientation, both samples were examined using LEED. Additonally, the surface quality was inspected. The resulting LEED patterns for both the low-T and high-T samples are shown in Fig. 5.2 (a) and (b), respectively.

Regarding the LEED pattern of the low-T sample, seven different sets of spots can be

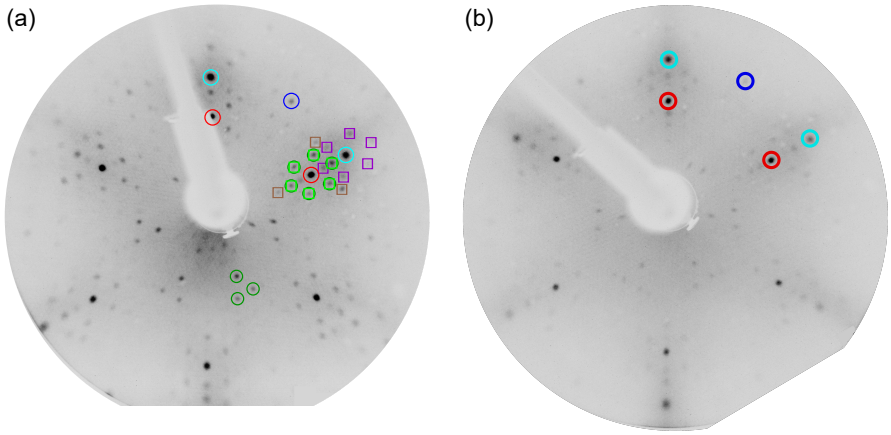

Fig. 5.2: LEED patterns obtained from the surfaces of both samples after the graphene preparation. (a) low-T sample, and (b) high-T sample. The substrate spots are marked by red circles, the Gr-R0° by cyan circles, and the Gr-R30° by dark blue circles. The additional5.2. LEED images were recorded at an electron energy of 100 eV.

identified and marked in different colors in Fig. 5.2 (a). The assignment of the spots, and the corresponding reconstructions with respect to the substrate are illustrated in Table 5.2.

Two diffraction spots of the substrate (SiC(0001)) are marked with red-colored circles. Note, that the (00) diffraction spot is not visible in the presented LEED images because the electron gun of the LEED apparatus, the white obstacle in Fig. 5.2, is blocking the view. The other intense spots are marked in cyan circles and form an hexagonal pattern. The cyan spots are aligned with respect to the red substrate spots in azimuthal direction, but they have a larger reciprocal lattice vector. Therefore, the cyan spots can be attributed to the unconventionally oriented graphene layer grown in the surfactant-mediated method. Since this graphene layer is rotated 0° with respect to the substrate,

it is named Gr-R0° in the following. It needs to be mentioned that the graphene layer is incommensurate to the SiC substrate. The spots marked with blue circles have the same reciprocal lattice vector length as the cyan spots, but are rotated by 30° with respect to the substrate. Therefore, these blue circled spots can be assigned to a second graphene layer, but with 30° crystalline orientation, or graphene-like zeroth-layer which is an intrinsic component located between the epitaxial graphene layer and the SiC substrate. Hereafter, the conventional epitaxial graphene layer with a 30° orientation is referred to as Gr-R30° and the graphene-like zeroth layer as ZLG-R30°. Only from the blue spots, these two structures can not be distinguished [1, 29, 30, 77, 144].

Another hexagonal pattern can be observed around the SiC substrate spots, which is marked by dark green circles. Additional to the hexagonal pattern around the substrate spot, a triangular pattern closer to the (00) spot is observed. All these spots are part of the $(6\sqrt{3} \times 6\sqrt{3})$R30° reconstruction, which is due to the formation of the zeroth-layer graphene. In the zeroth-layer graphene a third of the carbon atoms is still covalently bonded to the substrate, which causes the reconstruction on the one hand to be commensurate, but on the other hand, forces a corrugation onto the layer, because the two hexagonal lattices of SiC and graphene do not fit in a commensurate way. This corrugation has also been observed in former STM and theory works, and was shown to be a (6×6) reconstruction [29, 30, 145, 146]. All the spots belonging to this corrugation are on the $(6\sqrt{3} \times 6\sqrt{3})$R30° grid, but not all $(6\sqrt{3} \times 6\sqrt{3})$R30° spots are (6×6). The visible spots of the $(6\sqrt{3} \times 6\sqrt{3})$R30° which are also belonging to the (6×6) corrugation are marked with light green squares additionally to the dark green circles of

Table 5.2: Assignment of diffraction spots for LEED pattern in Fig. 5.2

Color	Involved Structures	Reconstruction
Red	SiC	(1×1)
Cyan	Gr-R0°	incommensurate
Blue	Gr-R30°	incommensurate
Dark Green	ZLG-R30°	$(6\sqrt{3}$x$6\sqrt{3})$R30°
Light Green	SiC + ZLG-R30°	(6×6)
Purple	ZLG-R30° + Gr-R0°	incommensurate
Brown	SiC + Gr-R0°	incommensurate

the $(6\sqrt{3} \times 6\sqrt{3})$R30° reconstruction. There are two more sets of spots observed in the LEED image (Fig. 5.2 (a)) which can only be explained by multiple scattering events. The purple marked spots are caused by multiple scattering at the ZLG-R30° and the Gr-R0°, while the brown spots are caused by the multiple scattering at the Gr-R0° and the SiC substrate. Both of these reconstructions are incommensurate because two layers incommensurate to each other are the origin of the two reconstructions [1, 29, 30, 77, 144].

The spots of the substrate and the two kinds of graphene with different crystalline orientation are also observed on the high-T sample. They are marked in the same way as for the low-T sample (substrate: red, Gr-R0°: cyan, Gr-R30°: blue). One major difference to the low-T sample is the intensity changes of several spots: the substrate spots, the spots of the $(6\sqrt{3}$x$6\sqrt{3})$R30° reconstruction, and the spots resulting from multiple scattering effects. The reduced intensity of the spots from the ZLG-R30° could be either caused by the decoupling of the ZLG-R30° from the surface and hence the loss of the ZLG-R30° layer or by the growth of additional graphene layers on-top, which result in a damping of the signal from the lower-lying layers. If the sample is not intercalated as it was exemplary shown in Chapter 3 and 4, the ZLG-R30° can not be converted into a graphene layer without growing a new ZLG-R30°. Hence, the loss of intensity has to be due to the growth of additional graphene layers on top. The growth mechanism upon annealing of the SiC substrate always results in the existence of a ZLG. Therefore it can be assumed that the amount of graphene on top of the SiC(0001) surface and the ZLG is higher than for the low-T sample.

5.4 ARPES

In addition to the structural investigations using LEED, the electronic structures of the two samples were examined using ARPES. The ARPES data obtained from both samples are shown in Fig. 5.3. Panels (a) and (c) show the energy distribution map (EDM) of the low-T and high-T samples, respectively, at the expected position in K-space of the characteristic Dirac cone of Gr-R0°. For the low-temperature sample, the characteristic Dirac cone is observed, showing the typical linear dispersion close to the Fermi level (0 eV). This Dirac cone clearly indicates the presence of a decoupled graphene layer with rotational alignment to the substrate (0°). It is apparent that the intersection

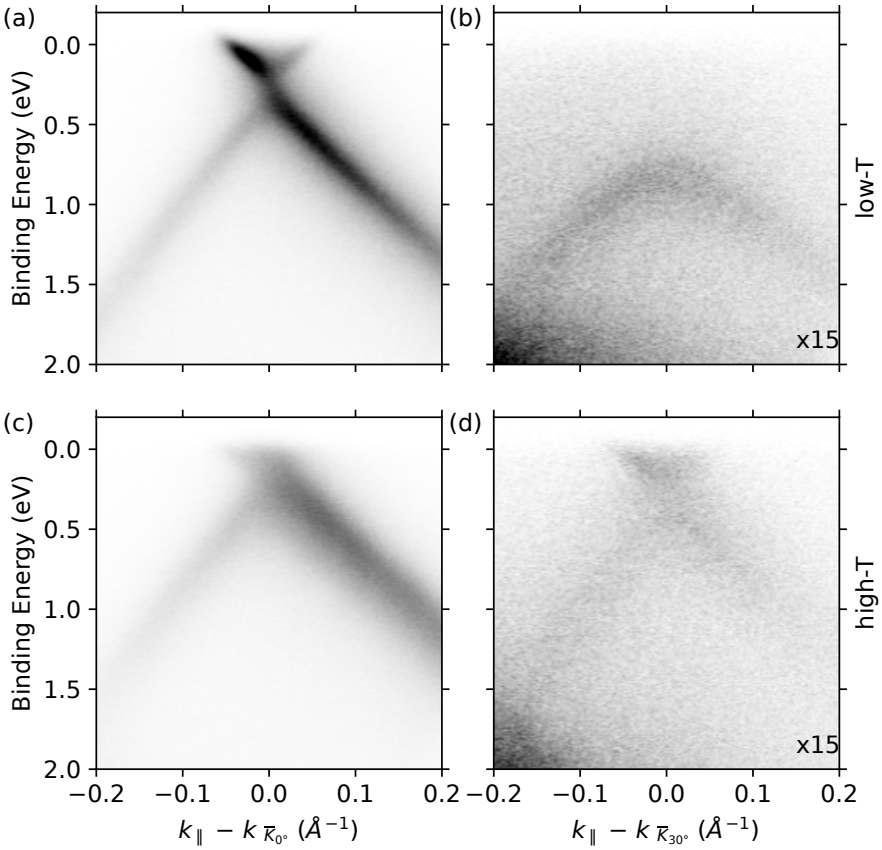

Fig. 5.3: (a, b) ARPES EDMs recorded at the $\bar{K}_0$ and $\bar{K}_{30}$ points of the graphene layers along the $\bar{\Gamma}\bar{K}$ direction of the low-T sample, respectively. (c, d) Same as (a, b) for the high-T sample.

of the two branches of the Dirac cone is not precisely at the Fermi level, but rather at an energy of approximately 300 meV. The shift towards lower energy indicates that the graphene is n-doped [147]. Upon closer inspection of the Dirac cone, it becomes apparent that the intersection of the two branches is not a single point, but an elongated kink.

This behavior has been discussed in the literature and is explained by electron-plasmon and electron-phonon coupling [148–150]. In addition to the kinks, it is also noteworthy that both branches are clearly visible, albeit with different intensities. In the literature, one branch is often barely observed in ARPES, the so-called ”dark corridor”. Gierz et al. demonstrated that the illumination of the dark corridor of graphene depends on the polarization and energy of the photon beam used [151]. The generated photons (He-I) were primarily s-polarized due to the geometry of the ARPES apparatus. This resulted in both branches being visible, with the branch farther from the $\bar{\Gamma}$ point being more intense [151].

The same region in K-space was investigated for the high-T sample. The EDM is shown in Fig. 5.3 (b), where the characteristic Dirac cone was also found. Therefore, it can be concluded that a layer of Gr-R0° is also present on the high-T sample. The observed doping level of Gr-R0° for the high-T sample is slightly less n-doped, with the Dirac cone located at approximately 200 meV. Notably, the Dirac cone of the high-temperature sample is less intense than that of the low-temperature sample. However, the reason for this difference is unclear at this point. One possible explanation is that a less homogeneous sample could result in less intensity of the Dirac cone. Another possibility is that the intensity of photoelectron spectroscopy can vary for different samples due to slightly different setups and the fluctuations in the He-lamp.

The electronic structure of both samples at the $\bar{K}_{30}$ point was also investigated on both samples using ARPES. The resulting EDMs are shown in Fig. 5.3 (b) and (d) for the low-T and high-T sample, respectively. First, looking again at the low-T sample, a band is observed. This band does not show linear dispersion, but rather parabolic behavior. Therefore, it cannot correspond to a Gr-R30° layer on the sample. Most likely, the observed band is from the Gr-R0° band close to the $\bar{M}$ point of Gr-R0°, which has the same position as a Dirac cone from Gr-R30°. Note that the intensity of this band has been enhanced by a factor of 15 compared to panel (a) for visual clarity. A completely different picture emerges for the high-T sample. Here, the characteristic Dirac cone of Gr-R30° is present. This cone clearly proves the existence of Gr-R30° on the high-T sample. Note that the intensity was again enhanced by a factor of 15. This lower intensity could indicate that Gr-R30° is below Gr-R0° due to damping of the photoelectrons

by the top layer or that the amount of Gr-R30° is much lower than the amount of Gr-R0°. Neither the ARPES nor the LEED results provide information about the number of graphene layers with the two different rotations. Therefore, the two samples were transferred to a LEEM apparatus to examine their morphology and layer number.

5.5 LEEM

LEEM images of both samples are depicted in Fig. 5.4. Each has a field of view of 30 μm and represents the surface morphology observed on both samples over a larger area (>200 μm). The surface of the low-T sample is highly uniform. Its dominant features are parallel lines that extend continuously across the field of view. These lines are identified as step edges, which define the boundaries of surface terraces on the SiC substrate. The consistent parallelism and continuity of these step edges suggest an ordered surface structure. Additionally, the surface of the low-T sample has a small number of dark spots that are interpreted as isolated defects.

In contrast, the surface of the high-T sample demonstrates a greater degree of inhomogeneity. The image reveals variations in brightness and darkness on a sub-micrometer scale, indicating spatial non-uniformities. Although the step edges are still visible, they appear fainter and less distinct than those of the low-T sample. These step edges are discontinuous and have a significantly higher density. This increased density and fragmentation suggest that the SiC substrate's step morphology underwent more pronounced restructuring or roughening during annealing at a higher temperature. Additionally, the surface of the high-T sample has a higher density of dark contamination spots. These spots are generally smaller than the defects observed on the low-temperature surface.

Further details about the regions with different contrast can be found in the LEEM-IV curves, particularly in the number of minima within the displayed energy range. The number of minima corresponds to the number of graphene layers on the SiC substrate. Note that this assignment of minima to layers is only valid for epitaxially grown graphene on SiC(0001) [31, 34, 152–154]. Hence, LEEM-IV measurements were used to investigate the stacking configuration of the graphene layers on both samples at a

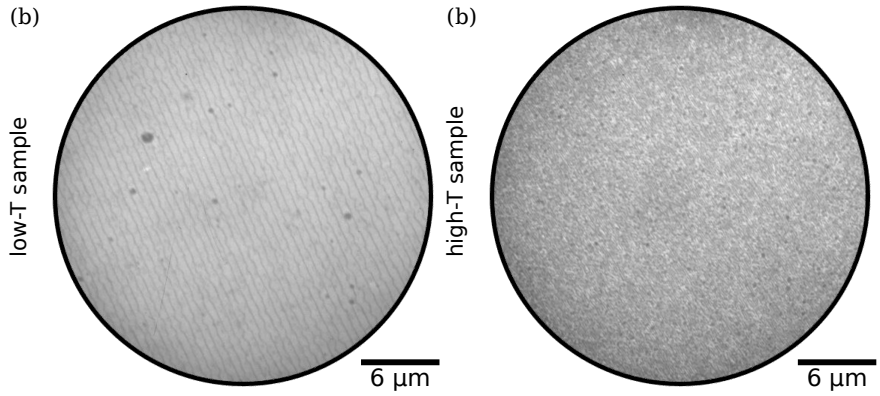

Fig. 5.4: (a) Bright field (BF) LEEM image of the low-T sample, taken at an electron energy (start energy) of 1.66 eV with a field of view (FoV) of 30 µm. (b) Same as (a) but for the high-T sample.

spatial resolution. In LEEM-IV measurements, LEEM images are recorded at various electron energies, and then the intensity of each pixel in the stack of LEEM images is plotted against the electron energy. First, the low-T sample will be discussed. The LEEM image of the area selected for LEEM-IV is shown in Fig. 5.5 (a). It has a smaller section size of 9.0 x 7.5 µm, and the energy range was set to 0 - 5.9 eV in 0.1 eV increments. The image in Fig. 5.5 (a) is from the LEEM-IV stack at E = 2.5 eV from the low-T sample. This energy was chosen because the terraces, step edges and defects can be well distinguished. Note that the step edges are brighter than the terraces at this energy. In addition to the homogeneous, dark grey terraces, dark and white lines and defects are also observed at this electron energy (2.5 eV). The white lines originate from the step edges of the SiC(0001) surface.

At each pixel of this LEEM image, a LEEM-IV curve with a starting energy from 0.0 to 5.9 eV was recorded. LEEM-IV data are usually processed by selecting several regions with the same contrast, integrating them, and coloring the different regions for visualization. However, this method often fails to accurately reflect the transition areas from one region to another. To avoid this potential issue, the data was processed pixel-by-pixel.

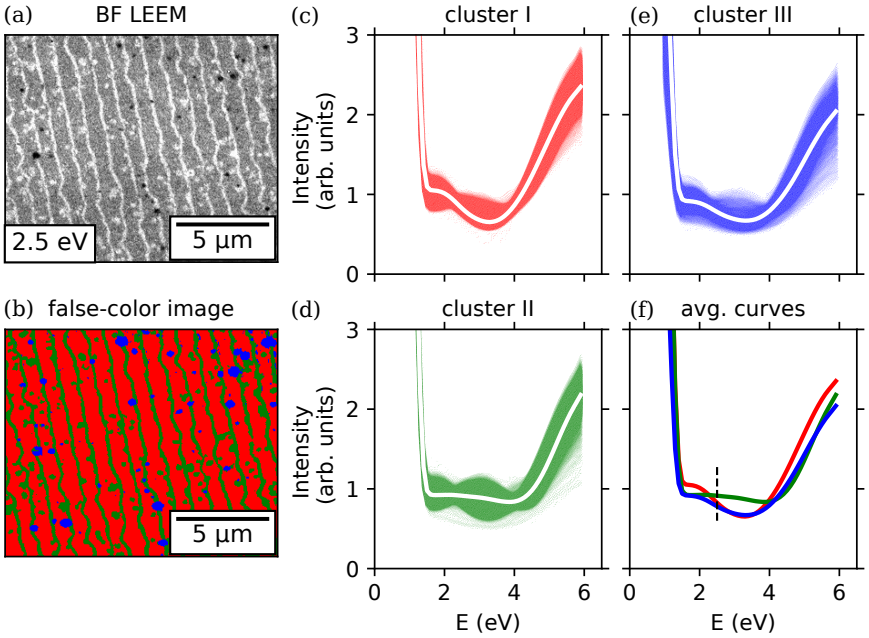

Fig. 5.5: (a) BF LEEM image of the low-T sample, recorded at $E = 2.5$ eV. LEEM-IV data ($E = 0$ to 6 eV) were recorded for this surface area. (b) False color image showing the clustering of the LEEM-IV curves. (c-e) All LEEM-IV curves measured for the surface area shown in (a). They have been assigned to three clusters using the *K-means* algorithm. The white curves in the middle of each cluster represent the average of all spectra assigned to that cluster. (f) Average curves of the three clusters (red: cluster I, green: cluster II, blue: cluster III).

Afterwards the K-means clustering algorithm was implemented to process the LEEM-IV dataset [155]. Further details on the implementation of the K-means algorithm for LEEM-IV analysis can be found in Ref. [133]. This K-means algorithm was used to assign these curves to three clusters. The pixels corresponding to each data point were colored according to their cluster assignment, as it is shown in Fig. 5.5 (b). Most of the pixels were assigned to cluster I (colored red). This cluster corresponds to the homogeneous, grey terraces seen in the BF-LEEM image. Cluster II (colored green) contains the white defects and step edges, while cluster III (colored blue) contains the dark defects.

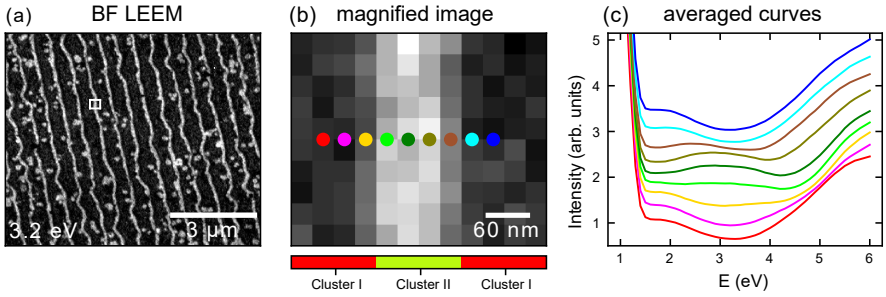

Fig. 5.6: (a) A bright-field LEEM image of the same area shown in Fig. 5.5 (a) but recorded at an electron energy of 3.2 eV. At this energy, the contrast between the step edges and the terraces is more pronounced. (b) A magnified portion of the image in (a), indicated by the white rectangle, showing a vertical step edge. The image size is 360 x 300 nm^2 (12 x 10 pixels). The colored dots mark nine pixel columns, each containing ten pixels, oriented parallel to the step edge. The red and green bars at the bottom of the image indicate which cluster the pixels in the corresponding columns were assigned to in Fig. 5.5 (b). The vertical dashed white lines mark the borders between clusters I (red) and II (green). (c) Averaged LEEM-IV intensities from the marked columns in panel (b). Neighboring spectra are vertically displaced by 0.3. The color coding corresponds to the colored dots in panel (b).

The corresponding false color image of the LEEM image is shown in Fig. 5.5 (b). This cluster mapping shows a homogeneous sample across the terraces, as it was already expected from the BF-LEEM image.

The LEEM-IV curves in cluster I exhibit a shoulder at approximately 1.5 to 2.0 eV, as well as an intense minimum around 3.2 eV. These features are characteristic of monolayer graphene grown on SiC. Therefore, LEEM-IV indicates that the majority of the observed region is an unconventionally oriented single graphene layer (Gr-R0°) on top of the ZLG-R30°.

To identify cluster II, it is neccessary to examine closer the areas where Cluster I borders Cluster II. Therefore, Fig. 5.6 provides a closer look at one of these borders. Fig. 5.6 (b) is a zoomed-in image of Fig. 5.6 (a), showing the area marked by the white rectan-

gle. This image shows the transition from one terrace to the next via the step edge. Two dashed white vertical lines mark the borders between the different assignment to clusters I and II. To understand the change in LEEM-IV profiles across the step edge, the corresponding LEEM-IV curves are shown in Fig. 5.6 (c). Note that the LEEM-IV curves shown are averaged across each column of the image in Fig. 5.6 (b). The colors used for the curves correspond to the marked spots in Fig. 5.6 (b). These LEEM-IV curves do not show an abrupt change in profile, but rather a gradual transition from the profile across the terrace. First one minimum is observed, then a mixture of a flat line and two minima around the step edge, and in the end again the single minimum is seen on the next terrace. These two minima suggest the presence of two graphene layers at this point, which differs from the single graphene layer on the terraces. Therefore, it can be concluded that growth of the second layer is beginning at the step edges and expanding over a range of 150 nm. Note that the LEEM instrument's resolution is much lower than the pixel size shown, so this constant change does not result from a mixture of two areas. Further experiments with longer annealing times have also shown that the growth of the second layer continuously increases further away from the step edges. However, before a complete second layer forms, a third layer starts to grow again at the step edge.

Cluster III represents the dark spots in the BF-LEEM image and corresponds to defects in the terraces. The LEEM-IV curve of cluster III is a combination of the LEEM-IV curves of cluster I and II. For the energy range of 2 to 4 eV, cluster III has the same minimum at around 3.2 eV as cluster I. However, the LEEM-IV curve of cluster III shows the behavior of cluster II below and above this energy range. Note that Cluster III is mainly visible in the LEEM image at an energy of 2.5 eV. This is not the case for most other energies below 6 eV.

As it was already evident from the large-area BF-LEEM image shown in Fig. 5.4 (b), the sample appears to be inhomogeneous. To understand the differences in contrast, LEEM-IV measurements were also performed on the high-T sample. They were again analyzed pixel-by-pixel and a clustering using the K-means algorithm was tried. However, the clustering of the different LEEM-IV curves into a physically reasonable number of clusters failed. Hence, pre-clustering into a manageable number of clusters was performed (in this case, 100 clusters). These clusters were then manually assigned to

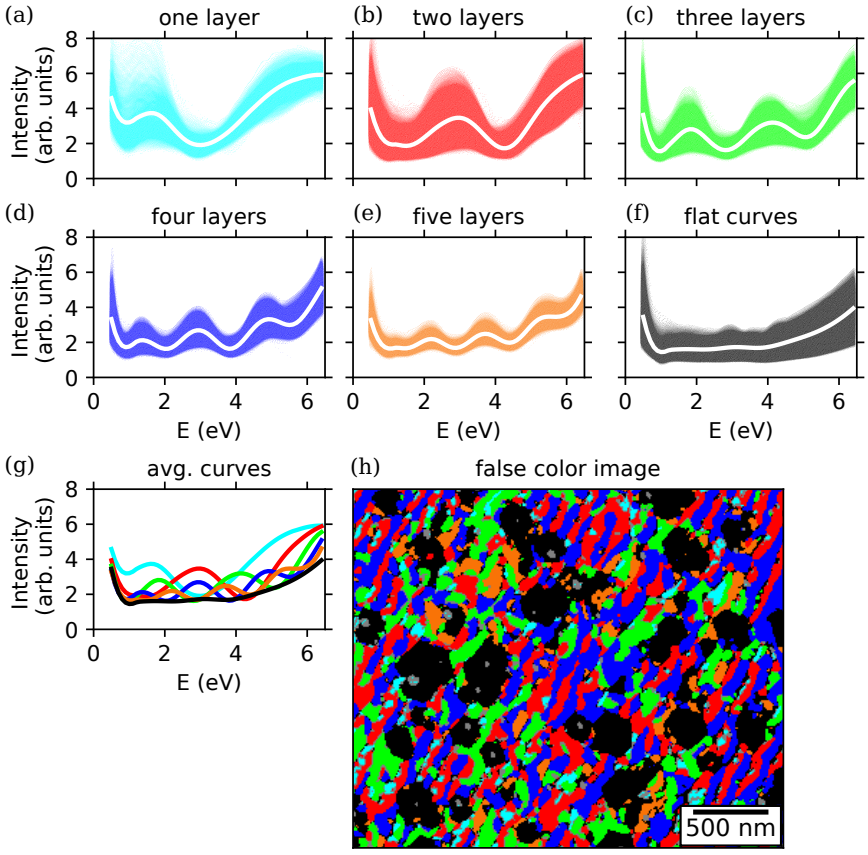

Fig. 5.7: Results of the clustering of LEEM-IV curves recorded for the high-T sample using the *K-means* algorithm. (a-f) Bundles of spectra that were sorted into six different classes, indicating graphene stacks consisting of one, two, ... five and more than five layers. The opacity of all curves is set to 0.01. White curves represent the average intensity of each bundle. (g) Average curves of each cluster (white curves from (a-f)). (h) False color representation of the surface area that was selected for the LEEM-IV analysis.

fewer groups based on the number and energy position of their minima. Inaccuracies in the clustering are, of course, possible when the assignment is done manually. This assigning resulted in a total of six clusters, one for each of the first five layers, as shown in

Fig. 5.7 (a-e). The sixth cluster (Fig. 5.7 (f)) represents the areas, where the LEEM-IV curves are flat. These curves do not allow an exact identification of the number of layers. The average curves of each cluster are plotted in Fig. 5.7 (g) for better comparison.

The heterogeneity of the graphene layers was evident in the BF-LEEM images, but the number of layers could only be determined through LEEM-IV analysis. In this sample, the majority ($\approx 55\%$) consists of two to four layers of graphene. The desired 30° TBLG was observed on only close to 20% of the surface. This distribution of the layers can also be well estimated by looking only at the false color image in Fig. 5.7 (h). It is apparent that the high-T sample is much more heterogeneous than the low-T one.

In summary, the low-T sample shows a homogeneous Gr-R0° layer on top of the ZLG-R30° layer with very small patches of a starting Gr-R30° layer starting from the step edges. In contrast, the high-T sample shows a Gr-R0° layer with Gr-R30° layers of different thicknesses beneath. In general the high-T sample is very inhomogeneous. Note, that the only difference in the preparation of the two samples is the difference in the annealing temperature of 50°C. Therefore, it is crucial to exercise extreme caution when annealing SiC substrates for graphene growth, as the exact annealing temperature significantly affects the resulting graphene layer(s). Further experiments on varying annealing parameters have shown that it is impossible to produce a sample consisting of only one layer of Gr-R0° and one layer of Gr-R30° using proper annealing parameters. In order to obtain high quality epitaxially grown twisted bilayer graphene with a twist angle of 30°, intercalation, for example with hydrogen, of the low-T sample is a promising way to achieve this [31, 55, 132, 156, 157].

6 Exfoliated Twisted Bilayer Graphene

The sample preparation and the acquisition and analysis of the STM and STS data was done by the author and S. Wenzel in collaboration.

6.1 Introduction and Motivation

Exfoliation and stacking is a popular method in fundamental research for the preparation of individual heterostructures. This is also true for twisted bilayer graphene (TBLG) samples studied by scanning tunneling microscopy (STM). STM is a great tool for measuring local changes in topology, and it also allows you to investigate density of states at the measured position. A lot of work has been done on TBLG with small twist angles, mostly close to the magic angle ($\approx$1.05°), showing that the general idea of studying TBLG in STM is worth the effort. While there are many publications on small twist angles [18, 19, 21, 22, 64–71], STM studies on large twist angles of TBLG are still lacking, especially in the range of 20° to 30°. There has been some work on the epitaxial preparation of 30° twisted TBLG on SiC using borazine as a surfactant as shown in Chapter 5 and by Bocquet et al. [1], but no exfoliated and stacked hetereostructure for STM studies.

For a long time, the community expected that large twist angles would not show any interesting physical phenomena. This belief has been contradicted by some theoretical work in recent years. The first paper claiming interesting physics was published by Pal et al. in 2019. [76] According to them, when the twist angle is 21.78°, the Moiré pattern shows a Kagome lattice and gives rise to two distinct regions, one being locally gapped and the other one locally ungapped. This leads to the localization of the electrons. The

localization of the electrons as well as the local changes in the band gap, indicate the existence of topologically protected states forming a geometrically frustrated network along the boundaries of the gapped and ungapped areas. This network leads to flat bands around the band gap. A second theoretical work was published shortly afterwards by Park et al. [75], who also investigated a twist angle of 21.78° and found a different phenomenon. They propose that topological corner states arise in TBLG. These corner states should have fractional electron charges.

In STM, two of these phenomena are potentially observable. On the one hand, the local change of gapped and ungapped regions can be studied with the high lateral resolution of a low temperature (LT)-STM. Here, potentially also the topologically protected states are observed. On the other hand, scanning tunneling spectroscopy could be used to show the rise of flat bands near the bandgap. Another possibility is to perform doping-dependent experiments on a heterostructure sample.

In this chapter, the goal was to examine a large-twist-angle TBLG sample and to look for both the gapped and ungapped areas as well as check for flat bands.

6.2 Materials and Methods

The method of exfoliation and stacking is applied in this chapter, which can be used to assemble heterostructures. Therefore, the preparation of the sample used in this work is described in detail. Here, a brief summary of the steps required is given, while the desired heterostructure with its various layers is shown in Fig. 6.1. For exfoliation, the Si/SiO_2 wafer needs to be cut and cleaned, the graphite bulk material needs to be thinned, and then the graphene is exfoliated onto the wafer. On these wafers, all the desired flakes are searched for. The selected flakes are then picked up one by one with a polymer stamp to transfer them to a STM-ready Si wafer piece with a gold structure on-top. The final stack will be from top-to-bottom: graphene, graphene, hBN, graphite, Au, Ti, SiO_2, as can be seen in Fig. 6.1. The required steps to achieve this heterostructure will now be discussed in detail. For the exfoliation and stamp production, supporting photographs are shown in Fig. 6.2.

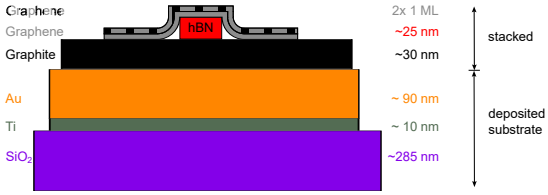

Fig. 6.1: Schematic representation of the stack for STM. This plot is not to scale.

First, the cutting and cleaning of the Si wafer is described [158]. The Si wafer with the top 90 nm oxidized to SiO_2 is cut into small pieces, about 1 cm x 1 cm, using a diamond cutter. The resulting wafer pieces are then cleaned in several steps. First, pressurized nitrogen is used to blow away loose residues from the cutting process. Second, the wafer pieces are cleaned in an ultrasonic bath for 15 minutes using acetone as a solvent. They are then transferred twice into isopropyl alcohol (IPA) to remove acetone residues. Finally, the wafer pieces are placed on a hot plate at 100°C where any remaining solvent is blown off with pressurized nitrogen.

The exfoliation process is discussed here for graphene as an example. The process for hexagonal boron nitride (hBN) is similar [159]. Graphite bulk material is placed on a Scotch tape. It is important to ensure that no part of the graphite protrudes from the tape. These parts should either be pressed onto the tape or removed with tweezers. Then another piece of Scotch tape is placed on top of the piece of Scotch tape holding the graphite flake, and then carefully removed so that pieces of the graphite flake are on both pieces of Scotch tape. This process is repeated several times with all of the available graphite material on the various tapes. The goal is to make certain areas of the graphite so thin that they are partially transparent.

The Scotch tape with the semi-transparent graphite flake is then placed on one of the wafer pieces that are removed from the hot plate at 100°C. The attached Scotch tape is shown in Fig. 6.2 (a), where the small blue areas indicate the very thin areas of the graphite (as indicated by the red arrows). It is then massaged using a semi-flexible piece of plastic, such as the tip of a disposable pipette or a silicone thimble, for 30 s to 1 min, see Fig. 6.2 (b), in order to support the homogeneous transfer of the graphene and

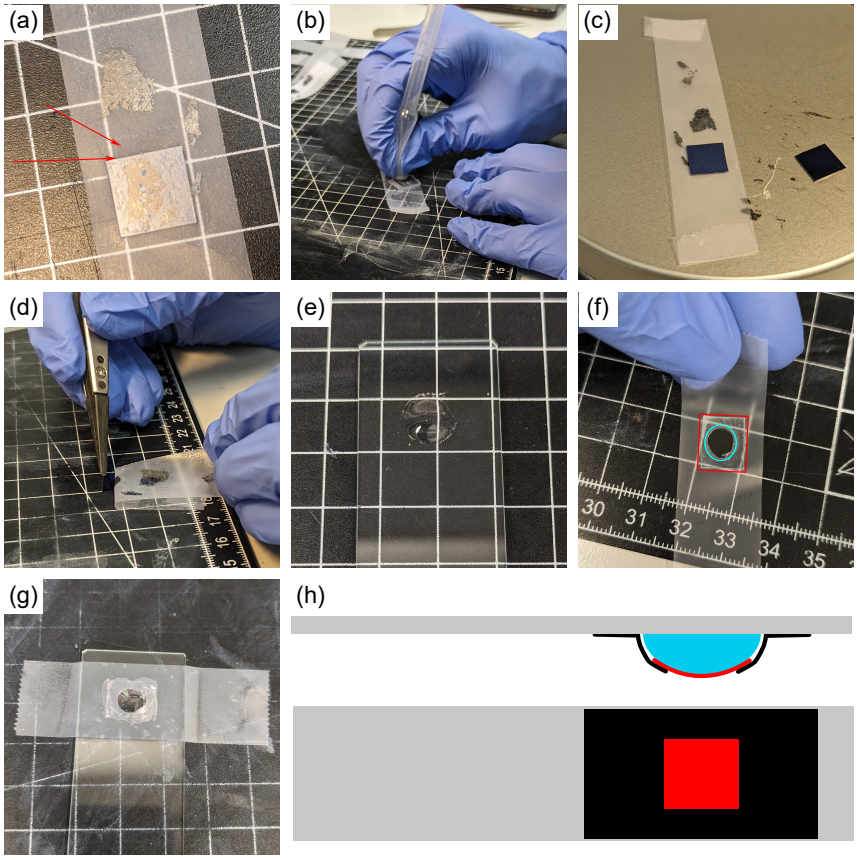

Fig. 6.2: Photographs of the exfoliation and stamp fabrication process. (a) Scotch tape with thin areas of graphene (marked with red arrows) placed on a fresh wafer. (b) Massaging the graphene with the tip of a disposable pipette. (c) Heating the wafer with the Scotch tape on the hot plate for 5 min at 100°C. (d) Peeling off the scotch tape from the wafer. (e) Scotch tape with a hole (cyan circle) after picking up the PC film (red rectangle). (f) PDMS drop on a microscope slide. (g) Combining (e) and (f) to form the stamp, while placing the hole from (e) onto the drop from (f). (h) Schematic drawings of the resulting PC stamp (gray: objective glass, cyan: PDMS drop, red: PC film, black: Scotch tape with hole); the top is a side view and the bottom is a top view.

graphite parts from the Scotch tape to the wafer piece. These wafer pieces with Scotch tape attached are then placed back on the hot plate for 5 min at 100°C, see Fig. 6.2 (c). Finally, the scotch tape is carefully and very slowly removed, keeping a small distance between the wafer and the Scotch tape, as shown in Fig. 6.2 (d). It is useful to employ tweezers for both holding the wafer and removing the tape.

Next, optical microscopy is used to look for thin flakes of the 2D materials on the wafer pieces. The thickness of a flake can be identified by its specific color, especially the green value (RGB) [158, 160, 161]. This green value can be extracted with the microscope software. Several spots on the flake (e.g. G: 112) and on the bare substrate (e.g. G: 121) are checked for this value. If the difference from the substrate to the flake in the green value is about 7-8%, this indicates monolayer graphene, while multiples of this percentage indicate bi- or trilayer graphene (exact values differ for different 2D materials) [158, 161]. From all the identified flakes, the preferred ones for a specific sample are selected and then prepared for transfer using a polymer stamp. To this end, a polymer stamp must be prepared for the transfer and stacking process.

A microscope slide (as used in standard optical microscopy) is used as the basis for the stamp. A drop of polydimethylsiloxane (PDMS) is placed on the slide to give the stamp a certain curvature (compare Fig. 6.2 (e)). This is made of PDMS because of its flexibility and transparency. However, PDMS is not well suited for the pick-up of monolayers of graphene. Therefore polycarbonate (PC) was used as the transfer polymer contacting the flakes. A 6 wt.% solution of PC in chloroform was first spin-coated onto a separate microscope slide for 1 minute at 1500 revolutions per minute (rpm). The PC film was then peeled off the glass slide by attaching a Scotch tape with a hole in the center, as shown in Fig. 6.2 (f). The hole in the Scotch tape with the PC film is then placed over the top of the PDMS drop to cover the top curvature of the PDMS drop, while the Scotch tape covers the rest of the PDMS drop, see Fig. 6.2 (g). The PC stamp, the combination of microscope slide, PDMS drop and PC film, is now ready to be used, i.e. for the transfer of 2D materials [158]. Schematic side and top views are shown in Fig. 6.2 (h) to further clarify on the specific layout of the stamp.

This PC stamp is then mounted into the manual transfer stage (commercial transfer stage

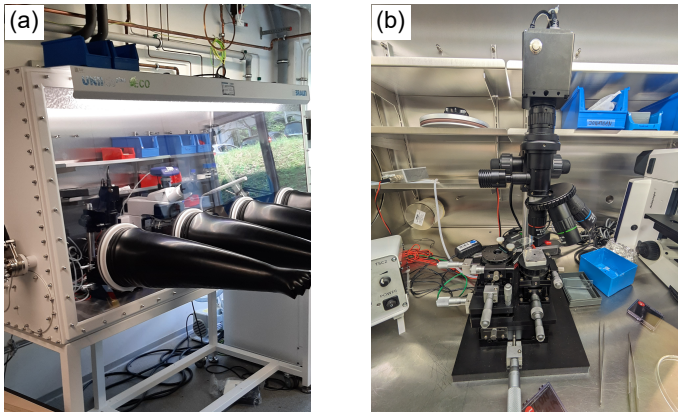

Fig. 6.3: Photos of the glovebox (left) and the transfer stage (right).

from hq graphene), which is located inside of an argon-filled glovebox, both shown in Fig. 6.3. The transfer stage consists of an x,y,z stage for the sample, an x,y stage for the stamp, and a microscope that can be moved in z direction and has three different lenses (5x, 20x, 50x magnification). The temperature of the sample stage is controlled by a commercially available controller. This setup is used to transfer the flakes and assemble the desired heterostructure.

Before assembling the heterostructure, the environment of all desired flakes must be cleaned to avoid picking up additional, unwanted flakes that are created in the environment during the exfoliaton process. This can be accomplished by using a stamp with a polyvinyl chloride (PVC) film on top instead of a PC film. These PVC stamps can pick up flakes and dirt without the need to melt, which is necessary for the PC film. Therefore, the stamp is placed in the vicinity of the desired flake, the wafer is heated to 70°C, then the contact area of the stamp can be moved around on the wafer to pick up or push all flakes in contact away from the desired flake. In this way, all unwanted flakes can be removed. At the end, the PVC film is removed from the stamp and a new PVC film is placed instead to prepare the stamp for later cleaning tasks, Hence, each PVC film is single-use. This type of stamp is not only used for cleaning, but is also often used for stacking heterostructures, as in the newly discovered flip-technique by Jin et al. [46].

However, this technique does not work well with graphene monolayers, because in our experience PVC tends to destroy monolayers and sometimes the pick up and drop down does not work reliably.

For stacking, the flakes must be picked up in the reverse order (top down) of the final stack to be investigated. The stacking order is shown in Fig. 6.1. Stacking starts with the top layer, here a graphene flake. The stacking itself is done with the PC stamp under the optical microscope of the transferstage. The first graphene flake is picked up by slowly touching the wafer next to the desired flake with the PC film on the stamp at 90°C. The sample is then slowly heated up to 130°C until the contact area of the PC film has rolled over the flake due to the thermal expansion of the polymer. Once the entire flake is covered by the contact area of the stamp, the sample is slowly cooled to pick up the flake and carefully lift the stamp from the sample surface.

This procedure is repeated for all the flakes that will form the desired heterostructure, since the entire pick-up and assembly of the heterostructure is done with one stamp. However, care must be taken to align the flakes. The substrate with next graphene flake is rotated with respect to the first graphene flake on the stamp so that two long straight edges of these graphene flakes have the desired twist angle with each other, in this case 30°. These long straight edges are either armchair or zigzag terminated, with the zigzag termination being energetically favorable. [162–164] Therefore, it is assumed that the desired twist angle can be achieved by visually judging the straight edges to obtain the desired twist angle.

In the next step, a smaller but thicker hBN flake is placed under the twisted bilayer region of the graphene flakes. The hBN flake is meant to act as an insulating layer between the twisted bilayer graphene and the surface that needs to be conducting in order to perform STM experiments. The last layer is a large and thick graphite flake, which acts as a flat support for the heterostructure.

The whole heterostructure is then placed on a Si wafer at 200°C, which is coated with 10 nm Ti and then 90 nm Au. Au is used because it interacts weakly with the 2D materials but is conductive, which is crucial for the STM experiments. The thin Ti layer

supports the adhesion of the Au to the wafer. Since these deposited metal layers have a quite high roughness (RMS of about 800 pm), the graphite flake is needed to reduce the vertical strain on the graphene flakes and flatten the heterostructure. To remove the remaining residues of the polymer-assisted transfer, the sample is progressively cleaned in chloroform, acetone, and isopropyl alcohol. To first verify the successful assembly of the heterostructure, the obtained sample is examined by optical microscopy. In Fig. 6.4, a large overview image of the Au pattern (light yellow) on the wafer (substrate is blue) and the position of the deposited heterostructure is shown in panel (a), while a closer view of the heterostructure is shown in panel (b). Here, the individual flakes of the stack are all still visible, as indicated by the arrows and in case of the graphene by an outline. Possible damage to the individual flakes during the transfer could also be observed.

Since the lateral resolution of the optical microscope is limited, the assembled heterostructure is additionally examined by atomic force microscopy (AFM) under ambient conditions to check the quality of the transfer in more detail. The AFM images shown in Fig. 6.5 were measured in contact mode. Panel (a) of Fig. 6.5 displays an overview image of the assembled heterostructure on the Au-coated Si-wafer. The AFM image shows the large graphite flake and the smaller hBN flake (indicated by the red arrow). At this scale, the two deposited graphene monolayers are difficult to observe, but can be identified by looking at the bubbles and edges of the flakes. This becomes clearer in the enlarged image in panel (b) of Fig. 6.5. Here the edges of the graphene flakes are marked by gray arrows at some positions. An important aspect is whether the hBN

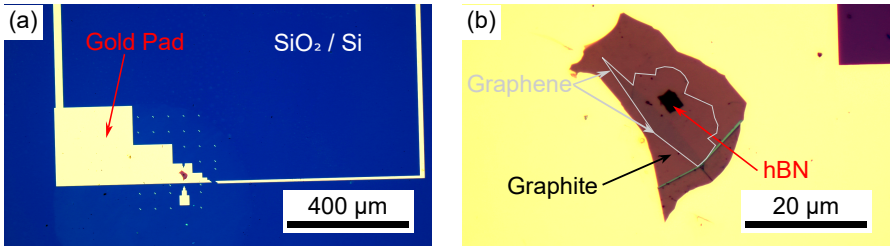

Fig. 6.4: Optical microscopy images of the twisted bilayer graphene on hBN heterostructure placed on the gold pre-pattern. (a) 5x magnification lens used. (b) 100x magnification lens used.

flake is completely covered by the graphene flakes. In addition, it should be ensured that the graphene flakes are still in the correct position and do not show any damage. This could cause the STM tip to come into direct contact with the hBN and potentially cause a crash.

Besides the visible edges of the graphene flakes, contaminations, buckles and bubbles are also observed. These, however, introduce potential interference with the subsequent STM investigations. Therefore, two additional steps were taken to address these issues. First, the assembled heterostructure was annealed in 1.3 bar of a mixture of hydrogen and argon (4% H) at 400°C for 3 hours. This flattens the topmost flakes and removes some of the impurities [165]. To further reduce the remaining contaminations and bubbles due to the polymer-assisted transfer after annealing, the area shown in Fig. 6.5 (b) was scanned several times in contact mode (scan speed: 20 µm/s, setpoint: 3000 mV) with the ambient AFM. Taking advantage of the tip moving over the surface, the dirt particles are pushed to the edges of the image frame. Because the tip exerts pressure on

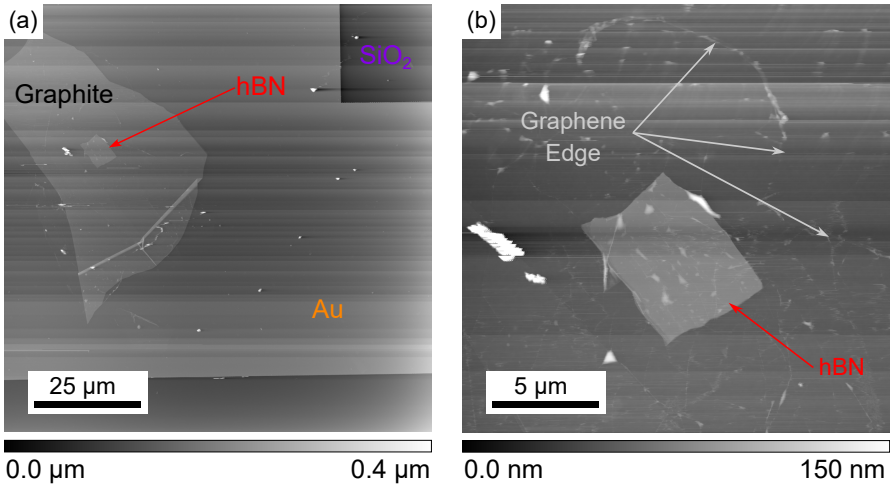

Fig. 6.5: AFM images of twisted bilayer graphene on hBN before annealing in H/Ar atmosphere. (a) 100 µm x 100 µm field of view (scan speed: 60 µm/s, setpoint: 300 mV). (b) 20 µm x 20 µm field of view (scan speed: 12 µm/s, setpoint: 1000 mV).

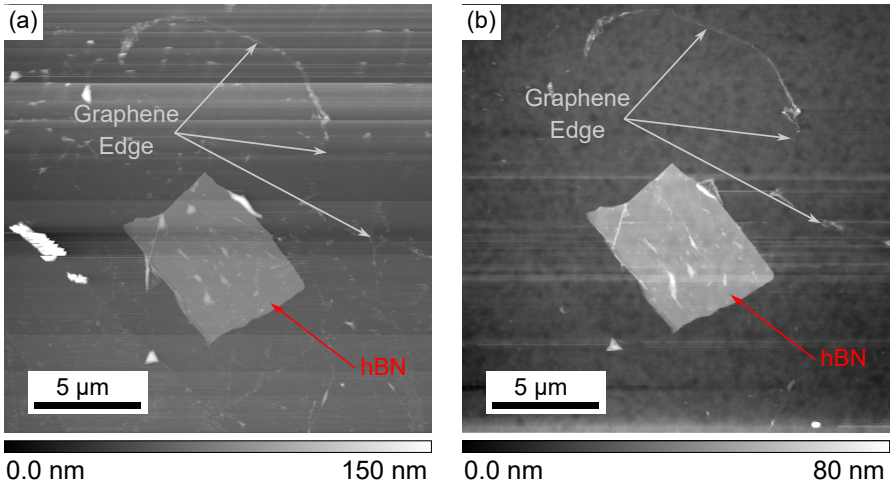

Fig. 6.6: AFM images of the twisted bilayer graphene on hBN (a) before and (b) after annealing in H/Ar atmosphere. 20 µm x 20 µm field of view (scan speed: 12 µm/s, setpoint: 1000 mV).

the surface, the amount of bubbles in the graphene layers can also be reduced. Subsequently, the resulting sample was again examined by AFM under ambient conditions (see Fig. 6.6).

Comparing Fig. 6.6 with Fig. 6.5 (b), a large piece of dirt on the left side has been removed by annealing and AFM sweeping. In addition, the amount of bubbles and buckles has been greatly reduced. Finally, the desired quality of the obtained heterostructure sample is achieved.

The assembled heterostructure needs to be grounded in order to study the sample in the STM, to avoid charging effects and to drain the tunneling current in the STM. This is accomplished by bonding the Au pad on the Si wafer to the sample plate using Ag-epoxy glue. Here, a two-component Ag-epoxy from Epoxy Technology (EPO-TEK H20E-FC) was freshly mixed (ratio 1:1) and then applied to bond the Au pad with the sample plate. The Ag-epoxy was then cured in the glovebox at 100°C for 1 hour. A photograph of the grounded sample mounted on an Omicron sample plate is shown in Fig 6.7 (b).

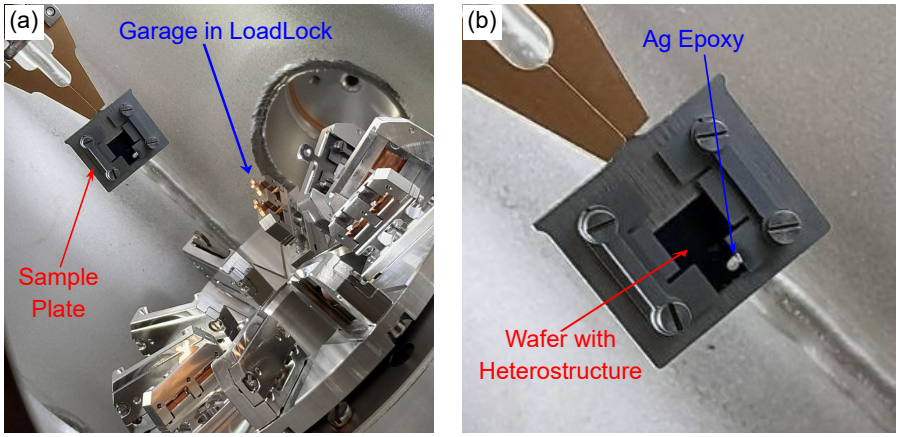

Fig. 6.7: (a) Photograph of the mounted and contacted sample during the transfer to the UHV system. (b) Zoom in on the sample.

Fig. 6.7 (a) shows the loadlock of the used STM chamber during the transfer of the sample into UHV. In the center (blue arrow) the sample garage is visible and at the top left the sample plate including the contacted sample (red arrow) is visible, while it is grabbed by the wobblestick. In Fig. 6.7 (b) the layout of the omicron sample plate is shown, with the Si wafer with the assembled heterostructure on top (marked in red) screwed to the sample plate. The small silver line on the bottom side of the sample (marked in blue) is the Ag-epoxy that connects the Au pad on the wafer to the clamp on the sample plate, thus grounding the heterostructure to the sample plate. The sample itself was transported in air into the UHV system, and then transferred to the preparation chamber and annealed at 230°C - 240°C for 45 minutes to remove any contamination from the air transport. The sample was then transferred to the LT-STM chamber and was ready for STM examination at a temperature of 6K.

6.3 Scanning Tunneling Microscopy

In the following, the STM investigations on the previously described sample are discussed. It is particularly important to note that the process of measuring STM on a het-

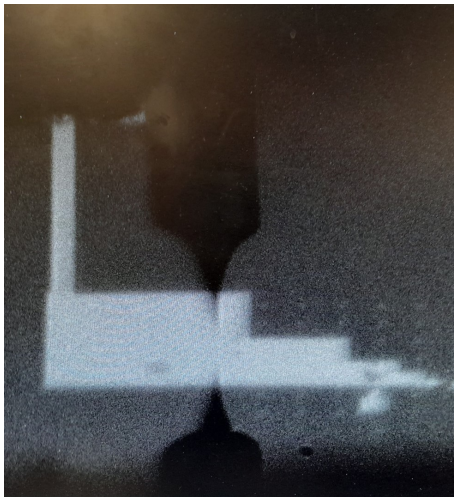

Fig. 6.8: Photograph of the tip being close to the gold pad on the wafer, utilizing the optical access of the used STM.

erostructure differs from that of studying a single crystal (with or without an adsorbate on top) or an epitaxially grown sample due to the size limitation of a heterostructure, increasing the difficulty of the STM investigations. Therefore, the procedure of placing the tip over the heterostructure is discussed before the observations are described in detail. The optical access of the STM machine used is shown in Fig. 6.8. Here the tip is approaching the gold pad, which has the highest contrast in the optical image (almost white). Since the surrounding SiO_2 wafer is insulating, it is important to approach on the gold pad to avoid physical contact between the tip and the wafer or heterostructure. Otherwise, the tip and the heterostructure could be damaged.

Once the tip is safely approached, the routine of navigating to the heterostructure on the gold pad begins. To facilitate this, the gold pad is designed in a stepped shape. This gold edge can be scanned and followed until a corner is reached that shares some x- or y-position with the desired heterostructure (originally planned during transfer and verified by optical microscopy). Once the graphite is hit, large scans are made to clearly identify where exactly the tip is positioned by comparing distinct features in the previous

recorded AFM image and the STM image. Before hitting the hBN edge with the tip, the tip is retracted and moved towards the expected position of the graphene layers. This is performed to avoid scanning the hBN edge itself. Since hBN can cause damage to the graphene on top [23], it may be exposed at the edge of the flake, so the tip could make physical contact and in the worst case destroy the heterostructure, or the tip could pick up insulating particles from the surface. If this happens, the tip must be re-prepared on the gold pad with a certain distance to the heterostructure to avoid damage by pulsing the STM tip, which can lead to loss of position.

On this sample, two different regions were investigated by STM: TBLG on hBN and TBLG on graphite. Both regions are discussed separately, with a focus on TBLG on hBN.

6.3.1 TBLG on hBN

In this section, the region of twisted bilayer graphene on hBN is discussed. Different scales have to be distinguished, especially 6 nm x 6 nm and 40 nm x 40 nm. The first is to look at a very small region and check for the topmost graphene layer. This is shown in Fig. 6.9 panel (a) with a 6 nm x 6 nm field of view. Here the typical hexagonal pattern of graphene can be observed with atomic resolution. To determine if the lattice vectors are in agreement with the literature, line profiles along different crystal directions can be used.

A typical line profile along a crystal direction is shown in Fig. 6.9 (b) as an example. The distance of multiple maxima in this line profile is divided by the number of maxima to reduce the statistical error. This procedure was repeated for different lines, also along other crystal directions. The averaged lattice vector of the three crystal directions is (2.47 $\pm$ 0.01) Å. This value is in excellent agreement with the lattice constant of graphene of 2.46 Å recorded in literature [166]. Besides the average lattice vector, the measured lattice vectors along the three different crystal directions are identical, indicating that there is no appreciable lateral strain on the topmost graphene layer.

In Fig. 6.10 (a) a 40 nm x 40 nm STM image is shown. This larger area can also be

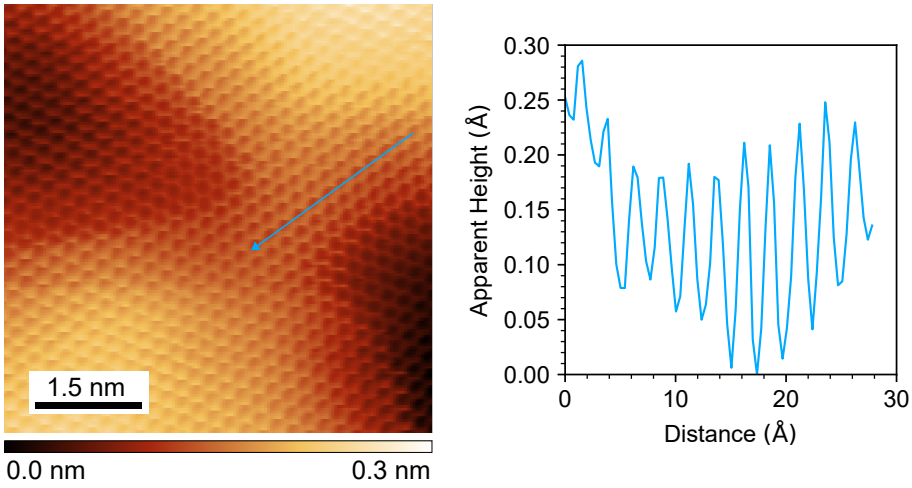

Fig. 6.9: STM image of twisted bilayer graphene on hBN. 6 nm x 6nm field of view (+100 mV, 50 pA), and line profile along the blue arrow in the STM image.

used to independently determine the lattice vector. If a Fast Fourier Transform (FFT) of the STM image is calculated, the length of the graphene lattice can be determined by measuring the distance of the graphene spots to the center of the FFT in reciprocal space (b). This distance is then converted back to a real space distance (a)

$$a = \frac{1}{b \sin\left(\frac{2\pi}{6}\right)} \,. \tag{6.1}$$

This calculation yields a value for the graphene lattice of 2.46 $\pm$ 0.6 pm, which is in agreement with the result of line profile analysis. The results for the two different methods are additionally shown in Table 6.1.

Regarding Fig. 6.10 (a), the atomic resolution is not the only interesting feature. At a larger scale, a hexagonal pattern with a higher apparent height can be observed in the STM image. This pattern is attributed to the moiré of the top two layers, both graphene layers. This moiré is induced by the twist angle between the two graphene layers. The length of the moiré is characteristic for a certain twist angle. Therefore, the twist angle

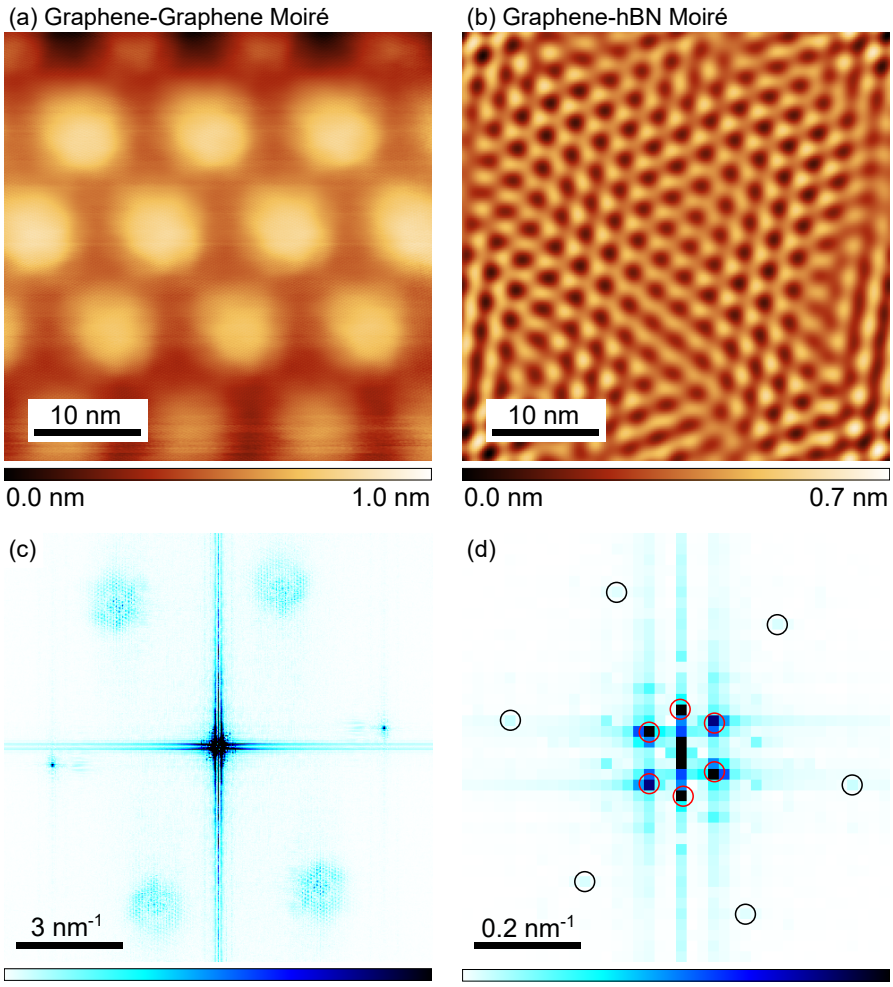

Fig. 6.10: (a) STM image of twisted bilayer graphene on hBN. 40 nm x 40nm field of view (+200 mV, 100 pA), (b) STM image from (a) with FFT filtered image overlaid, (c) FFT of the STM image in (a), (d) zoom in to the center of (c).

Table 6.1: Measured lattice constants for graphene.

method	lattice constant (pm)
line profile	2.47 ± 0.01
FFT	2.46 ± 0.06

θ of the twisted bilayer graphene on hBN can be determined using the expression [167, 168]

$$\lambda = \frac{(1+\delta)a}{\sqrt{2(1+\delta)(1-\cos(\theta)) + \delta^2}} , \tag{6.2}$$

where λ is the measured wavelength of the moiré pattern, δ is the lattice mismatch between the two layers, a is the lattice vector, and θ is the twist angle between the two layers. Rearranging yields

$$\theta = \frac{(\delta+1)^2(\lambda^2 - a^2)}{2\lambda^2(\delta+1)} . \tag{6.3}$$

In the case of twisted bilayer graphene, the lattice mismatch δ of both graphene layers is zero. Therefore, the expression simplifies

$$\theta = \frac{\lambda^2 - a^2}{2\lambda^2} . \tag{6.4}$$

The moiré length λ can be determined in two different ways, similar to the lattice constant: First, the distance from one moiré maximum to the next can be measured using the real-space image. Second, the distance can be determined from the FFT in reciprocal space. The reciprocal pattern of the moiré of both graphene layers is shown in Fig. 6.10 (c) by the inner hexagonal spots marked by red circles. The moiré length was investigated in several images, both in real space and in the FFT, with partly larger field of views and determined to be (11.6 ± 0.7) nm, which corresponds to a twist angle of

Table 6.2: Measured lattice constants for the moirés of graphene-graphene and graphene-hBN.

moiré	method	moiré length (nm)
graphene-graphene	real space	11.56 ± 0.07
graphene-graphene	FFT	11.64 ± 0.07
graphene-graphene	averaged	11.61 ± 0.07
graphene-hBN	FFT	2.92 ± 0.01

1.2° between the two graphene layers. This determined twist angle is far from the desired one, the reason and possible solutions will be discussed later.

A more thorough examination of Fig. 6.10 (c) reveals that the hexagonal pattern exhibited by the graphene-graphene-moire is slightly distorted. Two potential explanations are posited. The initial observation is that the hexagon appears to be distorted solely due to the low resolution of the FFT, which is constrained by the scan range of the STM image. This phenomenon becomes evident upon examining the dimensions of each measurement pixel in the FFT. An alternative hypothesis is that the lower graphene layer is distorted, as only the top graphene layer was observed in Fig. 6.9. This phenomenon would also result in a distortion of the hexagon.

Also the additional hexagonal moiré, marked by black circles in Fig. 6.10 (d), shows a distortion. This moiré pattern is due to the twist angle between the lower graphene layer and the underlying hBN layer. Here a moire length of (2.923 ± 0.004) nm is determined, resulting in a twist angle of 4.7°. This moiré is barely visible in the original real space STM image. To make it visible, a filtering technique for STM images can be applied: 2D-FFT (Fast Fourier Transform) filtering. Here, only the intensity of certain regions in the FFT is plotted in real space. In Fig. 6.10 (b), the STM image in Fig. 6.10 (a) has been overlapped with the FFT filtered image, selecting only the moiré pattern belonging to the graphene and hBN interaction. Looking at this overlapped image, it can be seen that the minima and maxima of the graphene-hBN moiré are not distributed identically on the maxima of the graphene-graphene moiré. Hence the graphene-graphene moiré

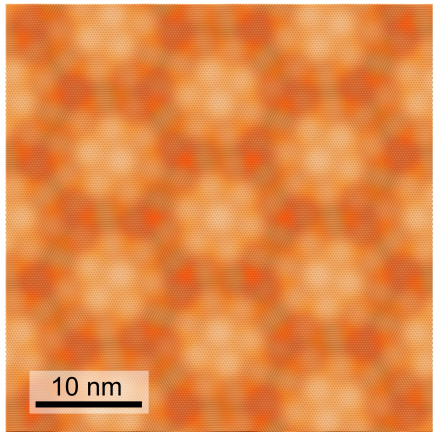

Fig. 6.11: Moire simulation of TBLG on hBN with twist angles 1.2° between the two graphene layers and 4.7° between the lower graphene and the hBN layer. The strength of the hBN pattern is attenuated by a factor of 0.3.

and the graphene-hBN moiré are incommensurate with each other. The assignment of the two different moiré patterns to the specific layers is based on their relative intensities. This is due to the fact that the STM intensity is strongly dependent on the height. Therefore, the more intense moiré is attributed to the interaction of the top two layers (the graphene-graphene moiré).

A more detailed understanding of the combination of the two moiré patterns can be obtained by performing a simulation. Here the atoms of all three layers (graphene, graphene, hBN) are plotted with their respective lattice constants and determined twist angles. For graphene a lattice constant of 2.460 Å was used, for hBN 2.502 Å. The twist angles are 1.2° and 4.7° for the graphene-graphene interface and the graphene-hBN interface, respectively. The resulting image is shown in Fig. 6.11.

The hBN layer intensity has been attenuated by a factor of 0.3 to reflect the intensity ratio of the dominant graphene-graphene moiré to the graphene-hBN moiré, but still keeping the intensity of the graphene-hBN moiré higher to visualize it more strongly than in the experimental image. When comparing the simulated moiré pattern with the

measured one, the incommensurability of the two moiré patterns in the measured pattern is not observed in the simulated one because on all the graphene-graphene moiré maxima, the minima and maxima of the graphene-hBN-moiré are similar. This effect can be explained by the existence of a super-moiré in the experimental data due to the overlap of the two moiré patterns [169]. This super-moiré is of much lower intensity and has a larger moiré length. In the simulation this effect is not included due to the very simple model of generating the moiré patterns. In addition, the simulation only reflects the topography in a simple way, but does not consider any electronic effects.

In addition to the STM images, scanning tunneling spectroscopy (STS) data were recorded. The data are discussed in terms of potential explanations for the observed peaks and features. To gain a more detailed understanding of the underlying physics and explicitly assign the observed peaks to specific physical phenomena, collaboration with a theoretical physicist would be necessary. However, this was beyond the scope of this thesis. The potential existence of superconductivity could not be explored due to the limitations of the available STM system, which had a base temperature of about 6 K. The critical temperature observed for magic-angle TBLG superconductivity is 1.7 K [16].

First, a large energy range from -500 mV to +500 mV is shown in Fig. 6.12. Two sets of features are observed, one at approximately ± 200 mV and the other at approximately 0 mV. Both are marked with arrows in Fig. 6.12. These peaks are caused by van Hove singularities due to the overlapping of the bands of the two graphene layers with a small twist angle. These van-Hove singularities emerges when the misaligned Dirac cones from each graphene layer ”cross” or hybridize, thereby creating saddle points in the electronic band structure where the density of states experiences a pronounced increase. The more dominant feature around 0 mV is caused by the van Hove singularities near the Fermi level, where the two Dirac cones cut each other, causing a van Hove singularity. A similar effect occurs at a position about ± 200 mV away from the Fermi level, resulting in so-called remote peaks [169]. These van Hove singularities shift in their energetic position with changing twist angles because the Dirac cones of the two graphene layers have different distances in K-space [74]. This behavior has been observed by Xie et al. for a twist angle of 1.01° [170]. The energetic position of the van Hove singularity is another indication that the high intensity moiré comes from the two graphene

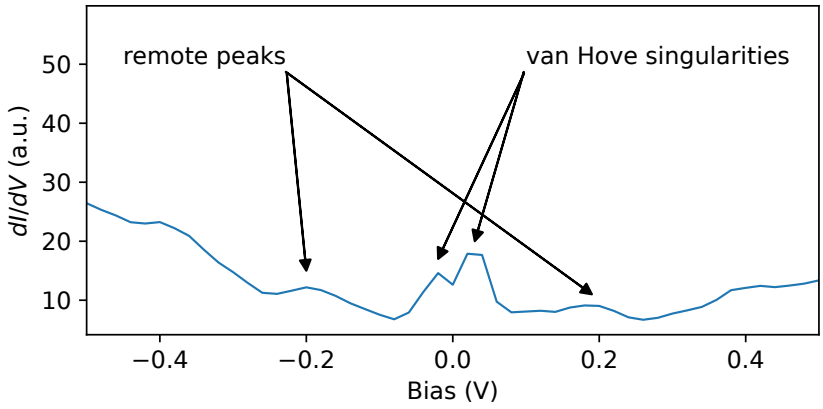

Fig. 6.12: Scanning tunneling spectrum of TBLG on hBN in the range from -500 mV to +500 mV. (Original spectrum was -1 V to +1 V, setpoint: 100 pA, lock-in modulation: 20 mV, temperature: 6.2 K.)

layers, because assuming the twist angle of the graphene-hBN moiré for the graphene-graphene moirŕe, the van-Hove singularities would be expected at a higher energy of approximately -500 meV and +500 meV [74].

In the large range STS spectrum in Fig. 6.12, the van Hove singularities around 0 mV appear to consist of two peaks, one below and one above the Fermi level. It is important to note that the interpretation of the number of peaks from this large range scan is not straightforward due to the low energy resolution. Hence, a closer look at the energy regime around the Fermi level is needed. Therefore, a series of STS investigations was performed in the range from -100 mV to +100 mV while changing the setpoint of the measurement. This was done for two spots at the maximum of the graphene-graphene moiré. The STS series of the first spot is shown in Fig. 6.13. In addition to the STS series itself, the various dI/dV spectra were fitted using only Gaussian peaks, as done by Li et al. for a twist angle of $\sim 1.2°$ [171]. Additionally, the raw data of this STS series is shown in Fig. 6.14 for comparison.

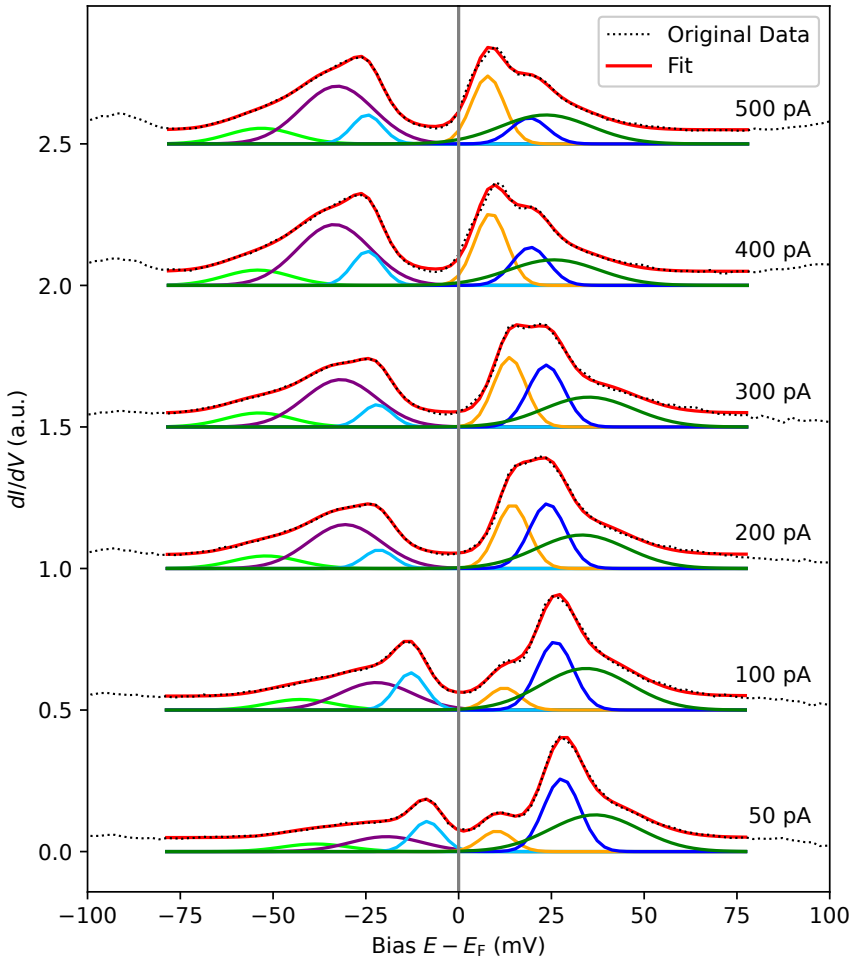

Fig. 6.13: Scanning tunneling spectra of TBLG on hBN. The scan range is from -100 mV to 100 mV. The original data and the fit are shown with a quadractic background subtracted.

The dI/dV spectrum, recorded with a setpoint of 50 pA, exhibits three distinct peaks and two broad shoulders. The three peaks are at -7.86 mV (cyan), 10.97 mV (yellow), and

28.47 mV (blue), while the shoulders appear to be further away from the Fermi level. The Fermi level can be determined as the minimum between the two sets of peaks. For a setpoint of 50 mA, the Fermi level is located at approximately 1-2 mV. 0 mV is indicated by the gray vertical line in Fig. 6.13. The three peaks in the spectrum correspond to the van Hove singularities. These observations were also made for the larger range scan depicted in Fig. 6.12, however, due to the low energy resolution of the instrument, these peaks could only be discerned as two distinct peaks. The enhanced energy resolution for the reduced scan range in Fig. 6.13 indicates the presence of at least three distinct peaks. Xie et al. demonstrated that van Hove singularities are divided into two peaks each when they are at the Fermi level [170, 171]. This phenomenon is also evident in this case, where the positive bias side exhibits two distinct peaks, attributed to the splitting at Fermi. This splitting is attributed to electron-electron correlation, as evidenced by recent studies [170, 172].

This phenomenon is not exclusive to the positive bias side; it is also observed for the negative bias side as the setpoint is elevated. As previously stated, modifying the setpoint results in a corresponding alteration of the distance between the tip and the sample. It can be deduced that an increase in the setpoint will result in a decrease in the distance between the tip and the surface. In a rudimentary model of a plate capacitor (E = U/d), the effective electric field from the tip to the surface is inversely proportional to the distance. Consequently, local doping of the heterostructure is observed as the setpoint is varied. This doping exerts a significant influence on the energetic position of van Hove singularities. Xie et al. [170] demonstrated that external doping can effectively shift the van Hove singularities from below the Fermi level to above the Fermi level. This phenomenon was observed through the observation of the splitting of the singularities. In this case, the doping strength is considerably weaker because no external doping was applied; only the changing effective electric field of the tip on the sample was used. The effect of this phenomenon can be observed by examining the transition from a low to a high setpoint, as illustrated in Fig. 6.13.

At a higher setpoint, i.e., 300 pA, there has been an alteration in both the intensity and position of the peaks in comparison to the spectrum at 50 pA. In addition to the shifts, a fourth peak (colored purple) is clearly more pronounced on the negative bias side.

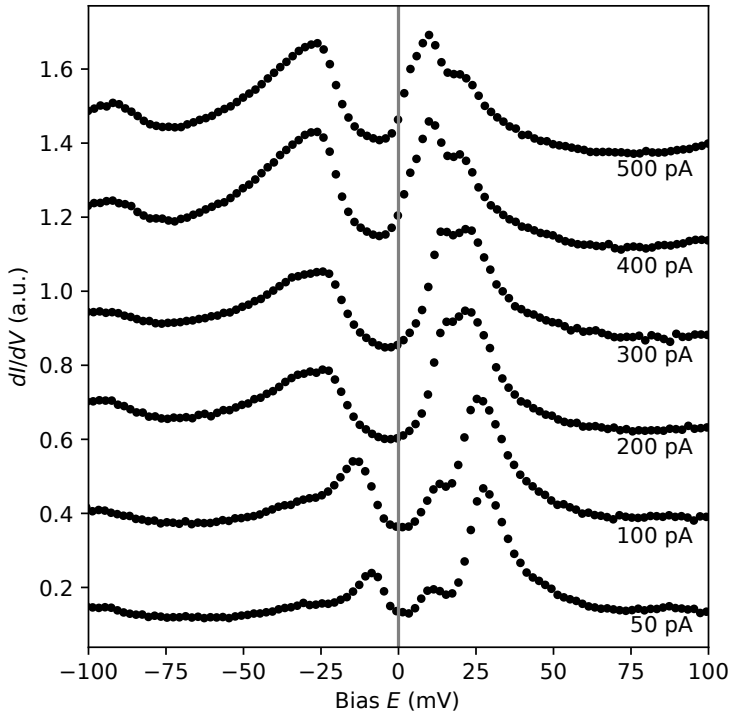

Fig. 6.14: Raw data of the scanning tunneling spectra of TBLG on hBN. The scan range is from -100 mV to 100 mV.

The observed phenomenon can be attributed to the splitting of the van Hove singularity, which also occurs on the negative bias side. This splitting is a consequence of increased doping, resulting in a different position relative to the Fermi level. The Fermi level undergoes a shift from a slightly positive value to a significantly negative value, indicative of the occurrence of doping. For this setpoint (300 pA), the peaks have their maximum at -31.39 mV (purple), -21.57 mV (cyan), 14.14 mV (yellow), and 23.99 mV (blue). Consequently, a total of four peaks are observed for the splitting of the van Hove singularities, while the two broad shoulders are also fitted using a Gaussian peak type. The presence of these two broad peaks is attributed to the presence of a lower-lying band,

Table 6.3: Fit parameters for the STS series shown in Fig. 6.13 for the different peaks.

color	peak shape	FWHM (50)	FWHM (500)	FWHM (avg.)
light green	Gaussian	18.71	23.60	21.16
purple	Gaussian	23.55	22.57	23.06
cyan	Gaussian	9.33	10.01	9.67
yellow	Gaussian	8.29	12.28	10.28
blue	Gaussian	11.90	11.25	11.52
dark green	Gaussian	25.90	31.20	28.55

which is responsible for the observed broad background.

The determination of peak positions and amplitudes, as determined by the fitting of the data, is illustrated in Fig. 6.15. For these fits, the full width at half maximum (FWHM) was fixed to the average of the 50 pA and 500 pA setpoint fits, as listed in Table 6.3. This was due to the fact that the peak shapes underwent significant changes at these extreme setpoints. The colors in Fig. 6.15 correspond to the fits in Fig. 6.13.

The present analysis primarily focuses on the two peaks on the positive bias side, where the trend is most pronounced. The peaks on the negative bias side are less visible in the raw data (Fig. 6.14), and their trend is more sensitive to the fitting parameters. As demonstrated in Fig. 6.15 (a) the majority of peaks exhibit a shift towards lower energy levels as the setpoint rises. A notable exception to this trend is the yellow peak, which initially increases in energy before reaching the 200 pA setpoint and aligning with the predominant trend.

This comprehensive behavior can be attributed to tip-induced doping, wherein the STM tip functions as a local gate. The varying setpoint has been demonstrated to alter the induced electric field, thereby modifying the local electron concentration. The aforementioned doping not only shifts the Fermi level but also renormalizes the electronic band structure, thereby causing the van Hove singularities to shift in energy [170]. The anomalous behavior of the yellow peak and the significant change in its amplitude between the 100 pA and 200 pA setpoints (Fig. 6.15 (b)) may indicate a change in the

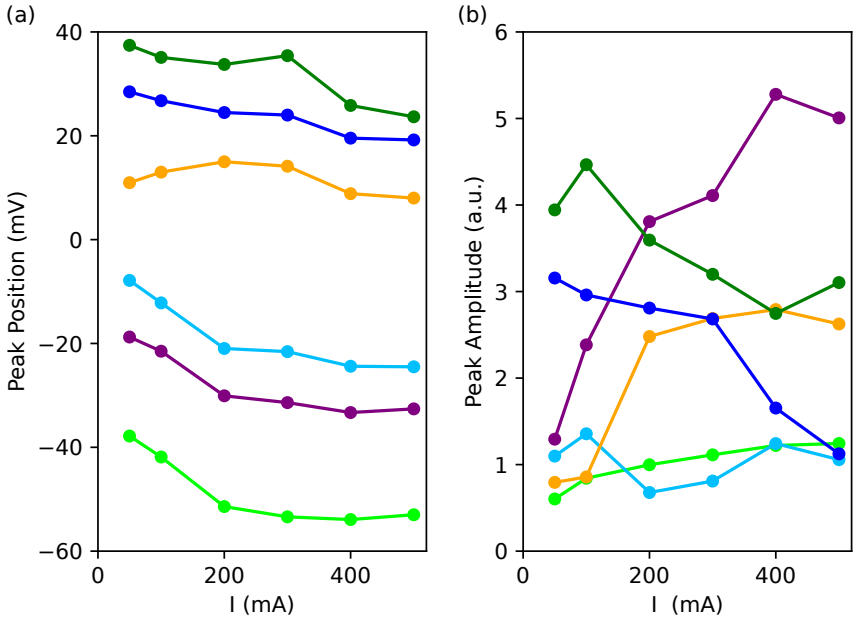

Fig. 6.15: (a) Peak positions of the fit against tunneling current. The colors used correspond the colors of the fits shown in Fig. 6.13. (b) Same as (a) but showing peak amplitudes instead of positions.

splitting of the van Hove singularities. This amplitude change is also evident in the raw data, thereby confirming that it is not a fitting artifact.

The trends for the peak amplitudes are less clear, and the exact values depend more on the fitting routine. The most significant observation is the anti-proportional behavior exhibited by the yellow and dark blue peaks, which show that the dark blue peak's amplitude decreases with increasing setpoint, while the yellow peak's amplitude increases. This opposing trend suggests the presence of significant electron-electron correlation at the van Hove singularities in proximity to the Fermi energy [19, 171, 172]. This correlation serves as the underlying driving force for phenomena such as the unconventional

superconductivity observed in TBLG, as evidenced by studies conducted by Jiang et al. [19], Inbar et al. [172], and Cao et al. [16, 134].

Another noteworthy trend is the increasing amplitude of the purple peak, which persists alongside a constant light blue peak. This phenomenon can be attributed to the shift of a lower-energy van Hove singularity into the Fermi level, resulting in enhanced splitting due to correlation effects. However, this observation could also be a fitting artifact, as these peaks are less distinct in the raw data compared to those at higher energies. The anti-parallel behavior of the lower-band peaks provides further indication for the existence of the tip-induced doping effect.

Subsequent re-examination of the same position within the graphene-graphene moiré at a different location on the sample yielded divergent results. The data were recorded using a more extensive setpoint steps (20, 50, 100, 150, 200, 250, 300, 350, 400, 450, and 500 pA). In order to ensure clarity and comparability with previous measurements (Fig. 6.13), only the spectra and corresponding fits for the same setpoints are shown in Fig. 6.16 (a). However, all data points are included in the plots for peak position and amplitude (Fig. 6.16 (b) and (c)). Furthermore, the raw data concerning all setpoints is displayed in Fig. 6.17 and the FWHM are listed in Table 6.4.

Two key phenomena are immediately apparent. First, the higher-energy side shows four peaks instead of the previous three. Secondly, the shift of the peaks is considerably less pronounced, suggesting a reduced doping effect of the tip. An examination of the spectrum, with a 50 pA setpoint, reveals the presence of three peaks on the negative bias side. These peaks correspond to the splitting of the van Hove singularity at -24.18 mV (purple) and -14.67 mV (cyan), as well as the broader, lower-lying band at -41.00 mV (light green), which forms the background. These peak positions bear a resemblance to those observed in the 100 pA measurement at the preceding location, suggesting a modification in the doping process.

A notable distinction emerges in the positive bias domain, where an additional peak necessitates the adjustment of the raw data to incorporate four peaks. Two of these peaks are attributed to the splitting of the van Hove singularity, and one is assigned to the

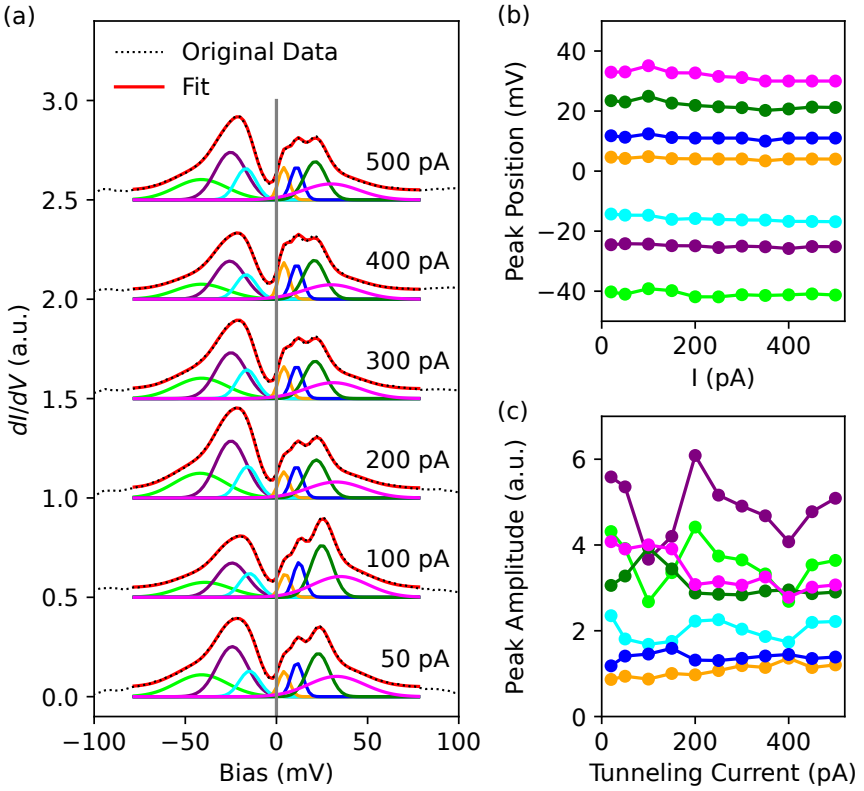

Fig. 6.16: (a) STS of TBLG on hBN at a second spot. The scan range is from -100 mV to 100 mV. The original data and the fit are shown without background subtraction, but for the fit a quadractic background was subtracted. (b) Peak positions of the fit aginst tunneling current. The colors used correspond to the colors of the fits in (a). (c) Same as (b) but showing peak amplitudes instead of positions.

lower-lying broad band. Given the absence of assignment to a fourth peak, a definitive linkage between the two van Hove singularity peaks and specific positions remains unattainable.

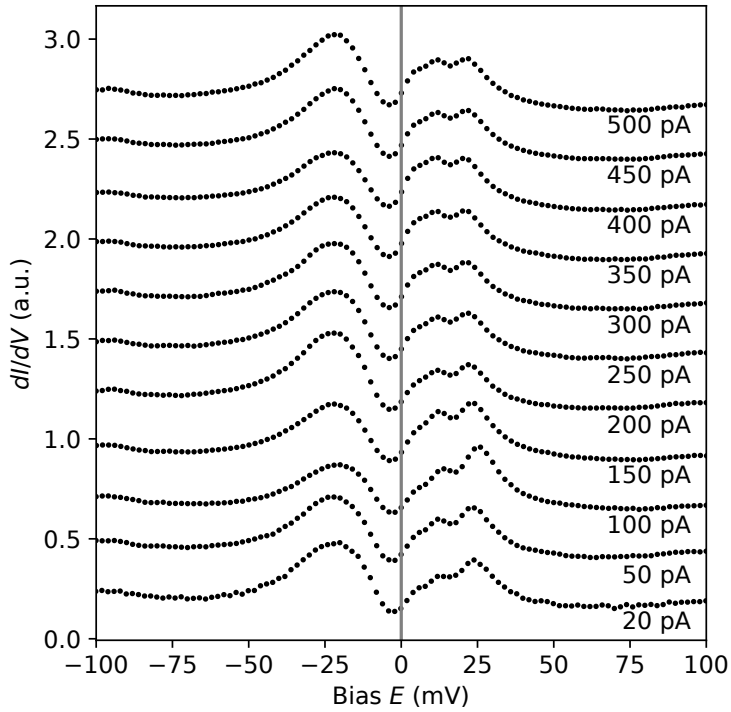

Fig. 6.17: Raw data of the scanning tunneling spectra of TBLG on hBN on the second spot. The scan range is from -100 mV to 100 mV.

In order to gain more insight into the fourth peak, it is necessary to consider the underlying hBN substrate. As previously mentioned, the hBN forms an additional moiré pattern with the lower graphene layer. This pattern is incommensurate with the graphene-graphene moiré, creating a super-moiré with a wavelength that exceeds the detection limit of the STM.

As demonstrated by Wong et al. [169], this phenomenon has been observed to occur for graphene-graphene and graphene-hBN twist angles of 0.93° and 1.65°, respectively. Their research has demonstrated that the underlying hBN disrupts the layer degeneracy

Table 6.4: Fit parameters for the STS series shown in Fig. 6.16 for the different peaks.

color	peak shape	FWHM (50)	FWHM (500)	FWHM (avg.)
light green	Gaussian	32.73	34.08	33.40
purple	Gaussian	18.98	20.93	19.95
cyan	Gaussian	11.21	15.19	13.20
yellow	Gaussian	6.08	7.81	6.94
blue	Gaussian	8.36	7.22	7.79
dark green	Gaussian	14.13	14.13	14.13
red	Gaussian	35.41	36.51	35.96

inherent in graphene, thereby inducing a splitting of the bands. Theoretical studies have predicted a strong influence of hBN on the band structure near the Fermi level, with a significant dependence on the graphene-hBN twist angle [173]. Therefore, a plausible conclusion is that the different effects observed at this position are caused by the super-moiré resulting from the underlying hBN.

As with the initial location, the peak positions and amplitudes are plotted against the setpoint in Fig. 6.16 (b) and (c). For the peak positions, a slight shift towards lower energies is observed as the setpoint increases. This trend aligns with the observations from the previous location; however, the shift in the current study is less pronounced, suggesting a less significant doping effect.

A lack of discernible trends is evident in the amplitude of the main peaks. The fitting artifact, observable at a 100 pA setpoint, could not be resolved without a substantial modification to the fitting method. This modification would have rendered the results incomparable to the initial location.

6.3.2 TBLG on Graphite

In addition to the TBLG region on hBN, a TBLG region on graphite was also found on the heterostructure. In Fig. 6.18 the STM shows a moiré with a moiré length of 8.5 $\pm$ 0.3 nm. This moiré length corresponds to a twist angle of 1.7°. This twist angle differs by 0.5° from the one observed for the TBLG on hBN.

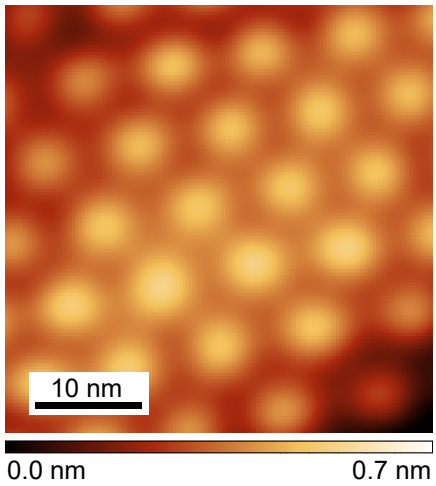

Fig. 6.18: STM image of twisted bilayer graphene on graphite. 40 nm x 40 nm field of view (+200 mV, 100 pA).

This difference in the twist angle is unexpected. For the same stacked graphene layers, the twist angle should remain the same throughout the sample. This change in twist angle could be due to the relatively high hBN flake (several nm), which therefore exerts some strain on the overlying graphene flakes at the edges of the hBN flake. These edges are the boundaries between the two observed moiré patterns and so the twist angle between the two graphene flakes is altered by the hBN flake edges. In contrast to the TBLG region on hBN, no second moiré due to the twisting of the graphite flake to the graphene layers is observed.

A setpoint-dependent series of dI/dV spectra was recorded and analyzed for the TBLG

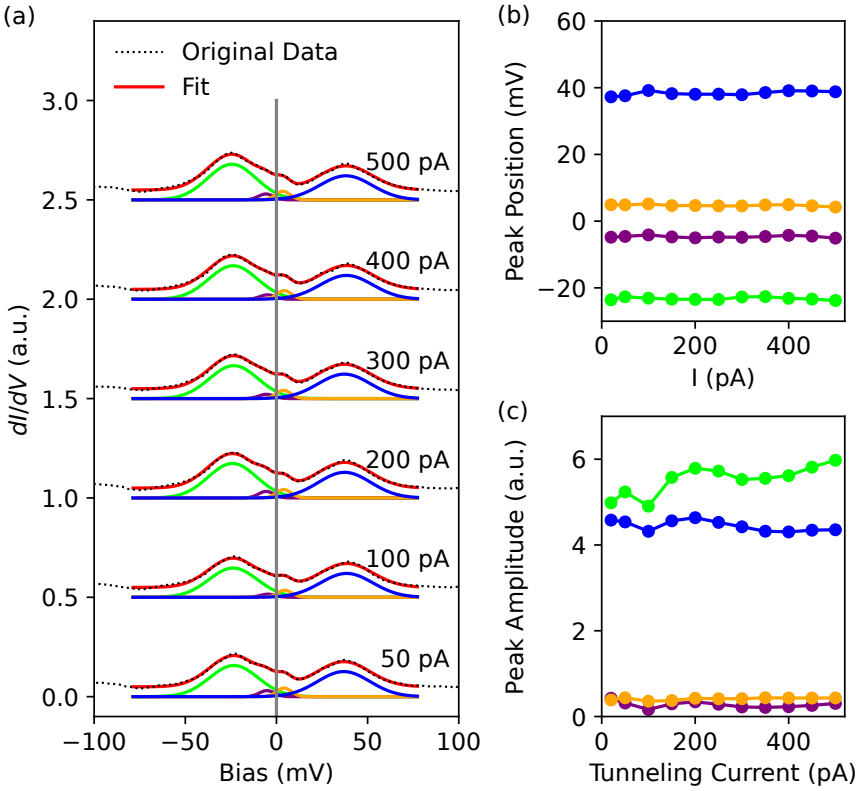

Fig. 6.19: (a) STS of TBLG on graphite. The scan range is from -100 mV to 100 mV. The original data and the fit are shown without background subtraction, but for the fit a quadractic background was subtracted. (b) Peak positions of the fit versus the tunneling current. The colors used correspond to the colors of the fits in (a). (b) Same as (a), but showing the peak amplitudes instead of positions.

region on a graphite substrate, similar to the procedure used for the hBN substrate. The data, fits, peak positions, and amplitudes are displayed in Fig. 6.19, with peak shapes and FWHM detailed in Table 6.5.

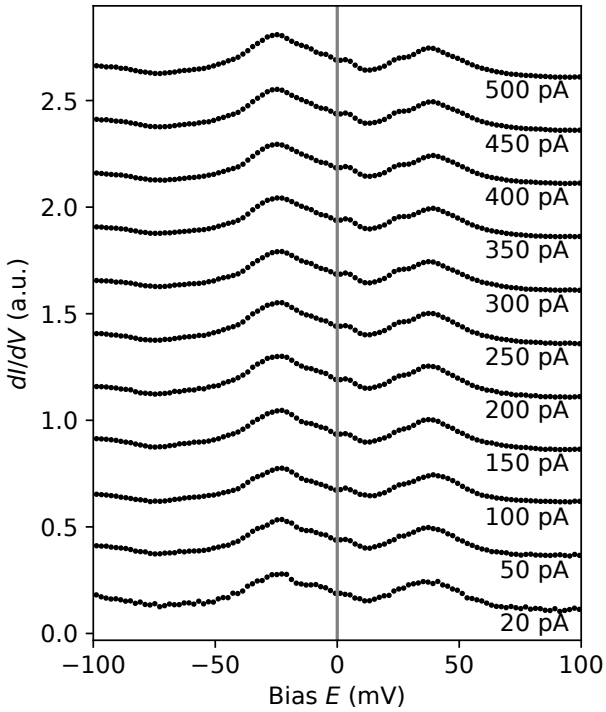

Fig. 6.20: Raw data of the scanning tunneling spectra of TBLG on graphite. The scan range is from -100 mV to 100 mV.

The spectra remain constant despite changes in the setpoint, as evidenced by the stable peak positions and amplitudes in Fig. 6.19 (b) and (c). The data is modeled using four Gaussian peaks. Two prominent peaks are located at approximately -23 mV and 34 mV, while two smaller peaks are found closer to the Fermi level at -5 mV and 5 mV. The four peaks in the spectra correspond to van Hove singularities, which are caused by the twisted graphene sheets and are additionally split at the Fermi level.

It is noteworthy that these van Hove singularities remain static on the graphite substrate, thereby indicating the absence of tip-induced doping. This phenomenon can be

Table 6.5: Fit parameters for the STS series shown in Fig. 6.19 for the different peaks.

color	peak shape	FWHM (50)	FWHM (500)	FWHM (avg.)
green	Gaussian	30.64	31.90	31.27
purple	Gaussian	8.04	11.12	9.58
yellow	Gaussian	11.77	6.69	9.23
blue	Gaussian	34.67	32.82	33.75

attributed to the electrical conductivity of graphite, which effectively shields the TBLG from the local potential changes induced by the STM tip. This behavior stands in contrast to the earlier findings concerning the insulating hBN substrate. In this case, a discernible trend with the shifting setpoint was identified, thereby reinforcing the assertion that the tip-induced doping shifted the observed peaks of the van Hove singularity.

The broad background on the sides away from Fermi is also not visible, indicating that the substrate (hBN or graphite) has a significant effect not only on the bands close to Fermi, but also on the lower lying bands.

The selection of substrate material was found to be a pivotal factor in determining the electronic properties of twisted bilayer graphene (TBLG), with discernible effects observed for both hBN and graphite. The insulating nature of hBN permitted tip-induced doping, thereby providing a valuable mechanism for exploring how van Hove singularities and band structure shift in response to local changes in charge carrier density. Additionally, the difference in the lattice constant of TBLG and hBN is likely the cause of the super-moiré pattern, which has been identified as a contributing factor to the observed splitting of the van Hove singularities. Conversely, the conductive graphite substrate functioned as an effective ground plane, thereby shielding the TBLG from the influence of the STM tip. This approach effectively mitigated the occurrence of tip-induced doping, thereby ensuring the reliability of measurements taken at a constant charge neutrality point. The absence of a broad background signal on the graphite substrate further indicated that its influence extends beyond the bands near the Fermi level to lower-lying bands. These findings underscore the notion that hBN serves as the more suitable substrate for investigating doping effects and moiré-induced band modifica-

tions, while graphite is better suited for stable, intrinsic band structure measurements with only delocalized modifications.

6.4 Summary and Outlook

A TBLG sample was prepared by exfoliation and stacking and then investigated by STM. In contrast to the desired large twist angle, the resulting twist angle was close to the magic angle, with a value of 1.2°. The different physics observed in this work, including the van Hove singularities as well as the doping effect of the tip, have already been observed in the literature [19, 74, 170, 171]. The different authors have shown these effects separately of each other, while in this work the combination of the phenomena is observed and presented. In contrast to the literature, the fitting routine of the van Hove singularities near the Fermi level was more sophisticated than the fit shown by Li et al. [171].

This work will be used in the future as an useful comparison to the originally planned samples with a large twist angle of 20° to 30°. These future samples will focus on large twist angles, as already planned for this work. The most likely reason for preparing a small twist angle instead of the desired large one could be the by-eye judgement of the long straight edges of the graphene flakes used. To reduce the potential problem of confusing zigzag and armchair edges, and thus the chance of getting a twist angle that differs by 30°, the graphene flakes must be chosen differently. The safest way is not to use two different flakes, but to use one large flake and cut it into two pieces. Then they can be picked up one after the other with a precise control of the angle. Since it is experimentally quite challenging to find graphene flakes large enough and to cut them without causing other damage to them, there is also the possibility of using flakes that are very close together on the wafer used for exfoliation. The idea here is that both flakes come from the same piece of graphite and therefore have the same orientation on the wafer. Thus, the two graphene flakes would be picked up one after the other, while the wafer piece in between would be rotated by the desired twist angle, similar to the cut flakes.

7 TBLG Preparation for (S)TEM by Exfolation

The sample preparation was done by the author and S. Wenzel in collaboration. First TEM tests were performed by O. Maßmeyer.

7.1 Introduction and Motivation

This chapter describes the preparation of TBLG samples for the investigation in transmission electron microscopy (TEM) in the group of K. Volz at the University of Marburg. The TEM investigations were carried out by O. Massmeyer in Marburg. The TEM technique has been extended by a new mode of operation, the scanning (S)TEM. STEM is able to achieve a higher resolution due to the different measuring mode. Here, the electron beam is focused on a spot and this spot is moved around the sample surface to obtain the image, whereas in standard TEM the entire sample surface is illuminated at once. Therefore, STEM can go down to atomic resolution and still have the ability to detect different atomic species due to its Z contrast (Z is the atomic number). In addition, STEM can provide information about the chemical environment by using energy dispersive X-ray spectroscopy (EDS) or electron energy loss spectroscopy (EELS). The most interesting feature for this project is the ability to measure charge localization and electric fields [174–182]. This can be used to gain further insight into large twist angle TBLG. The capabilities of STEM provide a complementary technique to the investigation of TBLG in STM. At a twist angle of 21.78°, TBLG is expected to be a topological insulator. Therefore, there are topologically protected corner states are expected for these large twist angles.[75]. These corner states should appear at the edges of the single graphene flakes and are expected to be detectable with STEM.

To study TBLG heterostructures in (S)TEM, they must be placed on a TEM grid. This is necessary to be able to detect the transmitted electrons. Therefore, the TBLG heterostructures are truly free standing in the TEM due to the design of the TEM grids. The freestanding TBLG is therefore not influenced by the underlying substrate, as this is the case in STM investigations. A disadvantage of these TEM grids is the difficulty of transferring TBLG heterostructures onto them. Therefore, in this chapter the transfer of exfoliated and stacked TBLG onto different types of TEM grids will be investigated and discussed.

7.2 Different Approaches for Sample Preparation

Sample preparation involves exfoliation and stacking, as with the STM sample. Exfoliating the required graphene flakes is done in the same way as described above for the STM samples. The main difference is the substrate. Previously, it was an Au-coated Si wafer; however, for the TEM samples, a TEM grid is needed. There are different types of grids. Some grids have a series of holes, while others have thin areas. The sample of interest is placed on these holes or thin areas. These holes or thin areas are necessary because the TEM measures transmitted electrons. These electrons come from the microscope, scatter within the sample, and exit on the opposite side. If the substrate were too thick, the electrons would not be able to pass through after scattering within the sample. These grids are problematic when transferring heterostructures using a polymer stamp. The issues with these grids during transfer will be discussed later. The following describes different approaches and their results that were tested in this work. The main difference between these approaches is the choice of TEM grid.

The first attempt to transfer TBLG to a TEM grid used a Cu grid. The heterostructure was picked up similarly to the sample for STM, but with two differences. First, thick hBN and graphite flakes are not needed under the TBLG. These would block the transmitted electrons necessary for TEM. Second, the heterostructure for the STM sample mainly uses standalone monolayer graphene flakes. In this case, one of the monolayer graphene flakes must have an additional part with a height of a few nm attached to it. This allows for easier tuning of the TEM focus to the correct focal point on the graphene. Additionally, the presence of other graphene or graphite flakes in the surrounding area

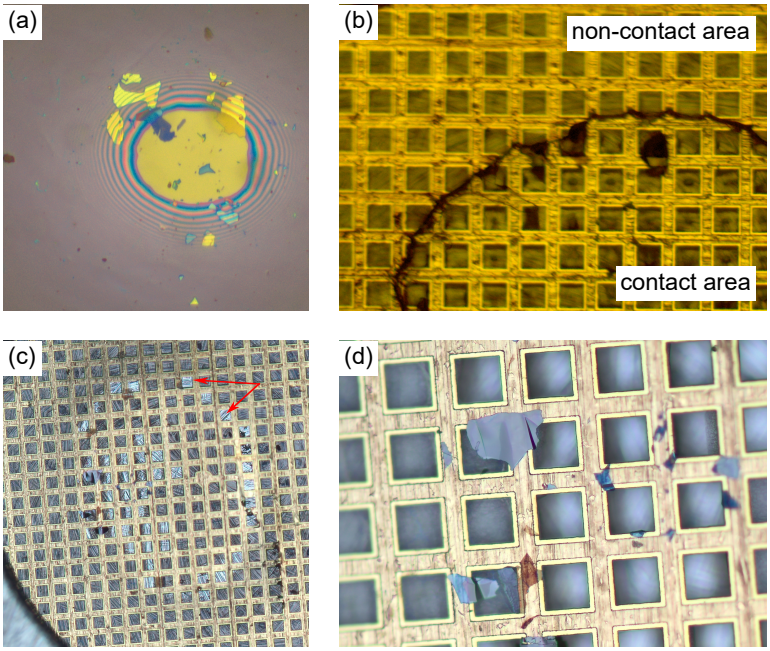

Fig. 7.1: Optical microscopy images of the transfer of heterostructures onto the Cu Grid. (a) Image during the pick-up process (yellow circle is the contact area), (b) image of the contact area on the Cu grid during the drop-down, (c) overview image of the Cu grid after the transfer, (d) zoomed image of the deposited flakes on the grid, the difference between the intact lacey carbon in the left squares and the broken ones on the right can be observed.

does not pose a problem due to the localized nature of TEM measurements.

Fig. 7.1 (a) shows an example of picking up part of the heterostructure, where thicker graphite flakes are also located in the contact area of the stamp. Fig. 7.1 (b) shows a step in the process of dropping these flakes onto the Cu grid. The dark line indicates the edge of the contact area. The contrast difference between the center of the contact area (lower right) and the non-contact area (upper right) is very small in the optical microscope, which makes precise control of the stamp more difficult than with a Au-coated Si wafer. The squares observed in the image are from the Cu grid. The grid consists of

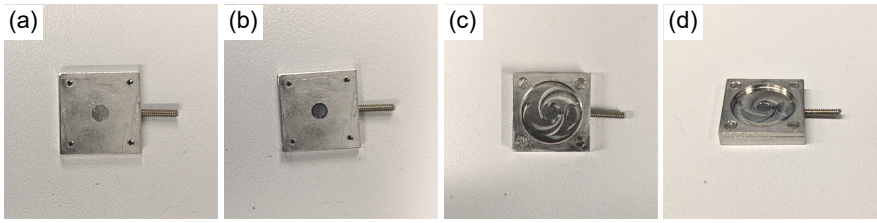

Fig. 7.2: Photos of the sample holder: (a) empty bottom plate with the small recess for the grid, (b) grid placed in the recess of the bottom plate, (c) top view of the grid mounted in the sample holder, (d) side view of (c).

many square holes, and its mesh is 300, which corresponds to approximate hole widths of 62 μm and bridge widths of 20 μm. The mesh is the number of holes in one inch. The entire Cu grid is covered with a film of lacey carbon, which is an amorphous carbon film with irregularly large holes. This film's purpose is to support the deposited pattern between the Cu bridges. The entire grid is only 3 μm in diameter. Due to its small size, as well as its thinness and resulting mechanical instability, we had to design a special sample holder to mount the TEM grid. The sample holder is shown in Fig. 7.2. Panel (a) shows the empty bottom plate. The bottom plate has a 0.02 mm deep recess in the center to prevent the grid from moving during mounting. Panel (b) shows the grid loosely placed in the recess of the bottom plate. Panels (c) and (d) show the fully mounted grid in the sample holder from the top and side, respectively. This layout ensures that the grid can be used as a transport substrate and held in position on the transfer stage. However, for stability reasons, the top plate has a thick edge that interferes with the standard stamp layout. Therefore, an additional PDMS block is placed between the PDMS drop and the microscope slide. This makes the stamp thicker and allows it to contact the TEM grid. One disadvantage of this PDMS block is the reduced transparency when looking through the stamp during transfer. This reduces controllability of the entire process, from picking up to stacking to dropping the heterostructure.

In addition to the sample holder, the polymer used for the TEM samples has also changed. In this case, the polymer used for the stamp is not PC, but rather a nail polish (*Revlon Extra Life No Chip Top Coat*). The nail polish is spin-coated and placed on

the apex of the PDMS drop [183]. The PDMS is separated from the nail polish using Scotch tape to prevent reaction between the two materials during heating. Unlike PC films, nail polish does not require a large contact area to release the heterostructure, which is a great advantage. This is crucial for reducing the force on these fragile TEM grids. Therefore, one must be very careful when transferring to the TEM grid. To pick up the desired flakes, the stamp is brought into contact with the flake and the surrounding substrate at 60°C for 10 min (Fig. 7.1 (a)). Then, slowly and continuously, the stamp is retracted. For placement, the Cu grid is also heated to 60°C and brought into contact with the stamp. To release the structure, melt the nail polish film at 130°C and slowly retract the stamp (Fig. 7.1 (b)). To remove the nail polish, place the TEM grid in acetone for one hour, then briefly dip it in IPA. The main difficulties with this transfer process are that the stamp's contact area on the grid is barely visible under the optical microscope on the transfer stage, and the lacy carbon film can break easily during transfer.

The first transferred sample was only partially successful. The main problem was that the TBLG was placed on the wrong side of the Cu grid, on the side opposite the lacey carbon film. Additionally, it was unclear if the monolayers survived the transfer because they could not be detected on the TEM grid due to their low optical contrast. The collaborators in Marburg could not resolve the regions of the monolayer. This was likely due to the sample being on the wrong side and difficulties focusing on this part of the grid. Another attempt on the correct side is shown in Fig. 7.1. The images shown here are representative of transfers onto Cu grids. A larger overview of the Cu grid after transfer is shown in Fig. 7.1 (c). The brighter squares are where the lacey carbon film broke upon contact, as indicated by the red arrows. The zoomed image (Fig. 7.1 (d)) shows the larger graphite flakes, but no graphene monolayer. It is also not possible to visualize the graphene monolayers on the right side by optical microscopy. Further attempts to transfer graphene onto the Cu grid resulted in the lacey carbon breaking due to the stamp's force or the flakes not surviving the transfer. In addition to spin-coating the nail polish, one can place a drop of nail polish on the apex of the PDMS drop. However, this did not increase the success rate, so the Cu grid transfer method was abandoned, and new options were considered.

The second attempt involved transferring the TBLG heterostructure onto sapphire glass,

followed by transferring it using a poly-(methyl methacrylate) (PMMA) wet transfer onto the TEM grid, which was performed by collaborators in Marburg. To transfer the heterostructure onto the sapphire glass, we used the standard stamp layout described in the STM chapter with a nail polish droplet on top. The typical cleaning routine for the substrates first involved an ultrasonic bath with acetone and IPA, followed by UV-ozone treatment of the sapphire glass. During UV-ozone treatment, UV light splits ozone into reactive parts that oxidize residues on the surface, which can then be removed. Unfortunately, this cleaning process was insufficient for cleaning sapphire properly. Therefore, a cleaning polymer (Red First Contact Polymer) was applied, which efficiently removed the residues from the sapphire glass. Transferring the heterostructure to the sapphire glass was straightforward and effective.

Two samples are shown in Fig. 7.3 (a) and (c). One significant challenge was locating the heterostructure in the optical microscope. Monolayers can only be observed within a certain color range of blue light, as seen in both Fig. 7.3 (b) and (d). The lighter blue areas are graphene monolayers; however, as can be seen, the contrast is weak. Two transferred heterostructures were sent to Marburg for PMMA transfer onto the TEM grid. For this transfer, the entire sapphire glass (with the heterostructures on top) was spin-coated with PMMA. Then, the heterostructure on the PMMA can be separated from the sapphire by submerging it in water. To transfer the heterostructure with PMMA onto the TEM grid, it must be lifted with the grid. Then, the PMMA is dissolved with acetone. However, due to the small size of the exfoliated heterostructures, this step was unsuccessful. Therefore, this method of preparing TBLG samples for TEM was abandoned.

The next type of TEM grid was the SiN grid. These grids have different layouts. The first SiN grid layout is shown in Fig. 7.4 (a), with an enlargement shown in (b). Six small holes in the middle allow examination of the heterostructure placed on top. The attempted transfer is shown in Fig. 7.4 (c). Here, the contact area is clearly visible during the transfer. Unfortunately, the middle part was not stable enough for the transfer. The broken middle center part is visible as the black area in Fig. 7.4 (d), indicated by the red arrow.

The next type is a SiN wafer with a thin (5-20 nm) square window. The heterostructure

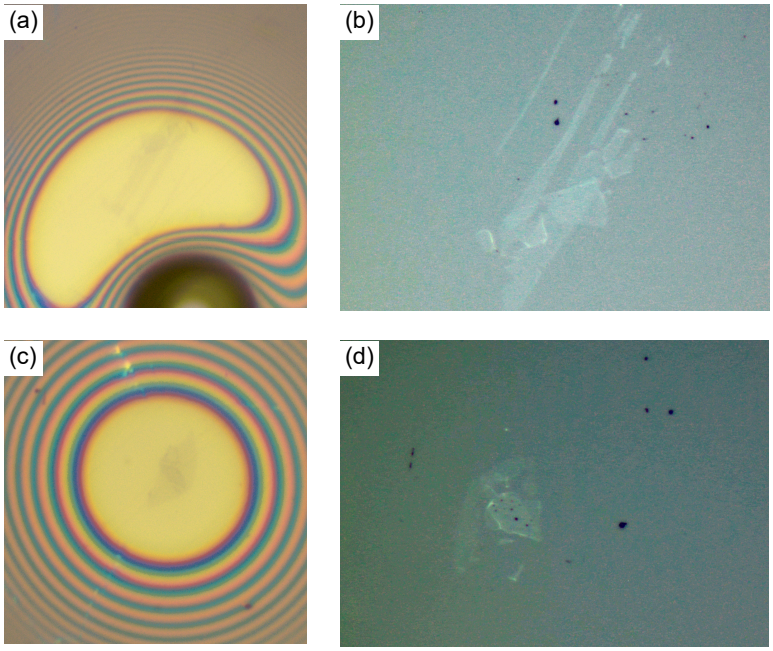

Fig. 7.3: Optical microscopy images of the transfer of heterostructures on to the sapphire glass. (a), (c) Images during the pickup process (yellow circle is the contact area), (b), (d) Images of the deposited flakes onto the sapphire glass. The contrast of the monolayer on the sapphire glass is rather weak.

is placed on the thinner part of the SiN grid. The purpose of the thin window is to enable measurement through the thin amorphous SiN layer. To transfer onto the SiN grid, the grid must be UV-ozoned shortly before the heterostructure is placed on it; otherwise, the graphene layers will not adhere to the SiN and will be washed away during cleaning. Generally, the interaction strength between graphene and the SiN grid is weak because transferred monolayer parts of graphene roll up on the grid. This effect is observed in Fig. 7.4 (e), where the edges of the TBLG are thicker due to the rolled-up graphene monolayers. Therefore, only the twisted region survives the transfer properly. The transfer on such a SiN window also has a chance to break the SiN window (Fig. 7.4 (f)), because this window has to be very thin in order to measure through. A sample of this

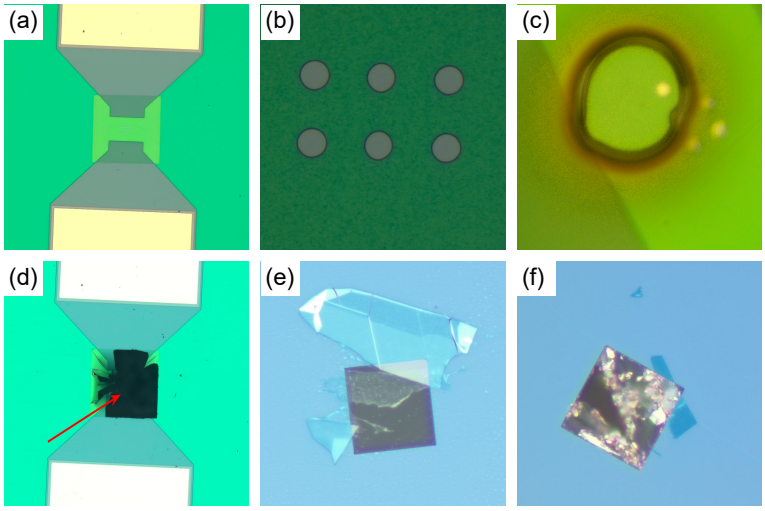

Fig. 7.4: Optical microscopy images of the transfer of heterostructures onto SiN grids. (a) Large image of the layout of one SiN grid design, (b) zoom in to the center of (a) showing the 6 small holes for TEM, (c) image during the transfer of the heterostructure onto the holes. The dark brown circle at the edges indicates the contact area. (d) Same section as in (a) but after the transfer. The central area has been completely broken during the transfer process (the black areas are broken off). (e) Optical microscopy image of a successful transfer on a thin SiN window (f) Similar to (e), but the SiN window broke during the transfer.

type was examined by TEM in Marburg; however, the amorphous background of the thin SiN was quite high, even though the transfer was already at the edge of mechanical stability. Additionally, the carbon species (in this case, graphene) scatters electrons weakly due to its small size (low atomic number). Therefore, the intensity contrast of graphene is low compared to the background level [176, 178, 180]. In a new attempt, a nanoporous SiN grid was used instead. This grid has many small holes in the nanometer range. Thus, the amorphous background could be ignored, as TEM measurements could be performed on these small holes. However, these nanoporous structures were not mechanically stable enough for polymer transfer of the heterostructure. During all attempts, the nanoporous region broke during transfer or cleaning.

7.3 Summary and Outlook

This work investigated three different types of transfers onto TEM grids. Transferring directly onto the Cu grid with a lacey carbon film was unsuccessful. The lacey carbon film is too fragile and tends to break during transfer. The forces of the polymer stamp are probably too high for the strength of the lacey carbon film. Additionally, the deposited heterostructure must be cleaned within the molten polymer, and it is sometimes simply washed away. Other polymer transfer methods, such as the flip technique [46], are not applicable to this type of transfer onto the TEM grid. The PVC used has too small of a contact area when releasing the heterostructure. Additionally, the heterostructure is strongly bound to the PVC, requiring a strong interaction with the TEM grid. The combination of the strong force due to the contact area and the bond strength between the heterostructure and the PVC stamp renders this method unsuitable.

Transferring the heterostructure to sapphire glass is manageable, although the sapphire glass must be prepared to ensure the heterostructure can be found later. However, subsequent transfer with PMMA from the sapphire glass to the TEM grid was unsuccessful. The most likely reason is that the heterostructures are too small.

Finally, the SiN grids were used for the transfer test. Two problems arose during trials on different types of SiN grids. First, the very thin SiN films and nanoporous SiN parts are not mechanically stable enough to withstand the forces that occur during transfer with a polymer stamp. The second problem was with the thin SiN windows, for which the transfer worked with at least a decent success rate. These SiN windows exhibit a significant amorphous background in TEM measurements due to the strong dependence of TEM intensity on atomic number. This relationship creates a poor contrast difference between graphene and SiN, making nice measurements almost impossible. One possible solution is to prepare special SiN grids. For example, one could use a thick SiN layer with small holes. This grid would still be strong enough and would not show a strong background in TEM measurements.

For further experiments, another option is to use TEM grids similar to the Cu grid but without a coating layer of lacey carbon or graphene. Rather than stabilizing the het-

erostructures with these layers, the grid would require a much higher mesh with smaller holes so that the grid is stable and the heterostructure lies on top of several holes. One potential problem is that the contact area between the heterostructure and the grid would be small, so the heterostructure could be washed away during cleaning.

8 Summary and Outlook

In this thesis, different approaches to modify the properties of graphene have been discussed. First, the intercalation possibilities of epitaxially grown graphene were explored using NIXSW, with a focus on Bi and Se intercalation. In addition to intercalation, epitaxial graphene can be modified by twisting two graphene layers by 30°. Two different samples were prepared that differ significantly in structure. To obtain a greater variety of twist angles, exfoliation and stacking techniques were applied to twisted bilayer graphene. Near magic angle twisted bilayer graphene samples were investigated using STM and STS. Additionally, different methods for preparing twisted bilayer graphene samples for further TEM investigation were explored.

In chapter 3, the intercalation of epitaxial graphene on SiC(0001) with Bi was investigated. Prior to this work, two different phases were detected. These phases differ in their horizontal structure as well as in their electronic properties. While the α phase shows metallic bands and a (1x1) reconstruction of the Bi atoms with respect to the substrate, the β phase has less Bi atoms in the intercalant layer ($\sqrt{3}$x$\sqrt{3}$)R30° reconstruction) and insulating bands are observed. In this work, the vertical structure of both phases has been studied by NIXSW. For both the α and β phases, a van-der-Waals bonding distance from Bi to graphene was found, which is another indication of the successful decoupling of the graphene from the substrate. While the β phase has a significantly lower amount of Bi in its intercalant layer, all the dangling bonds of the SiC surface are saturated. The bond distances also remain almost the same, with a slightly smaller distance for the β phase than for the α phase. Although this distance is only 0.05 Å, the difference is not due to a measurement artifact, since the height of the graphene is shifted closer to the substrate by the same amount. The changes in the horizontal structure during the phase transition could not be resolved yet.

Chapter 4 discusses the second variant chosen for graphene intercalation. In this case, the chosen element was Se, as in previous work on intercalating graphene with TMDCs. The vertical structure of Se-intercalated graphene on SiC(0001) was determined using the NIXSW technique. The first sample investigated was homogeneous across its entire surface. It exhibited high coherent fractions for all species except the graphene signal. The poor coherence of 0.38 for graphene indicates buckling of the graphene layer. To determine whether this low coherence is intrinsic to the system or due to sample quality, a new, similar sample was prepared and examined. This sample did not exhibit a low coherent fraction; rather, it exhibited a coherent fraction typical of graphene. The interlayer distances were found to be within the range of covalent distances for the Se-Si bond while maintaining the van der Waals distance between Se and graphene. As with the Bi intercalation, this again shows the successful intercalation and decoupling of the graphene layer on top.

In Chapter 5, twisted bilayer graphene was epitaxially grown on SiC(0001). Using the surfactant-mediated growth technique presented by Bocquet et al. [1], a twist angle of 30° was achieved by annealing the SiC substrate in a borazine atmosphere. In this chapter, it was shown that the exact annealing temperature in the graphene growth step is crucial for the resulting quality and structure of the twisted graphene samples. Two samples were grown at different annealing temperatures and showed different electronic properties in ARPES. The characteristic Dirac cone at the $\bar{K}$ of the lower graphene layer could only be observed for the higher annealing temperature. LEEM and especially LEEM-IV show a very different picture for the two samples, while the low-T sample is very homogeneous, the high-T sample shows a mixture of different graphene thicknesses.

Chapter 6 showed the preparation and analysis of twisted bilayer graphene using exfoliation and stacking. The original goal was to create a large twist angle, close to 30Â°. However, the sample studied had a twist angle of only 1.2°, which is close to the magic angle. Two significant findings emerged from this study: the shift of the van Hove singularities and their splitting at the Fermi level, as well as the ability to dope the sample by adjusting the electric field of the scanning tunneling microscope (STM) tip. These effects have been observed in previous studies, but never on the same sample. Additionally, the fitting routines used to detect van Hove singularities were not as sophisticated.

Future experiments will aim to prepare samples with a large twist angle and compare their properties with those of the small twist angle sample investigated here.

Chapter 7 discusses various approaches to preparing twisted bilayer graphene for investigation using TEM. Since TEM involves transmitting electrons through the sample, the heterostructure must be placed on a grid or a very thin substrate. This can lead to stability issues with the substrate or grid, as well as poor adhesion of the graphene to the substrate. This work describes three different transfer methods. All transfers used a polymer stamp made of nail polish. The first substrate used was a Cu grid with a lacey carbon film. The problem with this method was that the lacey carbon film was fragile and often broke during the transfer process. The second attempt involved transferring the heterostructures onto sapphire glass and then transferring the flakes onto a grid using a wet PMMA transfer. While the preparation of twisted bilayer graphene and its deposition onto sapphire is effective, the PMMA transfer has a low success rate. Finally, we investigated transferring onto SiN wafers. In this case, monolayer parts of the graphene do not stick to the SiN; instead, they roll up. Second, SiN substrates in TEM are usually examined through a thin film of SiN, which results in an amorphous background. For high atomic number atoms on top, this problem is minimal, but graphene consists only of carbon atoms and therefore has poor contrast with the SiN background. Additional investigations and new ideas are needed for possible future TEM investigations of twisted bilayer graphene to obtain a suitable sample.

Bibliography

[1] F. C. Bocquet, Y.-R. Lin, M. Franke, N. Samiseresht, S. Parhizkar, S. Soubatch, T.-L. Lee, C. Kumpf, and F. S. Tautz, "Surfactant-Mediated Epitaxial Growth of Single-Layer Graphene in an Unconventional Orientation on SiC", Phys. Rev. Lett. **125**, 106102 (2020).

[2] G. E. Moore, "Cramming more components onto integrated circuits, Reprinted from Electronics, volume 38, number 8, April 19, 1965, pp.114 ff.", IEEE Solid-State Circuits Society Newsletter **11**, 33 (2006).

[3] R. W. Keyes, "Physical limits of silicon transistors and circuits", Rep. Prog. Phys. **68**, 2701 (2005).

[4] K. S. Novoselov, A. K. Geim, S. V. Morozov, D. Jiang, Y. Zhang, S. V. Dubonos, I. V. Grigorieva, and A. A. Firsov, "Electric Field Effect in Atomically Thin Carbon Films", Science **306**, 666 (2004).

[5] A. K. Geim and K. S. Novoselov, "The rise of graphene", Nature Mater **6**, 183 (2007).

[6] F. Schwierz, "Graphene transistors", Nature Nanotech **5**, 487 (2010).

[7] J. Zhao, P. Ji, Y. Li, R. Li, K. Zhang, H. Tian, K. Yu, B. Bian, L. Hao, X. Xiao, W. Griffin, N. Dudeck, R. Moro, L. Ma, and W. A. de Heer, "Ultrahigh-mobility semiconducting epitaxial graphene on silicon carbide", Nature **625**, 60 (2024).

[8] G. Gui, D. Morgan, J. Booske, J. Zhong, and Z. Ma, "Local strain effect on the band gap engineering of graphene by a first-principles study", Applied Physics Letters **106**, 053113 (2015).

[9] K. Iyakutti, "Band Gap Engineering in the 2D Wonder Material Graphene: A Review of our Computational approach", Journal of Chennai Academy of Sciences **2**, 1 (2020).

[10] K. I. Bolotin, K. J. Sikes, Z. Jiang, M. Klima, G. Fudenberg, J. Hone, P. Kim, and H. L. Stormer, "Ultrahigh electron mobility in suspended graphene", Solid State Communications **146**, 351 (2008).

[11] N. Arora, J. Hauser, and D. Roulston, "Electron and hole mobilities in silicon as a function of concentration and temperature", IEEE Transactions on Electron Devices **29**, 292 (1982).

[12] B. G. Streetman and S. K. Banerjee, *Solid state electronic devices*, 7. ed., global ed, Always Learning (Pearson, Boston Munich, 2016).

[13] W. Zhai, "Enhancing Microchip Performance Through Graphene Integration: A Comparative Analysis with Silicon", Highlights in Science, Engineering and Technology **125**, 428 (2025).

[14] H. Cheun Lee, W.-W. Liu, S.-P. Chai, A. Rahman Mohamed, A. Aziz, C.-S. Khe, N. M. S. Hidayah, and U. Hashim, "Review of the synthesis, transfer, characterization and growth mechanisms of single and multilayer graphene", RSC Advances **7**, 15644 (2017).

[15] A. Santhiran, P. Iyngaran, P. Abiman, and N. Kuganathan, "Graphene Synthesis and Its Recent Advances in Applications—A Review", C **7**, 76 (2021).

[16] Y. Cao, V. Fatemi, S. Fang, K. Watanabe, T. Taniguchi, E. Kaxiras, and P. Jarillo-Herrero, "Unconventional superconductivity in magic-angle graphene superlattices", Nature **556**, 43 (2018).

[17] Y. Huang, Y.-H. Pan, R. Yang, L.-H. Bao, L. Meng, H.-L. Luo, Y.-Q. Cai, G.-D. Liu, W.-J. Zhao, Z. Zhou, L.-M. Wu, Z.-L. Zhu, M. Huang, L.-W. Liu, L. Liu, P. Cheng, K.-H. Wu, S.-B. Tian, C.-Z. Gu, Y.-G. Shi, Y.-F. Guo, Z. G. Cheng, J.-P. Hu, L. Zhao, G.-H. Yang, E. Sutter, P. Sutter, Y.-L. Wang, W. Ji, X.-J. Zhou, and H.-J. Gao, "Universal mechanical exfoliation of large-area 2D crystals", Nat Commun **11**, 2453 (2020).

[18] D. Wong, K. P. Nuckolls, M. Oh, B. Lian, Y. Xie, S. Jeon, K. Watanabe, T. Taniguchi, B. A. Bernevig, and A. Yazdani, "Cascade of electronic transitions in magic-angle twisted bilayer graphene", Nature **582**, 198 (2020).

[19] Y. Jiang, X. Lai, K. Watanabe, T. Taniguchi, K. Haule, J. Mao, and E. Y. Andrei, "Charge order and broken rotational symmetry in magic-angle twisted bilayer graphene", Nature **573**, 91 (2019).

[20] F. Joucken, C. Bena, Z. Ge, E. Quezada-Lopez, S. Pinon, V. Kaladzhyan, T. Taniguchi, K. Watanabe, A. Ferreira, and J. J. Velasco, "Direct Visualization of Native Defects in Graphite and Their Effect on the Electronic Properties of Bernal-Stacked Bilayer Graphene", Nano Lett. **21**, 7100 (2021).

[21] M. Oh, K. P. Nuckolls, D. Wong, R. L. Lee, X. Liu, K. Watanabe, T. Taniguchi, and A. Yazdani, "Evidence for unconventional superconductivity in twisted bilayer graphene", Nature **600**, 240 (2021).

[22] T. Benschop, T. A. de Jong, P. Stepanov, X. Lu, V. Stalman, S. J. van der Molen, D. K. Efetov, and M. P. Allan, "Measuring local moiré lattice heterogeneity of twisted bilayer graphene", Phys. Rev. Res. **3**, 013153 (2021).

[23] K. Kim, M. Yankowitz, B. Fallahazad, S. Kang, H. C. P. Movva, S. Huang, S. Larentis, C. M. Corbet, T. Taniguchi, K. Watanabe, S. K. Banerjee, B. J. LeRoy, and E. Tutuc, "Van der Waals Heterostructures with High Accuracy Rotational Alignment", Nano Lett. **16**, 1989 (2016).

[24] P. Wu, W. Zhang, Z. Li, and J. Yang, "Mechanisms of Graphene Growth on Metal Surfaces: Theoretical Perspectives", Small **10**, 2136 (2014).

[25] X. Li, W. Cai, J. An, S. Kim, J. Nah, D. Yang, R. Piner, A. Velamakanni, I. Jung, E. Tutuc, S. K. Banerjee, L. Colombo, and R. S. Ruoff, "Large-Area Synthesis of High-Quality and Uniform Graphene Films on Copper Foils", Science **324**, 1312 (2009).

[26] C. M. Orofeo, H. Ago, B. Hu, and M. Tsuji, "Synthesis of large area, homogeneous, single layer graphene films by annealing amorphous carbon on Co and Ni", Nano Res. **4**, 531 (2011).

[27] C. Li, D. Li, J. Yang, X. Zeng, and W. Yuan, "Preparation of Single- and Few-Layer Graphene Sheets Using Co Deposition on SiC Substrate", Journal of Nanomaterials **2011**, e319624 (2011).

[28] S. Kraus, F. Huttmann, J. Fischer, T. Knispel, K. Bischof, A. Herman, M. Bianchi, R.-M. Stan, A. J. Holt, V. Caciuc, S. Tsukamoto, H. Wende, P. Hofmann, N. Atodiresei, and T. Michely, "Single-crystal graphene on Ir(110)", Phys. Rev. B **105**, 165405 (2022).

[29] C. Riedl, C. Coletti, and U. Starke, "Structural and electronic properties of epitaxial graphene on SiC(0 0 0 1): a review of growth, characterization, transfer doping and hydrogen intercalation", J. Phys. D: Appl. Phys. **43**, 374009 (2010).

[30] C. Riedl, U. Starke, J. Bernhardt, M. Franke, and K. Heinz, "Structural properties of the graphene-SiC(0001) interface as a key for the preparation of homogeneous large-terrace graphene surfaces", Phys. Rev. B **76**, 245406 (2007).

[31] C. Riedl, C. Coletti, T. Iwasaki, A. A. Zakharov, and U. Starke, "Quasi-Free-Standing Epitaxial Graphene on SiC Obtained by Hydrogen Intercalation", Phys. Rev. Lett. **103**, 246804 (2009).

[32] U. Starke and C. Riedl, "Epitaxial graphene on SiC(0001) and SiC(000$\bar{1}$): from surface reconstructions to carbon electronics", J. Phys.: Condens. Matter **21**, 134016 (2009).

[33] C. Virojanadara, M. Syväjarvi, R. Yakimova, L. I. Johansson, A. A. Zakharov, and T. Balasubramanian, "Homogeneous large-area graphene layer growth on 6H-SiC(0001)", Phys. Rev. B **78**, 245403 (2008).

[34] Luxmi, N. Srivastava, R. M. Feenstra, and P. J. Fisher, "Formation of epitaxial graphene on SiC(0001) using vacuum or argon environments", Journal of Vacuum Science & Technology B **28**, C5C1 (2010).

[35] M. Beshkova, L. Hultman, and R. Yakimova, "Device applications of epitaxial graphene on silicon carbide", Vacuum **128**, 186 (2016).

[36] A. Pradeepkumar, D. Cortie, E. Smyth, A. P. L. Brun, and F. Iacopi, "Epitaxial graphene growth on cubic silicon carbide on silicon with high temperature neutron reflectometry: an operando study", RSC Adv. **14**, 3232 (2024).

[37] K. E. Whitener and P. E. Sheehan, "Graphene synthesis", Diamond and Related Materials **46**, 25 (2014).

[38] V. Singh, D. Joung, L. Zhai, S. Das, S. I. Khondaker, and S. Seal, "Graphene based materials: Past, present and future", Progress in Materials Science **56**, 1178 (2011).

[39] P. R. Somani, S. P. Somani, and M. Umeno, "Planer nano-graphenes from camphor by CVD", Chemical Physics Letters **430**, 56 (2006).

[40] T. Wu, G. Ding, H. Shen, H. Wang, L. Sun, D. Jiang, X. Xie, and M. Jiang, "Triggering the Continuous Growth of Graphene Toward Millimeter-Sized Grains", Advanced Functional Materials **23**, 198 (2013).

[41] Z. Li, P. Wu, C. Wang, X. Fan, W. Zhang, X. Zhai, C. Zeng, Z. Li, J. Yang, and J. Hou, "Low-Temperature Growth of Graphene by Chemical Vapor Deposition Using Solid and Liquid Carbon Sources", ACS Nano **5**, 3385 (2011).

[42] X. Gan, H. Zhou, B. Zhu, X. Yu, Y. Jia, B. Sun, M. Zhang, X. Huang, J. Liu, and T. Luo, "A simple method to synthesize graphene at 633 K by dechlorination of hexachlorobenzene on Cu foils", Carbon **50**, 306 (2012).

[43] J. Cai, P. Ruffieux, R. Jaafar, M. Bieri, T. Braun, S. Blankenburg, M. Muoth, A. P. Seitsonen, M. Saleh, X. Feng, K. Müllen, and R. Fasel, "Atomically precise bottom-up fabrication of graphene nanoribbons", Nature **466**, 470 (2010).

[44] P. B. Bennett, Z. Pedramrazi, A. Madani, Y.-C. Chen, D. G. de Oteyza, C. Chen, F. R. Fischer, M. F. Crommie, and J. Bokor, "Bottom-up graphene nanoribbon field-effect transistors", Applied Physics Letters **103**, 253114 (2013).

[45] T. H. Vo, M. Shekhirev, D. A. Kunkel, M. D. Morton, E. Berglund, L. Kong, P. M. Wilson, P. A. Dowben, A. Enders, and A. Sinitskii, "Large-scale solution synthesis of narrow graphene nanoribbons", Nat Commun **5**, 3189 (2014).

[46] K. Jin, T. Wichmann, S. Wenzel, T. Samuely, O. Onufriienko, P. Szabó, K. Watanabe, T. Taniguchi, J. Yan, F. S. Tautz, F. Lüpke, M. Ternes, and J. Martinez-Castro, "Assembly of Arbitrary Designer Heterostructures with Atomically Clean Interfaces", Advanced Materials Interfaces **11**, 2300658 (2024).

[47] F. Pizzocchero, L. Gammelgaard, B. S. Jessen, J. M. Caridad, L. Wang, J. Hone, P. Bøggild, and T. J. Booth, "The hot pick-up technique for batch assembly of van der Waals heterostructures", Nat Commun **7**, 11894 (2016).

[48] S. Wolff, S. Roscher, F. Timmermann, M. V. Daniel, F. Speck, M. Wanke, M. Albrecht, and T. Seyller, "Quasi-Freestanding Graphene on SiC(0001) by Ar-Mediated Intercalation of Antimony: A Route Toward Intercalation of High-Vapor-Pressure Elements", Ann. Phys. (Berlin) **531**, 1900199 (2019).

[49] Y.-R. Lin, S. Wolff, P. Schädlich, M. Hutter, S. Soubatch, T.-L. Lee, F. S. Tautz, T. Seyller, C. Kumpf, and F. C. Bocquet, "Vertical structure of Sb-intercalated quasifreestanding graphene on SiC(0001)", Phys. Rev. B **106**, 155418 (2022).

[50] Y. Sohn, S. W. Jung, F. Göhler, W. J. Shin, S. Cha, T. Seyller, and K. S. Kim, "Electronic band structure of Bi-intercalate layers in graphene and SiC(0001)", J. Korean Phys. Soc. **78**, 157 (2021).

[51] S. Forti, A. Stöhr, A. A. Zakharov, C. Coletti, K. V. Emtsev, and U. Starke, "Mini-Dirac cones in the band structure of a copper intercalated epitaxial graphene superlattice", 2D Mater. **3**, 035003 (2016).

[52] K. V. Emtsev, A. A. Zakharov, C. Coletti, S. Forti, and U. Starke, "Ambipolar doping in quasifree epitaxial graphene on SiC(0001) controlled by Ge intercalation", Phys. Rev. B **84**, 125423 (2011).

[53] I. Gierz, T. Suzuki, R. T. Weitz, D. S. Lee, B. Krauss, C. Riedl, U. Starke, H. Höchst, J. H. Smet, C. R. Ast, and K. Kern, "Electronic decoupling of an epitaxial graphene monolayer by gold intercalation", Phys. Rev. B **81**, 235408 (2010).

[54] S. Forti, S. Link, A. Stöhr, Y. Niu, A. A. Zakharov, C. Coletti, and U. Starke, "Semiconductor to metal transition in two-dimensional gold and its van der Waals heterostack with graphene", Nat Commun **11**, 2236 (2020).

[55] F. Speck, J. Jobst, F. Fromm, M. Ostler, D. Waldmann, M. Hundhausen, H. B. Weber, and T. Seyller, "The quasi-free-standing nature of graphene on H-saturated SiC(0001)", Applied Physics Letters **99**, 122106 (2011).

[56] H. Kim, N. Tsogtbaatar, B. Tuvdendorj, A. Lkhagvasuren, and J. M. Seo, "Effects of two kinds of intercalated In films on quasi-free-standing monolayer graphene formed above SiC(0001)", Carbon **159**, 229 (2020).

[57] P. Schädlich, C. Ghosal, M. Stettner, B. Matta, S. Wolff, F. Schölzel, P. Richter, M. Hutter, A. Haags, S. Wenzel, Z. Mamiyev, J. Koch, S. Soubatch, P. Rosenzweig, C. Polley, F. S. Tautz, C. Kumpf, K. Küster, U. Starke, T. Seyller, F. C. Bocquet, and C. Tegenkamp, "Domain Boundary Formation Within an Intercalated Pb Monolayer Featuring Charge-Neutral Epitaxial Graphene", Advanced Materials Interfaces **10**, 2300471 (2023).

[58] M. Gruschwitz, C. Ghosal, T.-H. Shen, S. Wolff, T. Seyller, and C. Tegenkamp, "Surface Transport Properties of Pb-Intercalated Graphene", Materials **14**, 7706 (2021).

[59] B. Matta, P. Rosenzweig, O. Bolkenbaas, K. Küster, and U. Starke, "Momentum microscopy of Pb-intercalated graphene on SiC: Charge neutrality and electronic structure of interfacial Pb", Phys. Rev. Research **4**, 023250 (2022).

[60] S. Oida, F. R. McFeely, J. B. Hannon, R. M. Tromp, M. Copel, Z. Chen, Y. Sun, D. B. Farmer, and J. Yurkas, "Decoupling graphene from SiC(0001) via oxidation", Phys. Rev. B **82**, 041411 (2010).

[61] M. Ostler, F. Fromm, R. J. Koch, P. Wehrfritz, F. Speck, H. Vita, S. Böttcher, K. Horn, and T. Seyller, "Buffer layer free graphene on SiC(0 0 0 1) via interface oxidation in water vapor", Carbon **70**, 258 (2014).

[62] Z. Mamiyev and C. Tegenkamp, "Sn intercalation into the BL/SiC(0001) interface: A detailed SPA-LEED investigation", Surfaces and Interfaces **34**, 102304 (2022).

[63] G. Profeta, M. Calandra, and F. Mauri, "Phonon-mediated superconductivity in graphene by lithium deposition", Nature Phys **8**, 131 (2012).

[64] R. Bistritzer and A. H. MacDonald, "Moiré bands in twisted double-layer graphene", Proceedings of the National Academy of Sciences **108**, 12233 (2011).

[65] S. Carr, S. Fang, Z. Zhu, and E. Kaxiras, "Exact continuum model for low-energy electronic states of twisted bilayer graphene", Phys. Rev. Res. **1**, 013001 (2019).

[66] M. Koshino, N. F. Q. Yuan, T. Koretsune, M. Ochi, K. Kuroki, and L. Fu, "Maximally Localized Wannier Orbitals and the Extended Hubbard Model for Twisted Bilayer Graphene", Phys. Rev. X **8**, 031087 (2018).

[67] H. C. Po, L. Zou, A. Vishwanath, and T. Senthil, "Origin of Mott Insulating Behavior and Superconductivity in Twisted Bilayer Graphene", Phys. Rev. X **8**, 031089 (2018).

[68] J. Liu, J. Liu, and X. Dai, "Pseudo Landau level representation of twisted bilayer graphene: Band topology and implications on the correlated insulating phase", Phys. Rev. B **99**, 155415 (2019).

[69] A. Nimbalkar and H. Kim, "Opportunities and Challenges in Twisted Bilayer Graphene: A Review", Nano-Micro Lett. **12**, 126 (2020).

[70] M. G. Scheer, K. Gu, and B. Lian, "Magic angles in twisted bilayer graphene near commensuration: Towards a hypermagic regime", Phys. Rev. B **106**, 115418 (2022).

[71] Z.-D. Song and B. A. Bernevig, "Magic-Angle Twisted Bilayer Graphene as a Topological Heavy Fermion Problem", Phys. Rev. Lett. **129**, 047601 (2022).

[72] G. Li, A. Luican, J. M. B. Lopes dos Santos, A. H. Castro Neto, A. Reina, J. Kong, and E. Y. Andrei, "Observation of Van Hove singularities in twisted graphene layers", Nature Phys **6**, 109 (2010).

[73] J. Yin, H. Wang, H. Peng, Z. Tan, L. Liao, L. Lin, X. Sun, A. L. Koh, Y. Chen, H. Peng, and Z. Liu, "Selectively enhanced photocurrent generation in twisted bilayer graphene with van Hove singularity", Nat Commun **7**, 10699 (2016).

[74] I. Brihuega, P. Mallet, H. González-Herrero, G. Trambly de Laissardière, M. M. Ugeda, L. Magaud, J. M. Gómez-Rodríguez, F. Ynduráin, and J.-Y. Veuillen, "Unraveling the Intrinsic and Robust Nature of van Hove Singularities in Twisted Bilayer Graphene by Scanning Tunneling Microscopy and Theoretical Analysis", Phys. Rev. Lett. **109**, 196802 (2012).

[75] M. J. Park, Y. Kim, G. Y. Cho, and S. Lee, "Higher-Order Topological Insulator in Twisted Bilayer Graphene", Phys. Rev. Lett. **123**, 216803 (2019).

[76] H. K. Pal, S. Spitz, and M. Kindermann, "Emergent Geometric Frustration and Flat Band in Moiré Bilayer Graphene", Phys. Rev. Lett. **123**, 186402 (2019).

[77] S. J. Ahn, P. Moon, T.-H. Kim, H.-W. Kim, H.-C. Shin, E. H. Kim, H. W. Cha, S.-J. Kahng, P. Kim, M. Koshino, Y.-W. Son, C.-W. Yang, and J. R. Ahn, "Dirac electrons in a dodecagonal graphene quasicrystal", Science **361**, 782 (2018).

[78] J. Zegenhagen, "Surface structure determination with X-ray standing waves", Surface Science Reports **18**, 202 (1993).

[79] G. Materlik and J. Zegenhagen, "X-ray standing wave analysis with synchrotron radiation applied for surface and bulk systems", Physics Letters A **104**, 47 (1984).

[80] D. P. Woodruff, "Surface structure determination using x-ray standing waves", Rep. Prog. Phys. **68**, 743 (2005).

[81] J. Zegenhagen and A. Kazimirov, *The X-Ray Standing Wave Technique: Principles and Applications*, Vol. 7, Series on Synchrotron Radiation Techniques and Applications (World Scientific, Apr. 2013).

[82] D. P. Woodruff, "Normal incidence X-ray standing wave determination of adsorbate structures", Progress in Surface Science **57**, 1 (1998).

[83] M. J. Bedzyk, G. M. Bommarito, and J. S. Schildkraut, "X-ray standing waves at a reflecting mirror surface", Phys. Rev. Lett. **62**, 1376 (1989).

[84] F. C. Bocquet, *TORRICELLI: A software to determine atomic spatial distributions from normal incidence x-ray standing wave data*, Nov. 2018.

[85] C. Nordling, E. Sokolowski, and K. Siegbahn, "Precision Method for Obtaining Absolute Values of Atomic Binding Energies", Phys. Rev. **105**, 1676 (1957).

[86] I. A. Vartanyants and J. Zegenhagen, "Theory of photoelectron emission from an X-ray interference field", in *Series on Synchrotron Radiation Techniques and Applications*, Vol. 7 (World Scientific, Apr. 2013), pp. 181–215.

[87] I. A. Vartanyants and J. Zegenhagen, "Photoelectric scattering from an X-ray interference field", Solid State Communications **113**, 299 (1999).

[88] G. van Straaten, M. Franke, F. C. Bocquet, F. S. Tautz, and C. Kumpf, "Non-dipolar effects in photoelectron-based normal incidence X-ray standing wave experiments", Journal of Electron Spectroscopy and Related Phenomena **222**, 106 (2018).

[89] N. Fairley, *CasaXPS, version 2.3.19PR1.0, Casa Software Ltd.*

[90] *The latest version of the open-source software Torricelli is available online at www.torricelli- software.com.*

[91] Y.-R. Lin, "Structure of two-dimensional multilayers and topological superconductors: surfactant mediated growth, intercalation and doping", PhD thesis (RWTH Aachen, Jülich, Apr. 2023).

[92] G. Binnig and H. Rohrer, "Scanning tunneling microscopy", Surface Science **126**, 236 (1983).

[93] G. Binnig and H. Rohrer, "Scanning tunneling microscopy—from birth to adolescence", Rev. Mod. Phys. **59**, 615 (1987).

[94] L. Mandelstam and M. Leontowitsch, "Zur Theorie der Schrödingerschen Gleichung", Z. Physik **47**, 131 (1928).

[95] L. Esaki, "Long Journey into Tunneling", Science **183**, 1149 (1974).

[96] K. Oura, M. Katayama, A. V. Zotov, V. G. Lifshits, and A. A. Saranin, *Surface Science*, Advanced Texts in Physics (Springer Berlin Heidelberg, Berlin, Heidelberg, 2003).

[97] B. Voigtländer, *Scanning Probe Microscopy: Atomic Force Microscopy and Scanning Tunneling Microscopy*, NanoScience and Technology (Springer Berlin Heidelberg, Berlin, Heidelberg, 2015).

[98] S. Wolff, M. Hutter, P. Schädlich, H. Yin, M. Stettner, S. Wenzel, F. S. Tautz, F. C. Bocquet, T. Seyller, and C. Kumpf, "Bi-intercalated epitaxial graphene on SiC(0001)", New J. Phys. **26**, 103009 (2024).

[99] N. Mishra, J. Boeckl, N. Motta, and F. Iacopi, "Graphene growth on silicon carbide: A review", physica status solidi (a) **213**, 2277 (2016).

[100] S. W. Li, Y. C. Chan, C. H. Hsu, S. Y. Yang, K. Y. Liao, C. H. Ho, C. Y. Chen, H. P. Chen, M. H. Lee, B. Magyari-Köpe, W. S. Yun, T. Y. Lee, I. Radu, J. Z. Huang, C. I. Wu, W. Shue, and M. Cao, "Intercalated Graphene as Next Generation Back-end-of-Line Conductors", in 2023 International Electron Devices Meeting (IEDM) (Dec. 2023), pp. i–iv.

[101] N. Briggs, Z. M. Gebeyehu, A. Vera, T. Zhao, K. Wang, A. D. L. F. Duran, B. Bersch, T. Bowen, K. L. Knappenberger, and J. A. Robinson, "Epitaxial graphene/silicon carbide intercalation: a minireview on graphene modulation and unique 2D materials", Nanoscale **11**, 15440 (2019).

[102] K. Zollner and J. Fabian, "Heterostructures of Graphene and Topological Insulators Bi2Se3, Bi2Te3, and Sb2Te3", physica status solidi (b) **258**, 2000081 (2021).

[103] M.-X. Wang, C. Liu, J.-P. Xu, F. Yang, L. Miao, M.-Y. Yao, C. L. Gao, C. Shen, X. Ma, X. Chen, Z.-A. Xu, Y. Liu, S.-C. Zhang, D. Qian, J.-F. Jia, and Q.-K. Xue, "The Coexistence of Superconductivity and Topological Order in the Bi2Se3 Thin Films", Science **336**, 52 (2012).

[104] A. Fang, C. Adamo, S. Jia, R. J. Cava, S.-C. Wu, C. Felser, and A. Kapitulnik, "Bursting at the seams: Rippled monolayer bismuth on NbSe2", Science Advances **4**, eaaq0330 (2018).

[105] S. Wolff, "Entkopplung von Graphen auf SiC(0001) durch Interkalation", PhD thesis (Technische Universität Chemnitz, 2025).

[106] M. Kruskopf, D. M. Pakdehi, K. Pierz, S. Wundrack, R. Stosch, T. Dziomba, M. Götz, J. Baringhaus, J. Aprojanz, C. Tegenkamp, J. Lidzba, T. Seyller, F. Hohls, F. J. Ahlers, and H. W. Schumacher, "Comeback of epitaxial graphene for electronics: large-area growth of bilayer-free graphene on SiC", 2D Mater. **3**, 041002 (2016).

[107] G. K. Wertheim, P. T. T. M. Van Attekum, and S. Basu, "Electronic structure of lithium graphite", Solid State Communications **33**, 1127 (1980).

[108] G. D. Mahan, "Collective excitations in x-ray spectra of metals", Phys. Rev. B **11**, 4814 (1975).

[109] I. Gierz, C. Riedl, U. Starke, C. R. Ast, and K. Kern, "Atomic Hole Doping of Graphene", Nano Lett. **8**, 4603 (2008).

[110] A. Bondi, "Van der Waals Volumes and Radii", J. Phys. Chem. **68**, 441 (1964).

[111] M. Mantina, A. C. Chamberlin, R. Valero, C. J. Cramer, and D. G. Truhlar, "Consistent van der Waals Radii for the Whole Main Group", J. Phys. Chem. A **113**, 5806 (2009).

[112] P. Pyykkö and M. Atsumi, "Molecular Single-Bond Covalent Radii for Elements 1–118", Chemistry – A European Journal **15**, 186 (2009).

[113] M. J. Bedzyk, P. Fenter, Z. Zhang, L. Cheng, J. S. Okasinski, and N. C. Sturchio, "X-ray Standing Wave Imaging", Synchrotron Radiation News **17**, 5 (2004).

[114] Q. H. Wang, K. Kalantar-Zadeh, A. Kis, J. N. Coleman, and M. S. Strano, "Electronics and optoelectronics of two-dimensional transition metal dichalcogenides", Nature Nanotech **7**, 699 (2012).

[115] A. Kuc, T. Heine, and A. Kis, "Electronic properties of transition-metal dichalcogenides", MRS Bulletin **40**, 577 (2015).

[116] Z. Bian, J. Miao, Y. Zhao, and Y. Chai, "Strong Interlayer Interaction for Engineering Two-Dimensional Materials", Acc. Mater. Res. **3**, 1220 (2022).

[117] D. Jariwala, V. K. Sangwan, L. J. Lauhon, T. J. Marks, and M. C. Hersam, "Emerging Device Applications for Semiconducting Two-Dimensional Transition Metal Dichalcogenides", ACS Nano **8**, 1102 (2014).

[118] H. S. Lee, S.-W. Min, Y.-G. Chang, M. K. Park, T. Nam, H. Kim, J. H. Kim, S. Ryu, and S. Im, "MoS2 Nanosheet Phototransistors with Thickness-Modulated Optical Energy Gap", Nano Lett. **12**, 3695 (2012).

[119] G. Froehlicher, E. Lorchat, and S. Berciaud, "Charge Versus Energy Transfer in Atomically Thin Graphene-Transition Metal Dichalcogenide van der Waals Heterostructures", Phys. Rev. X **8**, 011007 (2018).

[120] Q. Lv and R. Lv, "Two-dimensional heterostructures based on graphene and transition metal dichalcogenides: Synthesis, transfer and applications", Carbon **145**, 240 (2019).

[121] X. Xu, W. Yao, D. Xiao, and T. F. Heinz, "Spin and pseudospins in layered transition metal dichalcogenides", Nature Phys **10**, 343 (2014).

[122] Y. Chen, L. Wu, H. Xu, C. Cong, S. Li, S. Feng, H. Zhang, C. Zou, J. Shang, S. A. Yang, K. P. Loh, W. Huang, and T. Yu, "Visualizing the Anomalous Charge Density Wave States in Graphene/NbSe2 Heterostructures", Advanced Materials **32**, 2003746 (2020).

[123] Z. Qiu, M. Holwill, T. Olsen, P. Lyu, J. Li, H. Fang, H. Yang, M. Kashchenko, K. S. Novoselov, and J. Lu, "Visualizing atomic structure and magnetism of 2D magnetic insulators via tunneling through graphene", Nat Commun **12**, 70 (2021).

[124] Q. Zheng, Y.-C. Zhuang, Q.-F. Sun, and L. He, "Coexistence of electron whispering-gallery modes and atomic collapse states in graphene/WSe2 heterostructure quantum dots", Nat Commun **13**, 1597 (2022).

[125] Z. Y. Al Balushi, K. Wang, R. K. Ghosh, R. A. Vilá, S. M. Eichfeld, J. D. Caldwell, X. Qin, Y.-C. Lin, P. A. DeSario, G. Stone, S. Subramanian, D. F. Paul, R. M. Wallace, S. Datta, J. M. Redwing, and J. A. Robinson, "Two-dimensional gallium nitride realized via graphene encapsulation", Nature Mater **15**, 1166 (2016).

[126] J. A. Miwa, M. Dendzik, S. S. Grønborg, M. Bianchi, J. V. Lauritsen, P. Hofmann, and S. Ulstrup, "Van der Waals Epitaxy of Two-Dimensional MoS2–Graphene Heterostructures in Ultrahigh Vacuum", ACS Nano **9**, 6502 (2015).

[127] G. V. Bianco, M. Losurdo, M. M. Giangregorio, A. Sacchetti, P. Prete, N. Lovergine, P. Capezzuto, and G. Bruno, "Direct epitaxial CVD synthesis of tungsten disulfide on epitaxial and CVD graphene", RSC Adv. **5**, 98700 (2015).

[128] S. Subramanian, D. D. Deng, K. Xu, N. Simonson, K. Wang, K. Zhang, J. Li, R. Feenstra, S. K. Fullerton-Shirey, and J. A. Robinson, "Properties of synthetic epitaxial graphene/molybdenum disulfide lateral heterostructures", Carbon **125**, 551 (2017).

[129] M. T. Dau, M. Gay, D. Di Felice, C. Vergnaud, A. Marty, C. Beigné, G. Renaud, O. Renault, P. Mallet, T. Le Quang, J.-Y. Veuillen, L. Huder, V. T. Renard, C. Chapelier, G. Zamborlini, M. Jugovac, V. Feyer, Y. J. Dappe, P. Pochet, and M. Jamet, "Beyond van der Waals Interaction: The Case of MoSe2 Epitaxially Grown on Few-Layer Graphene", ACS Nano **12**, 2319 (2018).

[130] Wang, Qing-Yan, Li, Zhi, Zhang, Wen-Hao, Zhang, Zuo-Cheng, Zhang, Jin-Song, Li, Wei, Ding, Hao, Ou, Yun-Bo, Deng, Peng, Chang, Kai, Wen, Jing, Song, Can-Li, He, Ke, Jia, Jin-Feng, Ji, Shuai-Hua, Wang, Ya-Yu, Wang, Li-Li, Chen, Xi, Ma, Xu-Cun, and Xue, Qi-Kun, "Interface-Induced High-Temperature Superconductivity in Single Unit-Cell FeSe Films on SrTiO3", Chinese Phys. Lett. **29**, 037402 (2012).

[131] B. W. Yates and E. L. Hallin, "Design and performance of the double crystal monochromator beamline at the Canadian Light Source", Review of Scientific Instruments **73**, 1602 (2002).

[132] J. Sforzini, L. Nemec, T. Denig, B. Stadtmüller, T.-L. Lee, C. Kumpf, S. Soubatch, U. Starke, P. Rinke, V. Blum, F. C. Bocquet, and F. S. Tautz, "Approaching Truly Freestanding Graphene: The Structure of Hydrogen-Intercalated Graphene on 6 H - SiC (0001)", Phys. Rev. Lett. **114**, 106804 (2015).

[133] H. Yin, M. Hutter, C. Wagner, F. S. Tautz, F. C. Bocquet, and C. Kumpf, "Epitaxial growth of mono- and (twisted) multilayer graphene on SiC(0001)", Phys. Rev. Mater. **9**, 044003 (2025).

[134] Y. Cao, V. Fatemi, A. Demir, S. Fang, S. L. Tomarken, J. Y. Luo, J. D. Sanchez-Yamagishi, K. Watanabe, T. Taniguchi, E. Kaxiras, R. C. Ashoori, and P. Jarillo-Herrero, "Correlated insulator behaviour at half-filling in magic-angle graphene superlattices", Nature **556**, 80 (2018).

[135] M. Kurita, Y. Yamaji, and M. Imada, "Stabilization of topological insulator emerging from electron correlations on honeycomb lattice and its possible relevance in twisted bilayer graphene", Phys. Rev. B **94**, 125131 (2016).

[136] K. Kim, A. DaSilva, S. Huang, B. Fallahazad, S. Larentis, T. Taniguchi, K. Watanabe, B. J. LeRoy, A. H. MacDonald, and E. Tutuc, "Tunable moiré bands and strong correlations in small-twist-angle bilayer graphene", Proceedings of the National Academy of Sciences **114**, 3364 (2017).

[137] L. A. Gonzalez-Arraga, J. L. Lado, F. Guinea, and P. San-Jose, "Electrically Controllable Magnetism in Twisted Bilayer Graphene", Phys. Rev. Lett. **119**, 107201 (2017).

[138] B. Deng, B. Wang, N. Li, R. Li, Y. Wang, J. Tang, Q. Fu, Z. Tian, P. Gao, J. Xue, and H. Peng, "Interlayer Decoupling in 30° Twisted Bilayer Graphene Quasicrystal", ACS Nano **14**, 1656 (2020).

[139] W. Yao, E. Wang, C. Bao, Y. Zhang, K. Zhang, K. Bao, C. K. Chan, C. Chen, J. Avila, M. C. Asensio, J. Zhu, and S. Zhou, "Quasicrystalline 30° twisted bilayer graphene as an incommensurate superlattice with strong interlayer coupling", Proceedings of the National Academy of Sciences **115**, 6928 (2018).

[140] P. Moon, M. Koshino, and Y.-W. Son, "Quasicrystalline electronic states in 30° rotated twisted bilayer graphene", Phys. Rev. B **99**, 165430 (2019).

[141] I. Forbeaux, J.-M. Themlin, and J.-M. Debever, "Heteroepitaxial graphite on 6 H - SiC (0001) : Interface formation through conduction-band electronic structure", Phys. Rev. B **58**, 16396 (1998).

[142] R. M. Tromp and J. B. Hannon, "Thermodynamics and Kinetics of Graphene Growth on SiC(0001)", Phys. Rev. Lett. **102**, 106104 (2009).

[143] J. Schardt, J. Bernhardt, U. Starke, and K. Heinz, "Crystallography of the (3x3) surface reconstruction of 3C-SiC(111), 4H-SiC(0001), and 6H-SiC(0001) surfaces retrieved by low-energy electron diffraction", Phys. Rev. B **62**, 10335 (2000).

[144] H.-C. Shin, Y. Jang, T.-H. Kim, J.-H. Lee, D.-H. Oh, S. J. Ahn, J. H. Lee, Y. Moon, J.-H. Park, S. J. Yoo, C.-Y. Park, D. Whang, C.-W. Yang, and J. R. Ahn, "Epitaxial Growth of a Single-Crystal Hybridized Boron Nitride and Graphene Layer on a Wide-Band Gap Semiconductor", J. Am. Chem. Soc. **137**, 6897 (2015).

[145] S. Kim, J. Ihm, H. J. Choi, and Y.-W. Son, "Origin of Anomalous Electronic Structures of Epitaxial Graphene on Silicon Carbide", Phys. Rev. Lett. **100**, 176802 (2008).

[146] F. Varchon, P. Mallet, J.-Y. Veuillen, and L. Magaud, "Ripples in epitaxial graphene on the Si-terminated SiC(0001) surface", Phys. Rev. B **77**, 235412 (2008).

[147] T. Ohta, A. Bostwick, T. Seyller, K. Horn, and E. Rotenberg, "Controlling the Electronic Structure of Bilayer Graphene", Science **313**, 951 (2006).

[148] A. Bostwick, T. Ohta, T. Seyller, K. Horn, and E. Rotenberg, "Quasiparticle dynamics in graphene", Nature Phys **3**, 36 (2007).

[149] E. Rotenberg, A. Bostwick, T. Ohta, J. L. McChesney, T. Seyller, and K. Horn, "Origin of the energy bandgap in epitaxial graphene", Nature Mater **7**, 258 (2008).

[150] A. Bostwick, F. Speck, T. Seyller, K. Horn, M. Polini, R. Asgari, A. H. MacDonald, and E. Rotenberg, "Observation of Plasmarons in Quasi-Freestanding Doped Graphene", Science **328**, 999 (2010).

[151] I. Gierz, J. Henk, H. Höchst, C. R. Ast, and K. Kern, "Illuminating the dark corridor in graphene: Polarization dependence of angle-resolved photoemission spectroscopy on graphene", Phys. Rev. B **83**, 121408 (2011).

[152] H. Hibino, H. Kageshima, F. Maeda, M. Nagase, Y. Kobayashi, and H. Yamaguchi, "Microscopic thickness determination of thin graphite films formed on SiC from quantized oscillation in reflectivity of low-energy electrons", Phys. Rev. B **77**, 075413 (2008).

[153] T. Ohta, F. E. Gabaly, A. Bostwick, J. L. McChesney, K. V. Emtsev, A. K. Schmid, T. Seyller, K. Horn, and E. Rotenberg, "Morphology of graphene thin film growth on SiC(0001)", New J. Phys. **10**, 023034 (2008).

[154] P. C. Mende, J. Li, and R. M. Feenstra, "Substitutional mechanism for growth of hexagonal boron nitride on epitaxial graphene", Appl. Phys. Lett. **113**, 031605 (2018).

[155] F. Pedregosa, G. Varoquaux, A. Gramfort, V. Michel, B. Thirion, O. Grisel, M. Blondel, A. Müller, J. Nothman, G. Louppe, P. Prettenhofer, R. Weiss, V. Dubourg, J. Vanderplas, A. Passos, D. Cournapeau, M. Brucher, M. Perrot, and É. Duchesnay, "Scikit-learn: Machine Learning in Python", arXiv, 10.48550/ARXIV.1201.0490 (2012).

[156] F. C. Bocquet, R. Bisson, J.-M. Themlin, J.-M. Layet, and T. Angot, "Reversible hydrogenation of deuterium-intercalated quasi-free-standing graphene on SiC(0001)", Phys. Rev. B **85**, 201401 (2012).

[157] F. C. Bocquet, R. Bisson, J.-M. Themlin, J.-M. Layet, and T. Angot, "Deuterium adsorption on (and desorption from) SiC(0001)-(3x3), $(\sqrt{3} \times \sqrt{3})R30°$, $(6\sqrt{3} \times 6\sqrt{3})R30°$ and quasi-free standing graphene obtained by hydrogen intercalation", J. Phys. D: Appl. Phys. **47**, 094014 (2014).

[158] Gerber, Jonas, "Assembly of twisted bilayer graphene heterostructures", Project Report, RWTH Aachen, 2021.

[159] M. A. Islam, P. Serles, B. Kumral, P. G. Demingos, T. Qureshi, A. Meiyazhagan, A. B. Puthirath, M. S. B. Abdullah, S. R. Faysal, P. M. Ajayan, D. Panesar, C. V. Singh, and T. Filleter, "Exfoliation mechanisms of 2D materials and their applications", Appl. Phys. Rev. **9**, 041301 (2022).

[160] Y. Anzai, M. Yamamoto, S. Genchi, K. Watanabe, T. Taniguchi, S. Ichikawa, Y. Fujiwara, and H. Tanaka, "Broad range thickness identification of hexagonal boron nitride by colors", Appl. Phys. Express **12**, 055007 (2019).

[161] Y. Y. Wang, R. X. Gao, Z. H. Ni, H. He, S. P. Guo, H. P. Yang, C. X. Cong, and T. Yu, "Thickness identification of two-dimensional materials by optical imaging", Nanotechnology **23**, 495713 (2012).

[162] Z. Luo, S. Kim, N. Kawamoto, A. M. Rappe, and A. T. C. Johnson, "Growth Mechanism of Hexagonal-Shape Graphene Flakes with Zigzag Edges", ACS Nano **5**, 9154 (2011).

[163] J. Kim, N. Lee, Y. H. Min, S. Noh, N.-K. Kim, S. Jung, M. Joo, and Y. Yamada, "Distinguishing Zigzag and Armchair Edges on Graphene Nanoribbons by X-ray Photoelectron and Raman Spectroscopies", ACS Omega **3**, 17789 (2018).

[164] Z. Hu, Z.-B. Liu, and J.-G. Tian, "Stacking of Exfoliated Two-Dimensional Materials: A Review", Chinese Journal of Chemistry **38**, 981 (2020).

[165] W. Choi, Y.-S. Seo, J.-Y. Park, K. B. Kim, J. Jung, N. Lee, Y. Seo, and S. Hong, "Effect of Annealing in Ar/H2 Environment on Chemical Vapor Deposition-Grown Graphene Transferred With Poly (Methyl Methacrylate)", IEEE Transactions on Nanotechnology **14**, 70 (2015).

[166] D. D. L. Chung, "Review Graphite", Journal of Materials Science **37**, 1475 (2002).

[167] M. Yankowitz, J. Xue, D. Cormode, J. D. Sanchez-Yamagishi, K. Watanabe, T. Taniguchi, P. Jarillo-Herrero, P. Jacquod, and B. J. LeRoy, "Emergence of superlattice Dirac points in graphene on hexagonal boron nitride", Nature Phys **8**, 382 (2012).

[168] S. Carr, S. Fang, and E. Kaxiras, "Electronic-structure methods for twisted moiré layers", Nat Rev Mater **5**, 748 (2020).

[169] D. Wong, K. P. Nuckolls, M. Oh, R. L. Lee, K. Watanabe, T. Taniguchi, and A. Yazdani, "Insulators at fractional fillings in twisted bilayer graphene partially aligned to hexagonal boron nitride", Low Temperature Physics **49**, 655 (2023).

[170] Y. Xie, B. Lian, B. Jäck, X. Liu, C.-L. Chiu, K. Watanabe, T. Taniguchi, B. A. Bernevig, and A. Yazdani, "Spectroscopic signatures of many-body correlations in magic-angle twisted bilayer graphene", Nature **572**, 101 (2019).

[171] S.-Y. Li, K.-Q. Liu, L.-J. Yin, W.-X. Wang, W. Yan, X.-Q. Yang, J.-K. Yang, H. Liu, H. Jiang, and L. He, "Splitting of Van Hove singularities in slightly twisted bilayer graphene", Phys. Rev. B **96**, 155416 (2017).

[172] A. Inbar, J. Birkbeck, J. Xiao, T. Taniguchi, K. Watanabe, B. Yan, Y. Oreg, A. Stern, E. Berg, and S. Ilani, "The quantum twisting microscope", Nature **614**, 682 (2023).

[173] M. Long, P. A. Pantaleón, Z. Zhan, F. Guinea, J. Á. Silva-Guillén, and S. Yuan, "An atomistic approach for the structural and electronic properties of twisted bilayer graphene-boron nitride heterostructures", npj Comput Mater **8**, 1 (2022).

[174] Y. Zhu, M. Xu, and W. Zhou, "High-resolution electron microscopy for heterogeneous catalysis research", Chinese Phys. B **27**, 056804 (2018).

[175] G. A. Botton, "Probing bonding and electronic structure at atomic resolution with spectroscopic imaging", MRS Bulletin **37**, 21 (2012).

[176] O. L. Krivanek, M. F. Chisholm, V. Nicolosi, T. J. Pennycook, G. J. Corbin, N. Dellby, M. F. Murfitt, C. S. Own, Z. S. Szilagyi, M. P. Oxley, S. T. Pantelides, and S. J. Pennycook, "Atom-by-atom structural and chemical analysis by annular dark-field electron microscopy", Nature **464**, 571 (2010).

[177] P. D. Nellist, in *Science of Microscopy*, edited by P. W. Hawkes and J. C. H. Spence (Springer, New York, NY, 2007), pp. 65–132.

[178] P. D. Nellist, in *Springer Handbook of Microscopy*, edited by P. W. Hawkes and J. C. H. Spence (Springer International Publishing, Cham, 2019), pp. 49–99.

[179] S. J. Pennycook and P. D. Nellist, eds., *Scanning Transmission Electron Microscopy* (Springer, New York, NY, 2011).

[180] M. M. Treacy, "Z Dependence of Electron Scattering by Single Atoms into Annular Dark-Field Detectors", Microscopy and Microanalysis **17**, 847 (2011).

[181] Y. Xin, E. M. James, N. D. Browning, and S. J. Pennycook, "Atomic resolution Z-contrast imaging of semiconductors", J Electron Microsc (Tokyo) **49**, 231 (2000).

[182] S. Yamashita, J. Kikkawa, K. Yanagisawa, T. Nagai, K. Ishizuka, and K. Kimoto, "Atomic number dependence of Z contrast in scanning transmission electron microscopy", Sci Rep **8**, 12325 (2018).

[183] K. L. Haley, J. A. Cloninger, K. Cerminara, R. M. Sterbentz, T. Taniguchi, K. Watanabe, and J. O. Island, "Heated Assembly and Transfer of Van der Waals Heterostructures with Common Nail Polish", Nanomanufacturing **1**, 49 (2021).

[184] F. Li, H. Tang, J. Anderegg, and J. Shinar, "Fabrication and electroluminescence of double-layered organic light-emitting diodes with the Al2O3/Al cathode", Applied Physics Letters **70**, 1233 (1997).

[185] C. W. Tang, "Two-layer organic photovoltaic cell", Applied Physics Letters **48**, 183 (1986).

[186] C. W. Tang and S. A. VanSlyke, "Organic electroluminescent diodes", Applied Physics Letters **51**, 913 (1987).

[187] C. Dimitrakopoulos and P. Malenfant, "Organic Thin Film Transistors for Large Area Electronics", Advanced Materials **14**, 99 (2002).

[188] T. Hasegawa and J. Takeya, "Organic field-effect transistors using single crystals", Science and Technology of Advanced Materials **10**, 024314 (2009).

[189] H. Klauk, "Organic thin-film transistors", Chem. Soc. Rev. **39**, 2643 (2010).

[190] R. Giridharagopal and D. S. Ginger, "Characterizing Morphology in Bulk Heterojunction Organic Photovoltaic Systems", J. Phys. Chem. Lett. **1**, 1160 (2010).

[191] H. Hoppe and N. S. Sariciftci, "Organic solar cells: An overview", J. Mater. Res. **19**, 1924 (2004).

[192] R. Steim, F. R. Kogler, and C. J. Brabec, "Interface materials for organic solar cells", J. Mater. Chem. **20**, 2499 (2010).

[193] A. Haags, A. Reichmann, Q. Fan, L. Egger, H. Kirschner, T. Naumann, S. Werner, T. Vollgraff, J. Sundermeyer, L. Eschmann, X. Yang, D. Brandstetter, F. C. Bocquet, G. Koller, A. Gottwald, M. Richter, M. G. Ramsey, M. Rohlfing, P. Puschnig, J. M. Gottfried, S. Soubatch, and F. S. Tautz, "Kekulene: On-Surface Synthesis, Orbital Structure, and Aromatic Stabilization", ACS Nano **14**, 15766 (2020).

[194] S. R. Kachel, B. P. Klein, J. M. Morbec, M. Schöniger, M. Hutter, M. Schmid, P. Kratzer, B. Meyer, R. Tonner, and J. M. Gottfried, "Chemisorption and Physisorption at the Metal/Organic Interface: Bond Energies of Naphthalene and Azulene on Coinage Metal Surfaces", J. Phys. Chem. C **124**, 8257 (2020).

[195] J. Herritsch, S. R. Kachel, Q. Fan, M. Hutter, L. J. Heuplick, F. Münster, and J. M. Gottfried, "On-surface porphyrin transmetalation with Pb/Cu redox exchange", Nanoscale **13**, 13241 (2021).

[196] N. Armbrust, F. Schiller, J. Güdde, and U. Höfer, "Model potential for the description of metal/organic interface states", Sci Rep **7**, 46561 (2017).

[197] M. Marks, N. L. Zaitsev, B. Schmidt, C. H. Schwalb, A. Schöll, I. A. Nechaev, P. M. Echenique, E. V. Chulkov, and U. Höfer, "Energy shift and wave function overlap of metal-organic interface states", Phys. Rev. B **84**, 081301 (2011).

[198] B. Stadtmüller, D. Lüftner, M. Willenbockel, E. M. Reinisch, T. Sueyoshi, G. Koller, S. Soubatch, M. G. Ramsey, P. Puschnig, F. S. Tautz, and C. Kumpf, "Unexpected interplay of bonding height and energy level alignment at heteromolecular hybrid interfaces", Nat Commun **5**, 3685 (2014).

[199] B. Stadtmüller, C. Henneke, S. Soubatch, F. S. Tautz, and C. Kumpf, "Tailoring metal–organic hybrid interfaces: heteromolecular structures with varying stoichiometry on Ag(111)", New J. Phys. **17**, 023046 (2015).

[200] T. Huempfner, F. Sojka, R. Forker, and T. Fritz, "Growth of coronene on (100)- and (111)-surfaces of fcc-crystals", Surface Science **639**, 80 (2015).

[201] L. Zhang, D. Shi, S. Du, L. Chi, H. Fuchs, and H.-J. Gao, "Structural Transition and Thermal Stability of a Coronene Molecular Monolayer on Cu(110)", J. Phys. Chem. C **114**, 11180 (2010).

[202] S. Weiß, D. Gerbert, A. Stein, A. K. Schenk, X. Yang, C. Brülke, R. Kremring, S. Feldmann, F. C. Bocquet, M. Gille, S. Hecht, M. Sokolowski, P. Tegeder, S. Soubatch, and F. S. Tautz, "Dependence of the adsorption height of graphenelike adsorbates on their dimensionality", Phys. Rev. B **98**, 075410 (2018).

[203] K. A. Simonov, N. A. Vinogradov, A. S. Vinogradov, A. V. Generalov, E. M. Zagrebina, G. I. Svirskiy, A. A. Cafolla, T. Carpy, J. P. Cunniffe, T. Taketsugu, A. Lyalin, N. Mårtensson, and A. B. Preobrajenski, "From Graphene Nanoribbons on Cu(111) to Nanographene on Cu(110): Critical Role of Substrate Structure in the Bottom-Up Fabrication Strategy", ACS Nano **9**, 8997 (2015).

[204] C. Bronner, J. Björk, and P. Tegeder, "Tracking and Removing Br during the On-Surface Synthesis of a Graphene Nanoribbon", J. Phys. Chem. C **119**, 486 (2015).

[205] B. Moeini, M. R. Linford, N. Fairley, A. Barlow, P. Cumpson, D. Morgan, V. Fernandez, and J. Baltrusaitis, "Definition of a new Doniach-Sunjic-Shirley peak shape for fitting asymmetric signals applied to reduced graphene oxide/graphene oxide XPS spectra", Surface and Interface Analysis **54**, 67 (2022).

[206] X. Yang, L. Egger, P. Hurdax, H. Kaser, D. Lüftner, F. C. Bocquet, G. Koller, A. Gottwald, P. Tegeder, M. Richter, M. G. Ramsey, P. Puschnig, S. Soubatch, and F. S. Tautz, "Identifying surface reaction intermediates with photoemission tomography", Nat Commun **10**, 3189 (2019).

9 List of Publications

- M. Schöniger, S. R. Kachel, J. Herritsch, P. Schröder, **M. Hutter**, and J. M. Gottfried, "Direct synthesis of dilithium tetraphenylporphyrin: facile reaction of a free-base porphyrin with vapor-deposited lithium", Chemical Communications **55**, 91, 13665-13668 (2019).
- S. R. Kachel, B. Klein, J. Morbec, M. Schöniger, **M. Hutter**, M. Schmid, P. Kratzer, B. Meyer, R. Tonner and J. M. Gottfried, "Chemisorption and Physisorption at the Metal/Organic Interface: Bond Energies of Naphthalene and Azulene on Coinage Metal Surfaces", The Journal of Physical Chemistry C **124**, 15, 8257-8268 (2020).
- J. Herritsch, S. R. Kachel, Q. Fan, **M. Hutter**, L. Heuplick, F. Münster and J. M. Gottfried, "On-surface porphyrin transmetalation with Pb/Cu redox exchange", Nanoscale **13**, 13241-13248 (2021).
- Y.-R. Lin, S. Wolff, P. Schädlich, **M. Hutter**, S. Soubatch, T.-L. Lee, F. S. Tautz, T. Seyller, C. Kumpf, and F. C. Bocquet, "Vertical structure of Sb-intercalated quasifreestanding graphene on SiC(0001)", Physical Review B **106**, 15, 155418 (2022).
- P. Schädlich, C. Ghosal, M. Stettner, B. Matta, S. Wolff, F. Schölzel, P. Richter, **M. Hutter**, A. Haags, S. Wenzel, Z. Mamiyev, J. Koch, S. Soubatch, P. Rosenzweig, C. Polley, F. S. Tautz, C. Kumpf, K. Küster, U. Starke, T. Seyller, F. C. Bocquet, and C. Tegenkamp, "Domain Boundary Formation Within an Intercalated Pb Monolayer Featuring Charge-Neutral Epitaxial Graphene", Advanced Materials Interfaces **10**, 27, 2300471 (2023).
- S. Wolff, **M. Hutter**, P. Schädlich, H. Yin, M. Stettner, S. Wenzel, F. S. Tautz, F. C. Bocquet, T. Seyller, and C. Kumpf, "Bi-intercalated epitaxial graphene on SiC(0001)", New Journal of Physics **26**, 10, 103009 (2024).

- H. Yin, **M. Hutter**, C. Wagner, F. S. Tautz, F. C. Bocquet, and C. Kumpf, ”Epitaxial growth of mono- and (twisted) multilayer graphene on SiC(0001)”, Physical Review Materials **9**, 4, 044003 (2025).
- J. Herritsch, C. Gong, L. Heuplick, **M. Hutter**, Q. Fan, F. Münster, S. R. Kachel, M. Zugermeier, and J. M. Gottfried, ”On-surface chemistry of Pb(II) tetraphenylporphyrin on Au(111): reversible metalation, thermal degradation, and formation of a covalent organic framework”, Physical Chemistry Chemical Physics **27**, 20, 10875-10883 (2025).

10 Appendix

10.1 Coronene and DBBA as 0D- and 1D-Graphene

The interest of the scientific community in interfaces has been huge in the last years. The fundamental works help to understand the properties of interfaces and therefore optimize technical applications, especially those based on the interface between metals and organic molecules, like organic light emitting diodes [184–186], organic field-effect transistors [187–189] and organic solar cells [190–192]. Despite the various works on organic-metal interface, as for example on on-surface syntheses [193], on adsorption strengths [194] or on metalation reactions [195], the potential temperature dependence of the adsorption height is lacking comprehensive studies. The adsorption height - distance between metal surface and the molecule - plays a crucial role for various properties like the interaction strength, charge transfer as well as the energies and lifetimes of interface states [196–199]. Especially for the interface states, Armbrust et al. have predicted a temperature dependence of the energies and lifetimes for a carbon layer on Ag(111) and compared the resulting distances to experimental data [196]. However, a more systematic, experimental study on the temperature dependence of the adsorption height is needed to further understand the surface interaction.

In this work, the investigations of the temperature dependence of the adsorption heights for two model systems have begun prior to the covid-19 pandemic. The model systems were chosen to reflect so-called ”0D” (zero-dimensional) - and ”1D”-graphene. For ”0D” graphene, the molecule coronene was chosen, because coronene consists only out of carbon six-rings, as depicted in Fig. 10.1 (left), which limits its extension in all directions. Moreover, its growth and structure is studied on various metal surfaces [200, 201]. In contrast, di-bromo-di-antracene (DBBA, compare Fig. 10.1 (right)) performs an on-surface reaction at elevated temperatures and can form 1D graphene nanoribbons

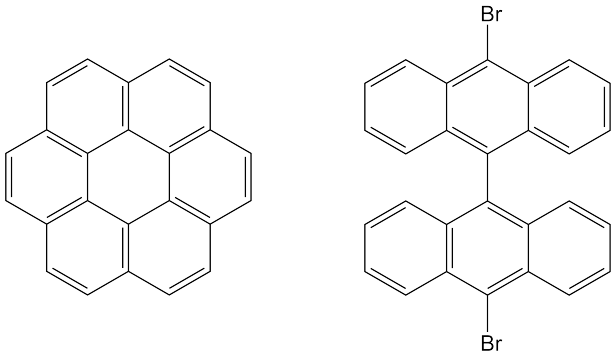

Fig. 10.1: Structure formula of coronene on the left and DBBA on the right.

[202–204]. For even higher annealing temperatures also 2D graphene can be formed. Therefore, these two molecules were chosen as model systems.

First, the preparation of coronene on Cu(111) is prepared and investigated with XPS in order to check for the amount of coronene on top and its behavior upon annealing. Second, the same is performed for DBBA on Cu(111). It is noteworthy, that the here shown data, is very preliminary work since the project was first paused and the cancelled due to the limitations of the covid-19 pandemic. Hence, no beamtime experiments could be scheduled within a reasonable timeframe. The beamtime at Diamond Light Source is necessary to measure the adsorption heights of the model systems at various temperatures and hence extract the temperature dependence of these adsorption heights.

The coronene on Cu(111) sample was prepared in the following way. The Cu(111) crystal was cleaned by alternating cycles of sputtering with Ar ions and annealing to 450°C. The cleanliness of the Cu(111) surface was checked by means of XPS (survey, C 1s, Br 3p, Cu 2p, O 1s). Then the coronene molecules were evaporated, using a commercial Knudsen cell evaporator, at 208°C for 30 min.

For characterization of the coronene layer on Cu(111) XPS investigations have been performed. In Fig. 10.2, a heating series of a coronene layer is shown. This means, that the sample was first investigated by XPS, then annealed to 100°C and investigated again by

XPS. This was performed for several heating steps (100°C to 240°C in steps of 20°C). The most interesting core-level for coronene is obviously the C 1s. Here, the temperature dependence of the coverage can be investigated. Additionally, one gains insight whether the chemical surrounding of the coronene is changed upon annealing to increasing temperatures. The raw XP spectra of the several heating steps is shown in Fig. 10.2 (a), showing one intense peak at a rough binding energy of 284.5 eV. To get more insight into the change of intensity of the peak, this peak has been fitted using a shirley background and a convolution of a gaussian and a Doniach-Sunjic profile for the peak. Here, the gaussian is representing the broadening of the signal due to the experimental setup, while the Doniach-Sunjic profile is taking care of the samples properties. This model is used for asymmetric peaks [205]. This fit model is shown in Fig. 10.2 (c) exemplary for the XPS signal of the sample annealed to 160°C. This fit model has been applied to all the C 1s spectra measured for the different annealing temperatures. The resulting fits as well as the raw data are shown in panel (d). Here, the same colors have been used as in (a), but the spectra have been vertically offset for clarity. From these fits, the integral of the peak can be extracted for all annealing temperatures. The temperature-dependence of the peak integral is plotted in Fig. 10.2 (d). It can be observed, that annealing above 100°C leads to a reduction of the carbon signal. The most likely explanation is that the coronene molecules start to desorb from the Cu(111) surface at these temperatures, which continously happening until the endpoint of this investigation at 240°C, where roughly half of the coronene molecules is still present.

For DBBA, the sample preparation was similar to the one described for coronene. The only difference is that the DBBA molecules were evaporated at 260°C for 10 min. As it was done for coronene, also for DBBA a heating series was performed. The used annealing steps were 100°C, 200°C, 250°C, 300°C, 350°C, 400°C, 500°C and 600°C. First, the C 1s XP spectra are shown in a similar way, as it was done for coronene, in Fig. 10.3. When regarding the peaks, the corresponding fits as well as the temperature-dependence of the peak integrals, the resulting data has a less clear trend. This might be on the one hand due to the occuring on-surface reaction, and therefore changing bonding situations, and on the other hand, more likely, due to the preliminary state of the investigations. Especially, the change in peak integral towards higher amounts of carbon on the Cu(111) surface when annealing from 400°C to 500°C is physically not reasonable,

because the reduced amounts of the former annealing steps is usually attributed to the desorption of molecules [202, 203, 206].

Additionally to C 1s XP spectra, the Br 3p XP spectra have been recorded for a few of the annealing steps, as shown in Fig. 10.4. They give insight on the state of the on-surface reaction, because upon connecting of two DBBA molecules towards the graphene nanoribbon, the Br atoms are removed from the molecules and desorb afterwards. The Br 3p XP spectra have been measured for 50°C, 100°C, 250°C, 350°C and 600°C. As it can be seen in Fig. 10.4 (a) the spectra have a bad signal-noise ratio due to the limited measurement time. The data were fitted using again the convolution of Gaussian and Doniach-Sunjic profiles, but for the background a constant background subtraction was chosen. While the constant background probably does not reflect the physical background, the recorded data do not allow a more detailed description of the background because it has a bad signal-to-noise ratio and more importantly the investigated binding energy range is not far enough. Therefore, the supposed background has still a contribution from the bromine peak. Therefore, one needs to address the peak integrals shown in Fig. 10.4 (d) with care. One thing, which can be extracted, is that the Br content on the surface drops to almost zero at an annealing temperature of 600°C. A slight decrease of Br atoms could be observed at 350°C although one needs to be careful due to the high uncertainties mentioned before.

In summary, preliminary XPS investigations have been performed on both coronene (as 0D) and DBBA (as 1D). For coronene, a clear trend upon annealing the sample is observed. The molecules start desorbing at temperatures above 100°C. For DBBA, the situation is more complex. While also a small loss of carbon is observed, the data is fluctuating way more and therefore prevent an extraction of clear trends and explanations. The most clear point is the loss of all Br atoms after annealing to 600°C. For more detailed information and for a potential resumption of the project, better XP spectra (longer measuring times) as well as smaller annealing steps would help to gain further insight on the needed preparation for investigations of the temperature-dependence of the adsorption height at the Diamond Light Source using NIXSW.

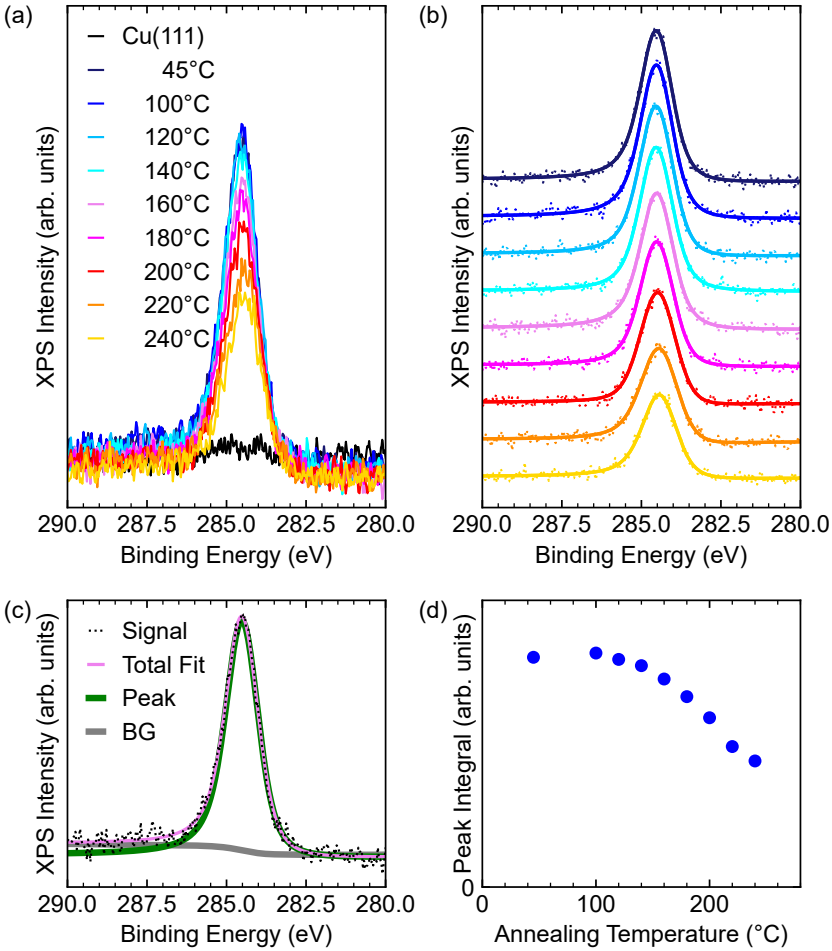

Fig. 10.2: C 1s heating series of coronene on Cu(111) with XPS. (a) C 1s XP spectra for annealing temperatures from 45°C to 240°C, (b) same spectra as in (a), but with a Shirley background substracted (as dots) and the peak fitted to it (as a line) offsetted in y-axis for clarity. The colors are the same as in (a). (c) Exemplary fit of one spectrum (160°C) showing the shirley background as well as the asymmetric gaussian-lorentzian peak, (d) plot of the integral of the peak versus the annealing temperature.

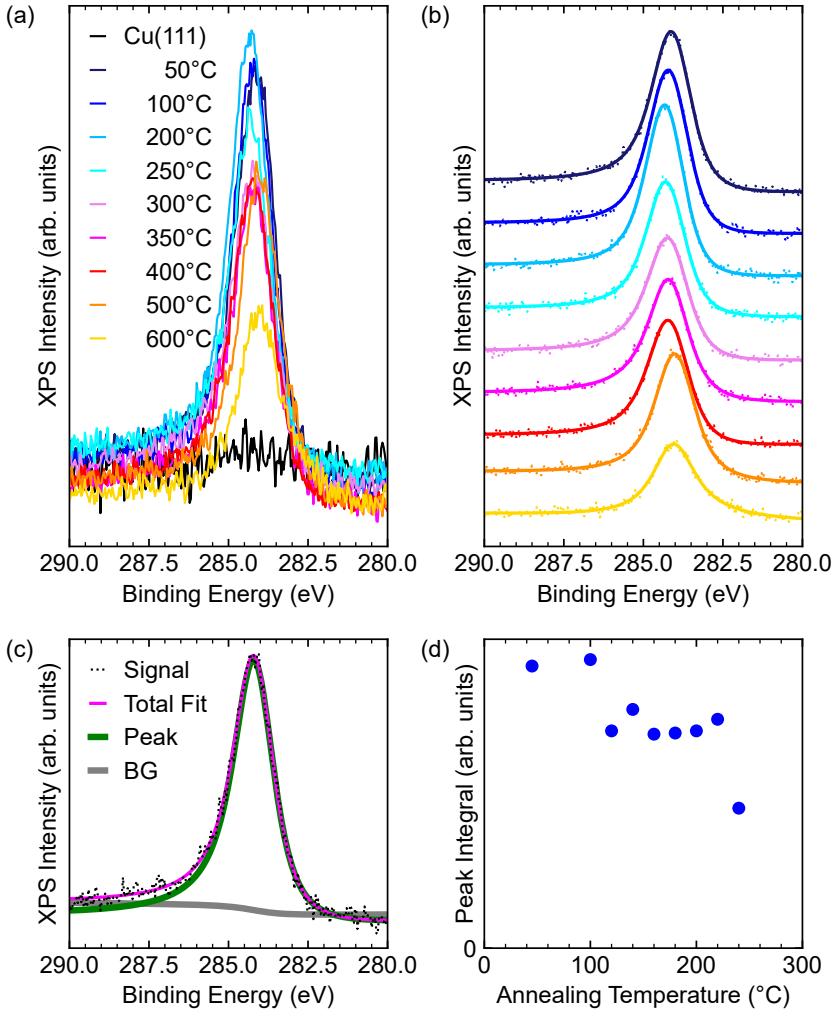

Fig. 10.3: C 1s heating series of DBBA on Cu(111) with XPS. (a) C 1s XP spectra for annealing temperatures from 50°C to 600°C, (d) same spectra as in (a), but with a Shirley background substracted (as dots) and the peak fitted to it (as a line) offsetted in y-axis for clarity. The colors are the same as in (a). (c) exemplary fit of one spectrum (160°C) showing the shirley background as well as the asymmetric gaussian-lorentzian peak. (d) Plot of the integral of the peak versus the annealing temperature.

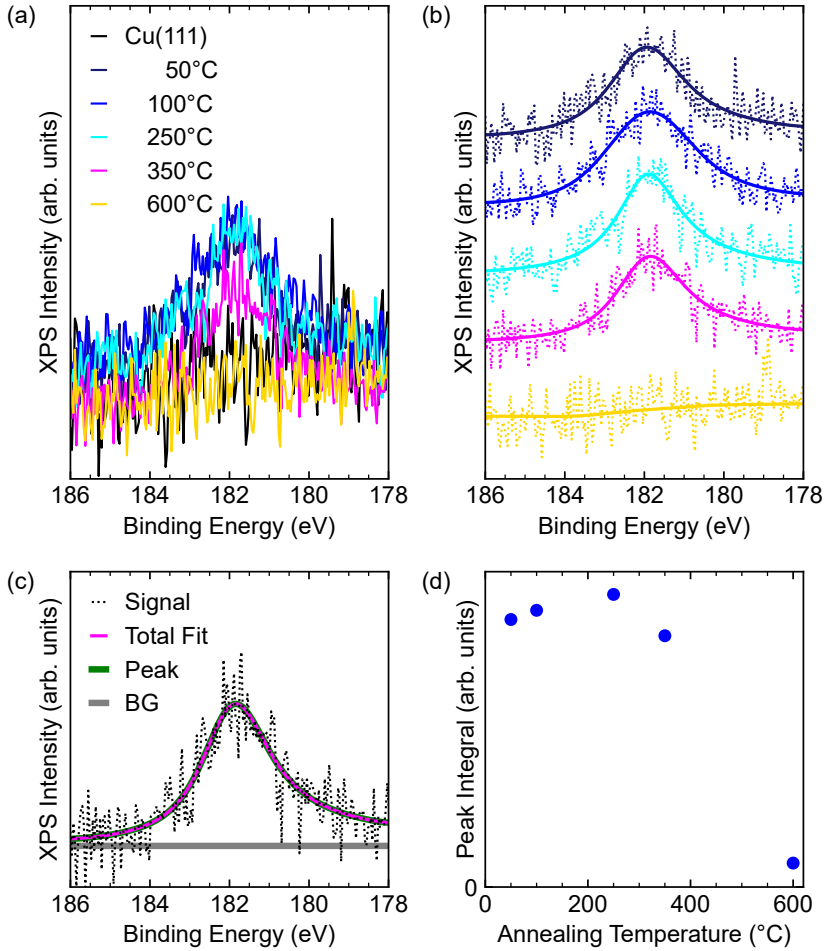

Fig. 10.4: Br 3p 3/2 heating series of DBBA on Cu(111) with XPS. (a) Br 3p 3/2 XP spectra for annealing temperatures from 50°C to 600°C, (b) same spectra as in (a), but with a constant background substracted (as dots) and the peak fitted to it (as a line) offsetted in y-axis for clarity. The colors are the same as in (a). (c) Exemplary fit of one spectrum (160°C) showing a constant background as well as the asymmetric gaussian-lorentzian peak. (d) Plot of the integral of the peak versus the annealing temperature.

Acknowledgments

During my Ph.D. I had the opportunity to work, discuss and share knowledge with many people. I would like to thank them all!

First of all, I would like to thank Prof. Dr. Stefan Tautz for giving me the opportunity to do my Ph.D. at his institute (PGI-3) and for being my supervisor. I would also like to thank him for his guidance and support during this time.

I would like to thank Prof. Dr. Michael Gottfried for the exceptional education during my bachelor and master studies and for co-advising my doctoral thesis.

I want to thank Prof. Dr. Christian Kumpf very much for his support. Not only did he help me with the scientific problems, but he also helped me with other issues.

I want to thank Dr. François Bocquet for his continuous scientific, moral and lab support in every problem I faced. Without him this thesis would not have been possible.

I want to thank Dr. Felix Lüpke for supervising my work on the TBLG sample for STM and its preparation in the 2D lab. He was always eager to help me achieve the desired results.

I want to thank Dr. You-Ron Lin, Miriam Raths for introducing me to the institute, the necessary laboratories and especially the social environment here at PGI-3.

I cannot express enough thanks to Dr. Sabine Wenzel for the time we worked together to achieve these beautiful STM results. She was a great help not only in learning how to measure STM, but also in keeping my head up mentally during difficult times of my journey.

I would like to thank Dr. José Martinez, Tobias Wichmann and Keda Jin for their help in everything related to 2D heterostructures and for being nice colleagues.

I want to thank Monja Stettner for being always willing to help me with various problems and for being so forgiving of all the mistakes I probably made while supervising your master's thesis.

I want to thank Hao Yin for your positive energy and help in the lab. In addition, it was very pleasant to work on the paper with you.

I would like to thank Susanne Wolff, Dr. Philipp Schädlich and Prof. Dr. Thomas Seyller for the very fruitful collaboration, which resulted in successful beamtimes and nice publications.

I would like to thank Dr. Oliver Maßmeyer, Dr. Andreas Beyer and Prof. Dr. Kerstin Volz for your cooperation in the TEM investigations of TBLG.

I would like to thank Dr. Anja Haags for everything! Although we had hardly any professional overlap, she was the most important person during my PhD time! She always helped me, no matter how stressful her own work and life was. Without her, I probably would not be where I am now. Thank you to Anja for being such a nice friend.

Dr. Jose Guevara-Parra, thank you for your assistance with analyzing STM data and the weekly distractions during bouldering.

Dr. Taner Esat, thank you for the nice time during lunch or coffee breaks and for your help in understanding STM results.

Thank you to the entire PGI-3 institute for the nice working environment! Everyone, I worked with was always very helpful, friendly and supportive!

I would like to thank Silke Behlau, Claudia Funk, Helmut Stollwerk and Denis Krylov for your help in all organizational and technical aspects of my thesis.

Last but not least, I would like to thank my family and friends for their constant support and sometimes distraction during my journey towards a Ph.D. degree.

Band / Volume 114
A System for the Cryogenic Power Management of Quantum Computing Electronics: Development, Integration, and Test
A. R. Cabrera Galicia (2025), xxv, 110, lviii pp
ISBN: 978-3-95806-844-5

Band / Volume 115
Investigation of 2D Materials using Low Energy Electron Microscopy (LEEM)
H. Yin (2025) viii, 137 pp
ISBN: 978-3-95806-848-3

Band / Volume 116
Topotactic phase transition in $La_{0.6}Sr_{0.4}CoO_{3-\delta}$ thin films: oxygen content, dynamics and reversibility
S. He (2025) ix, 137 pp
ISBN: 978-3-95806-868-1

Band / Volume 117
Electrical anisotropy and shear-resistant topology in the quasi one-dimensional van-der-Waals material α-Bi_4Br_4
J.K. Hofmann (2025) xv, 129 pp
ISBN: 978-3-95806-869-8

Band / Volume 118
Spin-orbital mixing in the topological ladder of the two-dimensional metal $PtTe_2$
M. Qahosh (2025), ix, 170 pp
ISBN: 978-3-95806-872-8

Band / Volume 119
Functions of SNNs constrained by biology
A. Korcsak-Gorzo (2025), xvi, 145 pp
ISBN: 978-3-95806-876-6

Band / Volume 120
On Scalable Integrated Charge State Tuning for Semiconductor Quantum Dot Devices
F. A. Hader (2026), xx, 145 pp
ISBN: 978-3-95806-884-1

Band / Volume 121
Efficient Massively Space-Time-Parallel Simulations with Adaptive Spectral Deferred Correction
T. Saupe (2026), v, 149 pp
ISBN: 978-3-95806-886-5

Band / Volume 122
Controlled single-molecule manipulation
P. Kopp (2026), viii, 136 pp
ISBN: 978-3-95806-887-2

Band / Volume 123
Growth and Excitation Dynamics of Epitaxial 2D Materials and Molecular Layers Studied by Electron and Momentum Microscopy
M. E. Raths (2026), xvi, 161, XXIX pp
ISBN: 978-3-95806-892-6

Band / Volume 124
Ferroelectric and Resistive Switching in Epitaxial $Hf_{0.5}Zr_{0.5}O_2$
J. R. Knabe (2026), 145 pp
ISBN: 978-3-95806-895-7

Band / Volume 125
Temperature Influences on Frequency Mixing Magnetic Detection for mobile Drinking Water Analysis in Crisis Areas
M. Jessing (2026), xx, 113 pp
ISBN: 978-3-95806-902-2

Band / Volume 126
Light-matter interaction from ab-initio Keldysh formalism
M. D. Merte (2026), xvi, 184, A-27 pp
ISBN: 978-3-95806-906-0

Band / Volume 127
Towards high-quality decoupled Graphene heterostructures
M. Hutter (2026), VIII, 149 pp
ISBN: 978-3-95806-912-1 (Print)
ISBN: 978-3-95806-913-8 (E-Book)

Information
Band / Volume 127
ISBN 978-3-95806-913-8

Mitglied der Helmholtz-Gemeinschaft

JÜLICH
Forschungszentrum